1-1-2014

Kinetic Studies of Model Reactions to Transform Biomass into Fuels

Dhairya Dilip Mehta
Purdue University

Graduate School ETD Form 9
(Revised 01/14)

PURDUE UNIVERSITY
GRADUATE SCHOOL
Thesis/Dissertation Acceptance

This is to certify that the thesis/dissertation prepared

By Dhairya Dilip Mehta

Entitled
Kinetic Studies of Model Reactions to Transform Biomass into Fuels

For the degree of Doctor of Philosophy

Is approved by the final examining committee:

Fabio H. Ribeiro

Rakesh Agrawal

W. Nicholas Delgass

Mahdi Abu-Omar

To the best of my knowledge and as understood by the student in the Thesis/Dissertation Agreement, Publication Delay, and Certification/Disclaimer (Graduate School Form 32), this thesis/dissertation adheres to the provisions of Purdue University's "Policy on Integrity in Research" and the use of copyrighted material.

Fabio H. Ribeiro

Approved by Major Professor(s): _____

_____

Approved by: John A. Morgan 08/18/2014

Head of the Department Graduate Program Date

KINETIC STUDIES OF MODEL REACTIONS TO TRANSFORM BIOMASS INTO FUELS

A Dissertation

Submitted to the Faculty

of

Purdue University

by

Dhairya D. Mehta

In Partial Fulfillment of the

Requirements for the Degree

of

Doctor of Philosophy

December 2014

Purdue University

West Lafayette, Indiana

aut viam inveniam aut faciam

उपायं करिष्यामि उत उपायं कार्षम्।

ACKNOWLEDGEMENTS

The submission of my thesis marks the culmination of five years of an amazing journey as a graduate student which has been possible due to support from a large of number of people.

To whom I owe everything, my parents Dilip and Prafulla Mehta, I would like to say a heartfelt thank you for their unending sacrifice and support. During this journey, I have had the good fortune of being advised by Prof. Fabio H. Ribeiro, Prof. Rakesh Agrawal and Prof. W. Nicholas Delgass. I have been able to count on them not only for sound advice but also to provide me with essential tools and means to achieve the best results. Prof. Ribeiro has taught me experimental meticulousness and is largely responsible for the R^2=0.99 data that is presented in the thesis. His expertise in the area of catalysis has been instrumental in ensuring that the project always stayed on track. Every meeting with Prof. Agrawal was always eventful especially with an abundance of ideas which have always left me enthusiastic to go back in the lab. He has continually encouraged to keep in mind the big picture and to be inquisitive in every area of research. The passion Prof. Delgass has for mentoring and teaching students is inspirational and I aspire to emulate that one day. His emphasis on critical analysis of data and literature has been one of the major learnings of my graduate study.

I would like also thank Prof. Mahdi Abu-Omar for serving in my committee and for providing valuable suggestions. Dr. Maureen McCann, Carl Huetteman and the entire C3Bio team should also be acknowledged for providing a wonderful opportunity to work in an environment leading to collaborative success. Financial support for the projects presented in this thesis was provided by C3Bio, an energy frontier research center funded by U.S. Department of Energy, Office of Science, Office of Basic Energy Sciences, Award Number DE-SC0000997.

I would like to express my appreciation toward mentors who initiated me into the research lab - Dr. Saurabh Chaugule, Dr. W. Damion Williams, Dr. Mayank Shekhar, Dr. Bradley Fingland, Dr. Jorge Pazmiño and Dr. Vincent Kispersky have all helped in more than one way. A special thank you goes out to Dr. Sara Yohe who has been a great buddy and a source of advice as the ‘co-catalysis experimentalist’ in the biomass to fuels group.

Past biomass group members, Dr. Navneet Singh, Dr. Andrew Smeltz, Dr. Fernando Resende, Dr. Jun Wang, Dr. Dharik Mallapragada and Dr. Piotr Gawecki have always helped with their insights and learnings. Harshavardhan Choudhari, John Degenstein, Vinod Kumar Venkatakrishnan, and Mckay Easton, have been great colleagues and it was wonderful to be a part of this team and my best wishes are with them for the future. A number of current catalysis group members, Anuj, Amir, Arthur, Atish, Fred, Han-Ting, Ian, Jamie, Jonatan, Juan, Kaiwalya, Mike, Shankali, Viktor, Yanran and Zhenglong have been contributories to many a discussion and I wish them well on their exciting journey as catalysis researchers.

I would like to specially mention among my first-year classmates – Cameron Hill, Andy Koswara, Dr. Paul Dietrich, Danni Gao and Dr. Bryce Walker for their continuing friendship. I would like to thank my office-mates at various times, Leonardo, Nathália, Emre, Josh, Gautham, Easa and Dharik whose company I have enjoyed during breaks between lab work. During my time as a social committee chair in the graduate student organization, my fellow members Kevin, Danni and Atish were a great team and made planning for social events fun.

Friends and apartment-mates (past and current), Harshavardhan Choudhari, Dr. Karthikeyan Marimuthu, Dr. Krishnaraj Sambath, Sumeet Thete and Ashish Vora – have been instrumental in making me feel at home away from home. I am indebted to them for their constant support and motivation. I am grateful of catalysis group members, Kaiwalya Sabnis and Atish Parekh with whom I have shared my 'extra-curricular catalysis' discussions, which has many a times led to new ideas for my experiments. Cherished memories with Vishesh, Anirudh, Anand, Neelanjan, Mahaprasad, Anshu, Aniruddha and Shankali will always be reminisced. Good times with Erika, Ryan and Kristen will be fondly remembered. I will always be grateful to Sachin for being a great mentor and someone I continually look up to.

A number of staff at school of chemical engineering have helped at various times. Dr. Yury Zvinevich deserves a special recognition for always being at hand to help with equipment troubleshooting. Deb Bowman was always prompt and efficient in solving our problems even before I landed in the United States. I would also like to thank Cristina Farmus, Dr. Catherine Field, Amy Hayden, Courtney Eddy, Jenny Olinger, Larry Campbell, Jason Davenport and Jeff Valley for their assistance over the years.

Finally, folks at MSEE coffee shop, especially April LaGrainge for always serving coffee with a smile, which is largely responsible for productivity in the latter half of most days.

Thank you all!

TABLE OF CONTENTS

Page

Page

Page

Page

Page

LIST OF TABLES

Table Page

Appendix Table

LIST OF FIGURES

Figure Page

Figure Page

Figure Page

Figure Page

Appendix Figure

Figure Page

LIST OF ABBREVIATIONS

C	Norit carbon
DAMP	Dianhydromannopyranose
DDO	Direct deoxygenation
DFT	Density functional theory
DHE	Dihydroeugenol
EXAFS	Extended X-ray absorption fine structure
FID	Flame ionization detector
FTIR	Fourier transformed infrared
GC	Gas chromatograph
GC-MS	Gas chromatograph – Mass spectrometer
HDO	Hydrodeoyxgenation
HYD	Hydrogenation
IWI	Incipient wetness impregnation
LC-MS	Liquid chromatograph – Mass spectrometer
LQIT-MS	Linear quadropole ion trap mass spectrometer
LWGS	Liquid-phase water gas shift
Mo	Molybdenum
MWCNT	Multi walled carbon nanotubes
Pt	Platinum
RID	Refractive index detector
S_c	Product carbon selectivity

S_{ring}	Product ring selectivity
STEM	Scanning transmission electron microscopy
STY	Site-time yield
STY_m	Site-time yield normalized by total metal content
STY_{Pt}	Site-time yield normalized by platinum content
TCD	Thermal conductivity detector
TEM	Transmission electron microscopy
TOC	Total organic carbon
TOF	Turnover frequency
TPR	Temperature programmed reduction
UHP	Ultra-high purity
WGS	Water-gas shift
WHSV	Weight hourly space velocity
XANES	X-ray absorption near edge spectroscopy
XAS	X-ray absorption spectroscopy
XPS	X-ray photoelectron spectroscopy

ABSTRACT

Mehta, Dhairya D. Ph.D., Purdue University, December 2014. Dissertation Kinetic studies of model reactions to transform biomass into fuels. Major Professors: Fabio H. Ribeiro, Rakesh Agrawal, and W. Nicholas Delgass.

Second-generation biofuels utilizing lignocellulosic biomass are considered to be a promising alternative to fossil-based fuels. Lignocellulosic biomass is structurally diverse and therefore requires detailed understanding of the thermal depolymerization and catalytic hydrodeoxygenation reactions to optimize the overall process. This dissertation describes the experimental work using model compounds to elucidate the role of bimetallic catalyst and control the reaction operating parameters such as temperature and hydrogen pressure to maximize energy recovery in the liquid product from biomass resource.

Water-gas shift (WGS) is a well-known reaction to produce hydrogen and finds application industrially in steam-reforming of methane and other fossil-based feedstocks. Traditionally, gas-phase WGS has been studied on noble metal based catalysts in experimental conditions relevant to reforming of methane. Recently, aqueous-phase reforming of oxygenated organic compounds has been considered to be one of the promising routes to produce hydrogen from sustainable biomass derivatives. One of the

hypothesis in that study was that WGS played a vital role in production of hydrogen and thus it is important to quantify and qualify the contribution of WGS under aqueous reforming conditions. Platinum (Pt) and platinum-molybdenum (Pt-Mo) catalysts supported on multi-walled carbon nanotubes (MWCNT) were chosen since they were studied previously for aqueous-phase reforming of glycerol. Under these conditions, kinetics of WGS were significantly altered, especially CO order which is ~0.9 compared to ~0.1 for gas-phase WGS. Furthermore, Mo is shown to alter the kinetics of WGS reaction in a similar way both in gas and liquid-phase WGS.

Fast-hydropyrolysis followed by in-line catalytic hydrodeoxygenation has been shown to have the potential to produce hydrocarbon fuels using hydrogen as co-feed. The objective of the research project was to identify and quantify the primary products of fast hydropyrolysis as well as establish the effect of temperature on overall product distribution. A torch igniter typically used in rocket engines was modified to design a reactor that is able to continuously feed biomass at a g min^{-1} scale and complete the entire process from fast hydropyrolysis to condensation of bio-oil in a matter of <70 ms at 3.6 MPa hydrogen pressure. Levoglucosan, cellobiosan, glycolaldehyde and glucopyranosyl-β-aldehyde were the major products from cellulose pyrolysis at 500°C. As hydropyrolysis temperature was increased in the range of 500 to 700°C, the bio-oil product distribution shifted toward C_2-C_5 light oxygenates. The identification and quantification of products with molecular weight higher than the monomer (levoglucosan) at 70 ms residence time compared to their absence in reactors with residence time of 2-3 s indicate that

levoglucosan is not the sole primary product of cellulose pyrolysis. Thus a portion of levoglucosan is a result of dimer (cellobiosan) and trimer (cellotriosan) degradation.

Hydropyrolysis of cellulose resulted in a product distribution that retained most of the oxygen from parent cellulose. Catalytic hydrodeoxygenation (HDO) therefore assumes the vital part of selectively removing that oxygen as water and thus transforming the oxygenated organic compounds to fungible hydrocarbon fuels. Furfural and dihydroeugenol were the chosen model compounds to represent cellulose and lignin fraction of biomass. Discerning the role of catalyst descriptors and hydrogen pressure were the main objectives of the study. A bimetallic catalyst system comprising platinum as a hydrogenation function and an oxophilic promoter molybdenum supported on multi-walled carbon nanotubes (MWCNT) was used to achieve 100% hydrodeoxygenation. Furthermore, a series of Pt-Mo catalysts were tested to elucidate roles of Pt and Mo in the reaction network. Finally hydrogen partial pressure was shown to have a defining say in the dominant reaction scheme in the network and hence in the final product distribution as well. Scanning transmission electron microscopy combined with electron energy loss spectroscopic analysis on the 5%Pt-2.5%Mo/MWCNT revealed that 77% of nanoparticles were bimetallic Pt-Mo. X-ray absorption spectroscopy also confirmed the presence of Pt-Mo alloy and that Mo was partially reduced with an average oxidation state of 0 and +4.

In case of furfural, four major routes observed were: Decarbonylation, reduction of aldehyde, furan-ring hydrogenation and furan-ring opening. Out of these decarbonylation

was undesirable since it leads to loss of carbon in the form of carbon monoxide whereas reduction and furan-ring opening reaction are a result of C-O scission and hence desirable. Increasing the hydrogen pressure as well the relative Mo loading on the catalysts are reported to have significant role in increasing the C-O bond scission selectivity.

Dihydroeugenol (DHE) is an aromatic ring with three substituents: alkyl, hydroxyl and methoxy. These substituents are characteristic of most of the compounds derived from a variety of lignin depolymerization processes such as pyrolysis/hydropyrolysis, organosolv extraction et cetera. Previously, the efficacy of Pt-Mo bimetallic catalyst system in complete hydrodeoxygenation of DHE to propylcyclohexane at 2.4 MPa hydrogen pressure was shown. In this work, hydrogen pressure was shown to have an impactful role in the distribution of aromatic to saturated hydrocarbon. At atmospheric pressure hydrogen, the yield of propylbenzene was 93.2%, and the pathway was deduced to be a result of direct deoxygenation of 4-propylphenol. Methoxy deoxygenation is proposed to occur through 4-propyl-1,2-benzenediol intermediate which subsequently deoxygenated to 4-propylphenol. Additionally, reaction site time yields and selectivity were compared to monometallic Pt and Mo catalyst in order to gain an understanding of their individual roles. Combination of results from catalyst characterization and kinetic studies over a series of Pt-Mo catalysts suggest that the overall site time yield was proportional to Pt loading, whereas the selectivity toward C-O scission products increased as the relative Mo to Pt ratio increased.

CHAPTER 1. INTRODUCTION

1.1 Dependence on fossil fuels

A grand challenge of 21st century is to provide a viable source of energy as development spreads to different corners of the world. In recognition of this, United Nations has unanimously declared 2014-2024 as the 'Decade of Sustainable Energy for All.'[1] Our reliance on fossil fuels can be evidenced by the fact that currently greater than 83% of our energy demands are provided through one form or other of the fossil fuels.[2] However, many studies indicate that fossil fuel generation will decrease in coming years, exhorting us to look for alternative means of energy to satisfy our energy needs.[3] The demand of energy is ever-increasing, in fact according to a recent International Energy Agency report the world population in the last 20 years increased by 27%, and per capita energy consumption increased by 10%. This clearly underlines a need to prepare for an eventuality where there would be a need to supplement existing fossil fuel resources with renewable energy.

Furthermore, fossil fuels account for almost all the energy-related carbon dioxide emissions.[4] Although there are conflicting reports on when we will reach the tipping point, it is generally agreed that continued carbon dioxide emissions will cause irreversible damage to the environment. While there are efforts by governments of many

countries to subsidize clean fuel technologies, the emissions continue to rise unabated partly due to fast developing economies of BRICS countries.

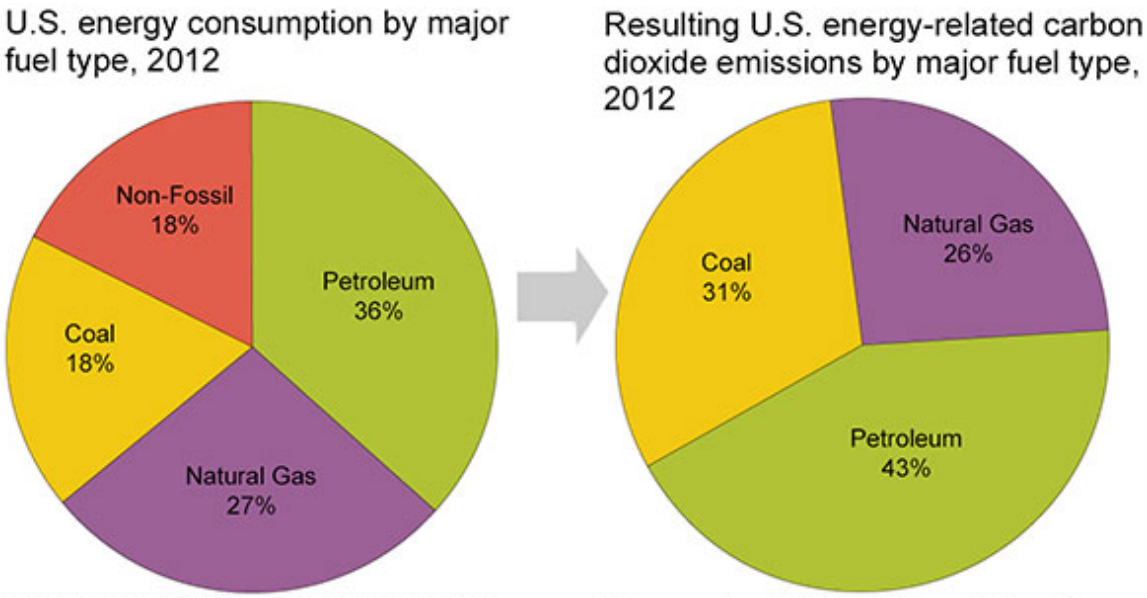

Figure 1.1 2010 U.S. energy consumption and energy related CO_2 emissions share by fuel[4]

1.2 Alternative energy resources

Of the alternative energy options, currently only nuclear and solar energy have the potential to fulfill enormous energy demands of the growing world. Amount of incident solar energy per year is ~10,000 times higher than estimated annual energy consumption of the world.[5] However, harnessing solar energy to efficiently transform to various energy forms we currently use is a challenge. Transportation sector alone is responsible for about 27% of the total energy consumed, of which greater than 90% is derived from petroleum based fuels.[6] Petroleum fuels dominate the transportation sector because of the extremely high energy density (volume equivalent), ease of use, and the existing

infrastructure. Currently, researchers have been studying viability of hydrogen-fuel cells, electric vehicles and liquid fuels derived from biomass as potential replacements.[7] The first two options according to present estimates are much less energy dense, therefore posing economic challenges to replace gasoline. Furthermore, 7-10% of world crude oil production is diverted to petrochemicals industry for producing valuable olefins and aromatics.[8] The net production rate of petrochemicals has continuously seen an upward trend and in the coming decades an alternative source would be required to continue using popular products like synthetic textiles, rubbers, electronic gadgets et cetera.

1.3 Biomass transformation routes to fuels

Biomass is the only sustainable source for both the carbon compounds and fuels which can use the same infrastructure that has been developed for petroleum. Using biomass as a feedstock would have two additional benefits, environmental and energy-independence. Fuels from biomass are considered carbon neutral since all carbon dioxide that is released from combustion is captured by the future cycles of biomass growth. Also, developing an energy system centered on biomass would help many countries lessen their reliance on other regions of the world for supply of primary energy. However, the biomass conversion route is also fraught with challenges. One of them is low bulk and energy density of biomass (150 kg/m^3) compared to petroleum oil (850 kg/m^3), leading to high transport costs. Moreover, the oxygen content of biomass is about 35-40% by weight compared to <1% for crude oil.[9] Both these reasons dictate that transformation of biomass to a high energy density form at a local facility has the potential to have an economic edge over those which rely on long-distance transportation. This energy form is

envisioned to be low in oxygen content so that it is stable as well as amenable to be fed to existing refinery infrastructure.

Major constituents of lignocellulosic biomass include cellulose (30-50%), hemicellulose (15-30%) and lignin (10-30%).[10] Cellulose is a linear polymer composed of repeating six carbon glucose units primarily linked to one another by glycosidic bonds. Hemicellulose is a branched polymer consisting of five and six carbon monosaccharide units that link cellulose fibers into microfibrils as well as cross-link with lignin. Lignin comprises of three monomer units: p-coumaryl alcohol, guaiacyl alcohol and syringyl alcohol. Lignin is a three-dimensional amorphous polymer with an aromatic backbone which provides individual fibers with strength. The relative proportion of its three building blocks is dependent on type of biomass. Among the constituents, lignin has the lowest oxygen to carbon ratio.

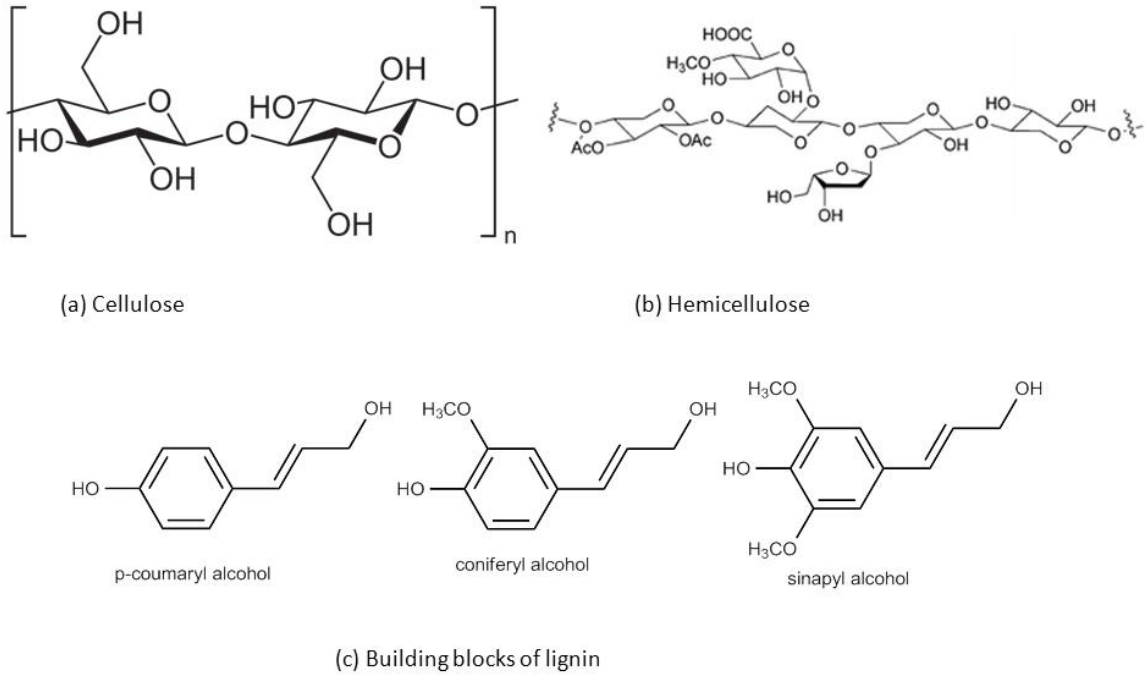

Figure 1.2 Cellulose, hemicellulose and lignin chemical structure[11,12]

Most of the biomass processing options can be either classified under the biological conversion route or the thermochemical conversion route.[10] First generation biofuels were produced from biological conversion route, including the widely studied ethanol. Since, these are relatively volatile, as well as retain oxygen and thus water solubility; they are limited in use and can be blended only to a certain extent to petroleum based fuels. Moreover, this route only utilizes the sugar fraction of biomass, with rest of the carbon (up to 25%) generated as a waste by-product. In order to surpass the 'blend-wall' and to utilize the entire plant, second generation biofuels were developed based on thermochemical technologies.

This route involves thermally treating biomass or its hydrolyzed constituents with or without a catalyst to produce fuel-like compounds and various other valuable chemicals. Among these, aqueous-phase processing of sugar molecules, gasification and pyrolysis have been prevalent technologies. Biomass feedstocks are available in wide variety such as starch, energy crops, food waste, forestry residues, urban municipal waste etc. Within a single type of feedstock as well, there can be varying proportion of constituents which can have different properties. It is unlikely that a solitary process will be optimum for all these feedstocks and their respective constituents. For example, bagasse a waste by-product from sugarcane industry has 40-50% water content; it could be improvident to dry it for gasification or pyrolysis processing.[13] On the contrast, it may not be good economics to lower carbon efficiency from energy crops, where using processes like pyrolysis it may be possible to convert most of the carbon in plant material to liquid product.

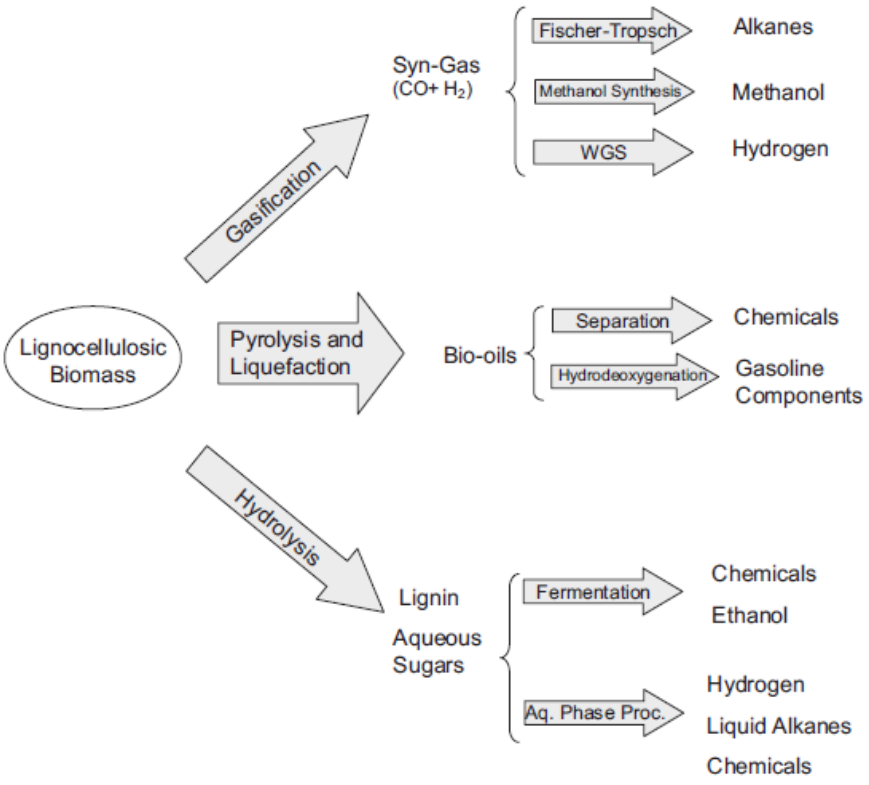

Figure 1.3 Thermochemical treatment options Serrano-Ruiz et al.[14]

None of thermochemical treatments have been shown to produce hydrocarbon compounds standalone without the use of a catalyst. Catalysts therefore hold the key to transform the biomass or thermal decomposition products from biomass in to fungible transportation fuels. However, the current understanding behind the operating parameters and catalysts in these processes is limited. Since biomass feedstocks have such varied components and products of thermal treatments are even more diverse, it is prudent to perform studies on model reactions and apply the gained information to a real system.

Researchers at University of Wisconsin, Madison have proposed aqueous phase reforming of biomass to utilize the sugar fraction of biomass to make hydrocarbon fuels,

hydrogen and other platform chemicals.[15–17] This process is one of the promising methods to produce hydrogen from a renewable biomass source with high yields over Pt-based catalysts. Parsell et al. have reported a concept of recovering lignin from intact biomass using a single step catalytic transformation to selectively produce 2-methoxy-4-propylphenol and 2,5-dimethoxy-4-propylphenol.[18] In contrast to these technologies, gasification and pyrolysis utilize all biomass constituents and without use of solvent resulting in significant savings in terms of operating costs.

1.3.1 Pyrolysis

Pyrolysis can process intact biomass to transform all constituents into useful products. Fast pyrolysis involves rapidly heating biomass in an inert atmosphere up to 500°C which results in breakdown of its constituents to liquid products collectively named bio-oil. The process of heating up biomass to vaporize and condensation to bio-oil is completed in a matter of 1-10 seconds.[19] Bio-oil retains an oxygen content of 35-50% similar to parent biomass and a low pH.[20] Also, the energy content of bio-oil is in the range of 16-19 MJ/kg compared to ~40 MJ/kg of gasoline. As the bio-oil is aged, the reactive oxygen functional groups lead to degradation reactions which increase viscosity, average molecular weight and thus instability. During the upgrading process, while reheating/ vaporizing the bio-oil, polymerization reactions are known to occur which may further lower the overall efficiency of the process.[21]

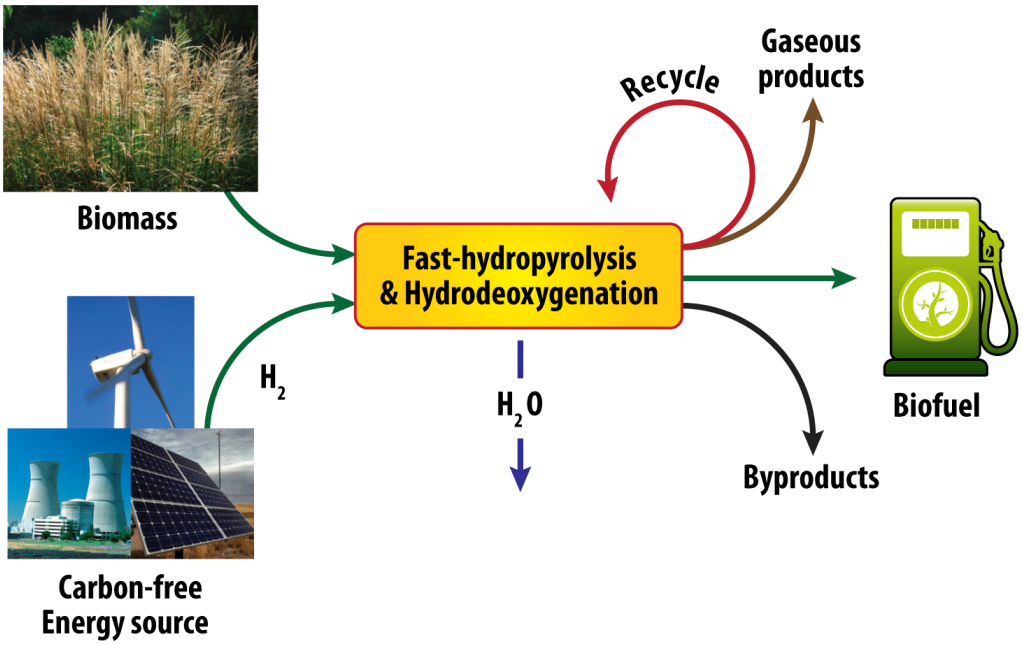

Figure 1.4 Concept of H_2Bioil process[22] (© R. Agrawal)

Agrawal and Mallapragada have argued that biomass should be primarily viewed as a carbon resource, not only as an energy source.[23] Keeping this in mind, Agrawal and co-workers,[22,24–26] have proposed a series of hybrid approaches based around fast hydropyrolysis to collect a stable liquid product with a view to maximize carbon yield in the liquid. One of them called the H_2Bioil process, involves pyrolyzing biomass in presence of high pressure hydrogen followed by in-line vapor phase catalytic hydrodeoxygenation to produce transportation fuel. This process overcomes few of the issues with conventional hydrotreating processes as the collected liquid product is envisioned to be free of the reactive oxygen functional groups. The argument for using high pressure hydrogen is motivated from traditional hydrotreating processes where use of high pressure hydrogen is instrumental in successful desulfurization of the refinery

feedstock.[27] Singh et al. reported a detailed economic analysis of H_2Bioil process revealing that depending on the hydrogen source the break-even price for this process could be in the range of $103-$143/bbl of crude oil.[28]

1.4 Thesis objectives

In a broader sense the goal of this dissertation was to identify descriptors for optimization of biomass transformation reactions to produce fuels via fundamental kinetic studies. In this dissertation, following projects are discussed:

1.4.1 Liquid-phase water-gas shift reaction

Water gas shift (WGS) reaction is considered to be one of the hydrogen producing steps in aqueous phase reforming of biomass-derived oxygenates.[29] However, the quantification of water-gas shift reaction rate in liquid-phase conditions is not known. Pt and Pt-Mo catalysts have been reported to have different selectivity toward hydrogen production in aqueous phase reforming. The idea then was to estimate the rate of WGS reaction for both Pt and Pt-Mo catalysts under aqueous phase reforming conditions and explain the difference in hydrogen production. Furthermore, comparing the kinetics of WGS reaction in both gas-phase and liquid-phase may help bridge the gap.

1.4.2 Millisecond timescale hydropyrolysis of cellulose

In literature, there is a debate about the pathway of cellulose hydropyrolysis.[30] Studies performed on a milligram timescale in a batch reactor exhibit a product distribution which is different from continuous feed lab-scale reactor. The goal in this project was to

design and operate a continuous-feed millisecond residence time scale in order to bridge the gap between two scales of reactor design which would help resolve the cellulose hydropyrolysis reaction pathway.

1.4.3 Hydrodeoxygenation kinetics of furfural over a series of Pt-Mo catalysts

Catalytic hydrodeoyxgenation of biomass-derived oxygenates has been typically carried out at atmospheric pressure hydrogen in contrast to current hydrotreating processes in the refinery. The influence of hydrogen pressure is unknown in the literature and there is a need to carry out detailed experimental analysis as expressed in a recent review paper. Moreover, utilizing extensive catalyst characterization in tandem with kinetic studies it is proposed to determine the structure-activity relationship.

1.4.4 Dihydroeugenol hydrodeoxygenation: Role of hydrogen, Pt and Mo

Dihydroeugenol a lignin-based model compound is reported to undergo ring hydrogenation followed by methoxy and hydroxyl losses to produce saturated hydrocarbon at 2.4 MPa hydrogen pressure over the bimetallic Pt-Mo catalyst.[31] The aim of this study was to perform a detailed hydrogen pressure study and reveal its effect on the pathway of hydrodeoxygenation and the final product distribution. Furthermore, it was envisioned to elucidate the role of Pt and Mo in the reaction pathway.

CHAPTER 2. KINETICS OF THE LIQUID PHASE WATER-GAS SHIFT REACTION ON PLATINUM-BASED CATALYSTS

2.1 Abstract

The water-gas shift (WGS) reaction was carried out in liquid-phase in a stirred tank reactor at 4 MPa over Pt and Pt-Mo catalysts supported on norit-carbon and multi-walled carbon nanotubes (MWCNT). The objective of this work was to measure the kinetics for the WGS reaction in aqueous phase reforming conditions. The turnover frequency (TOF) under reaction conditions of 160°C, P_{CO} = 0.4 MPa, P_{H2} = 0.4 MPa, P_{CO2} = 0.02 MPa, P_{H2O} = 0.5 MPa was $3.3 \cdot 10^{-2}$ s^{-1} for Pt-Mo/MWCNT, four times higher than the TOF of $7.4 \cdot 10^{-3}$ s^{-1} measured on monometallic Pt/MWCNT. The apparent activation energy measured for Pt-Mo/MWCNT was lower than Pt/MWCNT for both gas-phase and liquid-phase WGS. The kinetics for liquid-phase WGS follow $[CO]^{0.88}[CO_2]^{-0.28}[H_2]^{-0.35}$ dependence for Pt/MWCNT and $[CO]^{0.89}[CO_2]^{-0.29}[H_2]^{-0.32}$ dependence for Pt-Mo/MWCNT, suggesting that Mo altered kinetics in a similar way for both gas-phase WGS and liquid-phase WGS.

2.2 Introduction

As world fossil fuel reserves diminish, the search for renewable sources of energy becomes even more urgent. Hydrogen has received considerable attention as a promising alternative source of energy or as a co-feed to biomass processing technologies to augment liquid fuels yield.[32] Currently hydrogen is produced primarily from non-renewable natural gas and petroleum.[33] Thus, the present challenge is to produce hydrogen using renewable and environmentally benign sources instead. One of the promising routes to produce hydrogen is aqueous reforming of water-soluble oxygenated compounds derived from biomass.[29,34] Cortright et al.[29], suggested a complex reaction network for aqueous phase reforming that includes the water-gas shift (WGS) reaction as an important hydrogen producing step. Thus, it is important to understand the WGS contribution to hydrogen production in aqueous phase reforming.

Water-gas shift has traditionally been an important industrial reaction for synthesis of ammonia, optimization of hydrogen/carbon monoxide ratio in steam reforming and minimization of carbon monoxide in fuel cell applications.[33] WGS is a reversible reaction wherein carbon monoxide reacts with water to give carbon dioxide and hydrogen. It allows maximization of hydrogen production and simultaneous minimization of toxic and undesirable carbon monoxide.

$$CO + H_2O \leftrightarrow CO_2 + H_2$$

Thus, WGS can be used as a secondary reaction to optimize the H_2/ CO ratio in the product stream.[35] WGS has already been studied extensively in gas-phase conditions over a variety of catalysts including noble metal catalysts like platinum, palladium, and gold.[33,36] The gas-phase WGS has typically been studied at a total pressure of 1 bar and temperature of 280-300°C for Pt catalysts. Liquid-phase reforming is carried out at 25 bar and temperatures of about 200-220°C.[37] In addition to this the phase of reaction is different for gas-phase WGS and liquid-phase reforming. Density functional theory (DFT) studies on the activation of water on Pt surfaces by Desai and Neurock[38] suggest that the activation barrier might be significantly reduced in presence of liquid water. This study was backed up by experimental evidence from He et al.[39] which also suggested that CO coverage on Pt/Al_2O_3 could be lowered in the presence of liquid water.

Determination of kinetics of WGS in liquid-phase thus becomes critical to accurately estimate the WGS rate under liquid-phase reforming conditions. There have been studies on Pt and Pt-Mo catalysts for aqueous phase reforming.[40] Therefore, liquid-phase WGS (LWGS) was studied over Pt and Pt-Mo catalysts supported on norit-carbon and multi-walled carbon nanotubes to elucidate the role of WGS in liquid-phase reforming.

In this work, we have determined the kinetics of the WGS reaction in liquid phase conditions. Water was both a solvent and a reactant in the WGS reaction. The reaction was carried out at temperatures of 130-160°C and high pressure (~4 MPa) to maintain liquid phase conditions. A stirred tank reactor was used to carry out the semi-batch

operation. The measured rate was proven to be kinetically controlled using the Koros-Nowak criterion.[41] The observed rate was modeled according to the power law:

$$r = k_o e^{-\frac{E_{app}}{RT}} P_{CO}^{a} P_{H_2}^{b} P_{CO_2}^{c}$$

We have also compared the kinetics of LWGS with gas-phase WGS, revealing agreement between liquid-phase data and extrapolated gas-phase data.

2.3 Experimental Methods

2.3.1 Catalyst preparation

Liquid phase water-gas shift was studied on Pt and Pt-Mo catalysts prepared by incipient wetness impregnation (IWI) on norit-carbon (C) and multi-walled carbon nanotubes (MWCNT).The norit-carbon catalysts were prepared by first depositing Pt using an aqueous solution of chloroplatinic acid hexahydrate (Strem Chemicals). This material was dried in air overnight at 120°C. For Pt-Mo/C catalysts a second impregnation was done using a molybdenum hexacarbonyl in THF solution to give a 1:1 Pt:Mo atomic ratio. Then, this catalyst precursor was dried in air overnight at 25°C. After drying, the material was reduced in flowing hydrogen for 2 hours at 450°C (0.6°C/min ramp). Finally, passivation of the catalyst was carried out at 25°C using a 2% O_2/He mixture.

Multi-walled carbon nanotubes (MWCNT) obtained from Cheap Tubes, Inc. were acid treated by refluxing the as-received nanotubes in concentrated nitric acid for 4 hours. Next, the MWCNT were washed in deionized water, centrifuged, and decanted for 15 washes.

The Pt/MWCNT catalyst was synthesized by IWI using an aqueous solution of tetraamineplatinum (II) nitrate. The wet catalyst was then dried in air overnight at 150°C. Before running the reaction the catalyst was reduced in flowing hydrogen for 2 hours at 400°C (2 hour ramp). The Pt-Mo/MWCNT catalyst was synthesized by sequential impregnation of aqueous solutions of tetraamineplatinum (II) nitrate and ammonium heptamolybdate tetrahydrate, with overnight drying in air at 60°C between impregnation steps. The salts were calculated to give weight loading of 5 percent Pt and 2.46 percent Mo, or 1:1 atomic ratio of Pt: Mo. The wet catalyst was then dried in air overnight at 150°C. Before running the reaction the catalyst was reduced in flowing hydrogen for 2 hours at 450°C (2 hour ramp).

2.3.2 Catalyst characterization

The platinum content of the catalysts was determined by inductively coupled plasma optical emission spectrometry (ICP-OES) test performed by Galbraith Laboratories, Knoxville, TN. The platinum particle size was determined by transmission electron microscopy (TEM) using an HRTEM FEI Titan 300kV. TEM samples were prepared by dissolving 1μg catalyst in 0.5ml ethanol, and dispersing the suspension in an ultrasonic bath for 5 minutes. The solution was then dropped onto 200 mesh lacey carbon-coated copper grids, and the grids were dried for 15 minutes at room temperature. The experimental setup and technique have been discussed in detail elsewhere.[42] The platinum dispersion was also measured by CO chemisorption in a standard volumetric Micromeritics ASAP 2020 instrument. The procedure consists of evacuation at 300°C for 8 hours. This evacuation is followed by H_2 reduction at 300°C for 120 min followed by

evacuation at the same temperature for 180 min. Analysis step was carried out at 35°C and a pressure range of 200-400 mmHg CO. A Pt/CO stoichiometry of 1 was assumed to estimate the moles of surface Pt. X-ray absorption spectroscopy (XAS) experiments were carried out at the Advanced Photon Source (APS) at Argonne National Laboratory.[43,44] Spectra were collected for three Pt/C catalyst samples: fresh catalyst reduced under flowing H_2 at 450°C for 2 hours, used catalyst for carrying out liquid-phase WGS reaction, and used catalyst for liquid-phase WGS and subsequently for chemisorption.

2.3.3 Kinetic studies

All the experiments for LWGS were carried out in a stirred tank reactor (Parr Instrument Co.) at 4 MPa and 130-160°C [Figure 2.1]. The capacity of this reactor without the internals is 500 ml. The reactor is equipped with a gas entrainment impeller, dip tube, thermowell and a pressure gauge. Inlet gas enters through the dip tube, ensuring that gas does not directly bypass to the outlet of reactor. Gas back mixing was achieved through an entrainment impeller which draws gas in the head space into its hollow stirring shaft when the impeller is operated above 600 rpm. Baffles are inserted into the reactor to avoid vortex formation and enhance liquid mixing.

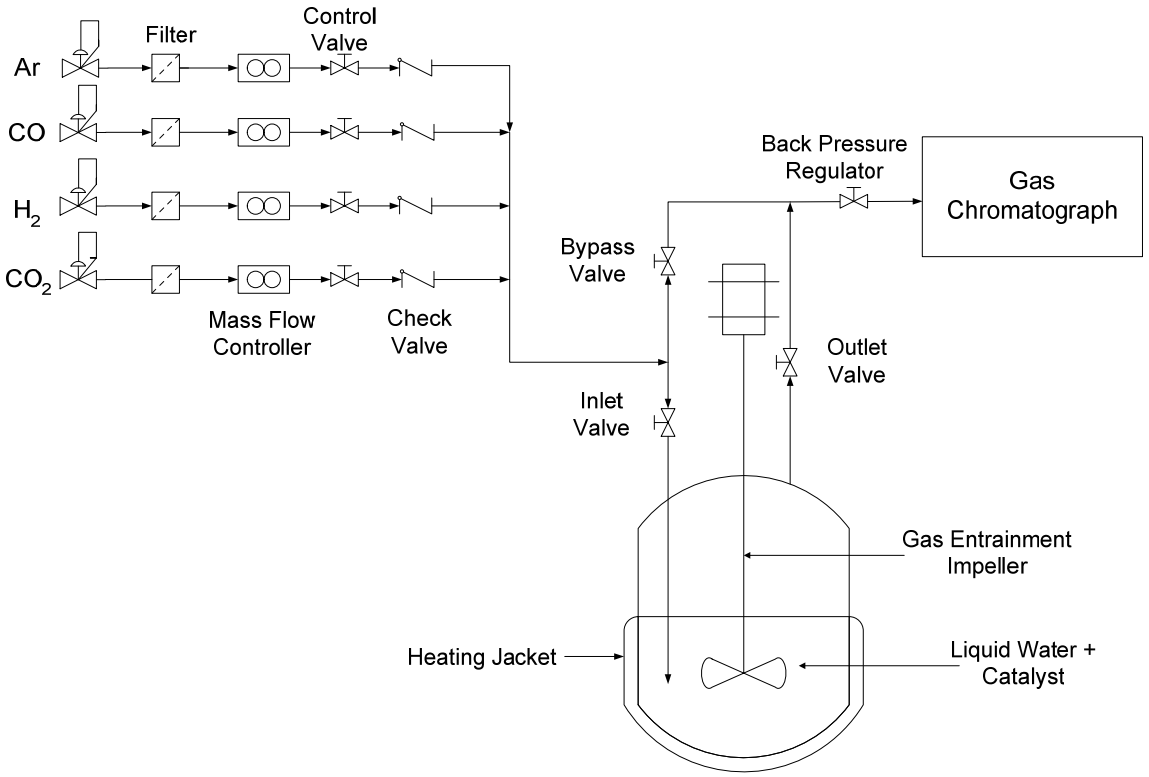

Figure 2.1 Process flow diagram of the experimental setup to study LWGS

The exit gas stream was analyzed using an online Agilent 7890 Gas Chromatograph (GC) equipped with a Thermal Conductivity Detector (TCD) and a Carboxen 1000 column. Helium was used as the carrier gas. In a typical run approximately 350 ml of water was loaded into the reactor along with the 0.7-1 g catalyst. At the outlet of reactor there is a vertical tube approximately 10 cm in length which allowed any entrained water droplets to coalesce and return to the reactor. Since only water saturated at room temperature is allowed to leave the reactor in the outlet gas stream we lost minimal quantities of water resulting in more than half of liquid water retained after 100 hours of experiments. Maintaining liquid water was important as no water was fed through the inlet stream and

water partial pressure would be controlled only if there was liquid water present in the reactor.

Before beginning reaction, the catalyst was reduced *in-situ* under 3 MPa H_2 and 1 MPa Ar for about 3-4 hours at 200°C. It was observed that the water-gas shift rate increased when the Pt/norit-C catalyst was exposed to 2.6 MPa CO for the first time and remained stable at the high value afterwards. Thus, the catalyst was exposed to 2.6 MPa carbon monoxide for about 4 hours until the exit gas concentration was constant before starting the kinetic measurements. Further details of this phenomenon are presented in the discussion section. After CO pretreatment the reactor was then pressurized to 4 MPa by flowing the feed gases (Ar, CO, CO_2 and H_2) through a bank of mass flow controllers into a gas manifold which is connected to the reactor inlet [Figure 2.1]. The total gas flow rate was 300 ml min^{-1} (10% CO, 10% H_2 and balance Ar). Argon served as an internal standard. The pressure was controlled using a back-pressure regulator at the exit of the reactor. Temperature was then increased to the set-point at about 5°C/min. Once the reactor reached steady temperature and pressure, analysis using gas chromatograph was started and gas samples were taken every 15 minutes. Using the bypass, the peak areas from the GC were calibrated against flow rates from the mass flow controllers. This calibration was then used to estimate the exit gas composition from the peak areas during the run. For a differential reactor, the rate per gram of catalyst can be directly computed from difference between inlet and outlet gas composition. This rate per gram of catalyst was further normalized to rate per moles of surface metal (TOF) using techniques described in the catalyst characterization section. It was observed that the value of rate

per moles of surface metal agreed to within 10% for replicate runs. The apparent activation energy was estimated over a temperature range of 30°C, keeping the gas composition constant. For the measurement of apparent reaction orders, the partial pressure of reactants and products was varied in the range of 0.4-2 MPa CO, 0.4-2 MPa H_2 and 0.2-0.6 MPa CO_2.

Gas-phase WGS was carried out in the unit described in Bollmann et al.[45] This unit has four parallel plug flow reactors operated under differential conditions. About 200-250 mg of catalyst sample was loaded into the reactor. The catalyst was reduced prior to the kinetic measurements using 25% H_2 and balance Ar with a total flow rate of 50 ml min^{-1} at 300°C for 2 hours. The catalyst is then stabilized at 300°C for 20 hours to obtain a steady reaction rate value. Further details on treatment conditions for Pt catalysts are described in Pazmiño et al.[46]

2.4 Results

2.4.1 Catalyst characterization

Table 1 lists the catalysts used, metal loading, and the average metal particle size derived from TEM measurements. The dispersion was calculated from the relation that the dispersion is equal to the inverse of the average particle size in nm.[47,48]

Table 2.1 Percentage Pt loading and particle size/dispersion by TEM for catalysts

Catalyst	% Pt Loading (ICP-OES)	Particle Size/ nm		Dispersion	
		Fresh	Used	Fresh	Used
5% Pt/C	4.8	2.2	4.3	0.45	0.23
1%Pt/C	1	1.7	4.3	0.59	0.23
5%Pt-Mo/C	4.5	2.3	2.6	0.43	0.39
5% Pt/MWCNT	-	2.2	3.7	0.46	0.27
5% Pt-Mo/MWCNT	-	2.9	3.3	0.34	0.30

The comparison for fresh and used catalysts, shown in Figure 2.2 and Figure A1.1 indicates that the catalysts have sintered during use. However, it is important to note from (b) and (c) in Figure A1.1 that the metal particle size after CO activation was more or less the same as it was after the kinetics were measured.

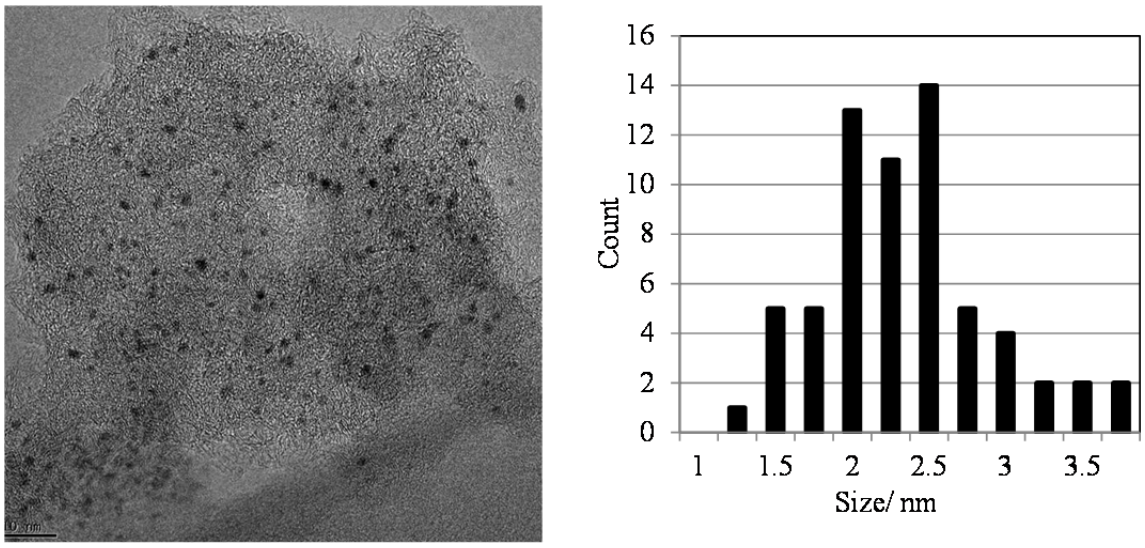

Figure 2.2 TEM Image and size distribution for fresh 5%Pt/C

The average particle size from TEM for the 5%Pt/C is in agreement with the results obtained from XAS experiments [Table 2.2]. The average particle size was determined from the average metal-metal coordination number as detailed in Miller et al.[43,49]

Table 2.2 Average particle size for the 5% Pt/C from XAS

Treatment	Scatter	N	R/ Å	Debye Waller factor (x 10^3)	E_o/ eV	Size/ nm
Fresh	Pt-Pt	6.8	2.73	2.0	-3.0	2.0
Used, After High Pressure CO	Pt-Pt	9.8	2.73	1.0	-2.5	5.0
Used, After LWGS and Chemisorption	Pt-Pt	9.8	2.73	1.0	-2.6	5.0

2.4.2 Proof of kinetic control

Variation of agitation speed, variation of total gas flow rate and changing the active material concentration (Koros-Nowak criterion) were used to test for heat and mass transport limitations.[41]

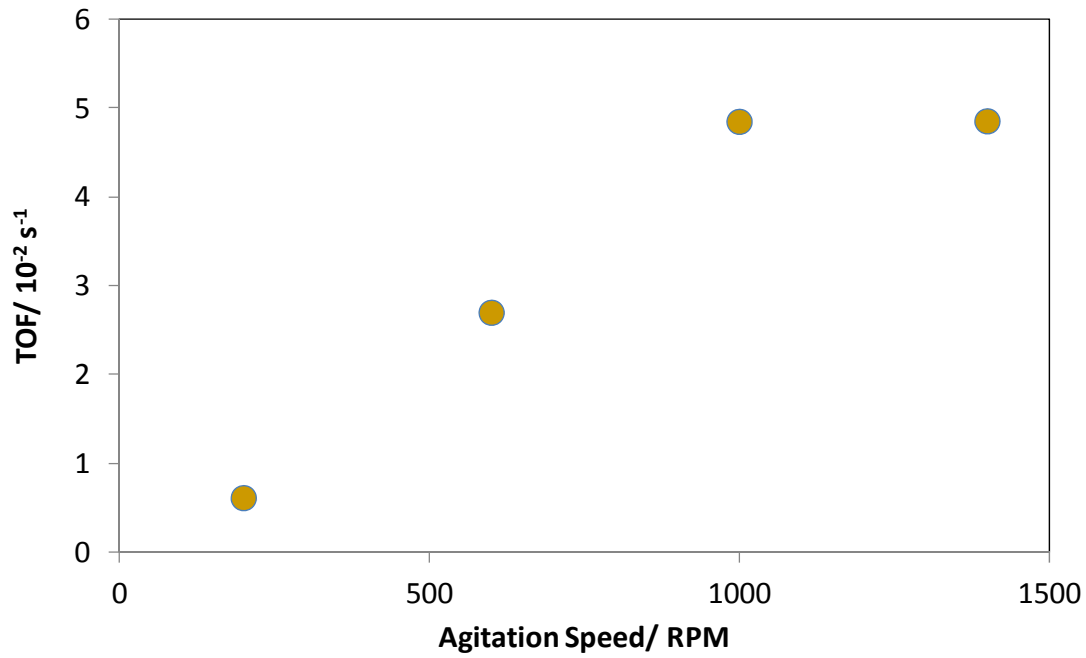

Figure 2.3 Effect of agitation speed on measured rate to determine the minimum agitation speed above which TOF remains constant

The rate of reaction was measured as a function of agitation speed (Figure 2.3), and the reactor was operated at an agitation speed above which the TOF was constant. No effect of total gas flow rate was observed on TOF as evidenced by similar TOF's obtained for 5%Pt/C for 100sccm ($4.7 \pm 0.4 \cdot 10^{-3}$ s^{-1}) and 300sccm ($6.9 \pm 0.6 \cdot 10^{-3}$ s^{-1}) gas flow rates.

Finally, we used the Koros - Nowak criterion, which states that in the kinetic regime the TOF must be invariant as the concentration of active material is changed.[41,50] Two catalysts with different Pt loading but similar dispersion were synthesized and tested for this purpose. For LWGS, the TOF for 5%Pt/C was ($6.9 \pm 0.6 \cdot 10^{-3}$ s^{-1}) and for 1%Pt/C was ($5.8 \pm 0.6 \cdot 10^{-3}$ s^{-1}), thus the data suggest that TOF is independent of the metal

loading on the catalyst at dispersion values of about 0.23 for both catalysts. Collectively, these kinetic results indicate that the rate measurements in this study are not influenced by heat and mass transport limitations.

2.4.3 Kinetics

The turnover frequencies reported are per surface metal atom, as calculated from average particle size estimated by TEM images. The apparent activation energy and reaction orders with respect to CO, H_2 and CO_2 were determined in the following way. Each set of experiments were started at standard conditions to check for deactivation. The rates at these standard conditions were reproduced to within 10%.

Table 2.3 Kinetics of WGS reaction in gas-phase and liquid-phase for Pt and Pt-Mo catalysts

	LWGS Pt/C	LWGS Pt/MWCNT	LWGS PtMo/C	LWGS PtMo /MWCNT
TOF*/ 10^{-3} s^{-1}	6.9 ± 0.6	7.4 ± 0.6	50 ± 5	33.2 ± 5
E_{app}/ kJ mol^{-1} (Temperature Range/ °C)	82 ± 3 (150-180)	80 ± 3 (150-180)	76 ± 2 (110-150)	69 ± 6 (150-180)
N_{CO} (P_{CO} Range/ MPa)	0.47 ± 0.08 (0.4-2.6)	0.88 ± 0.08 (0.4-2.6)	0.22 ± 0.01 (0.4-2.6)	0.89 ± 0.06 (0.4-2.6)
N_{H2} (P_{H2} Range/ MPa)	-0.33 ± 0.06 (0.4-2.6)	-0.35 ± 0.06 (0.4-2.6)	-0.35 ± 0.03 (0.4-2.6)	-0.32 ± 0.04 (0.4-2.6)
N_{CO2} (P_{CO2} Range/ MPa)	-0.30 ± 0.08 (0.2-0.6)	-0.28 ± 0.08 (0.2-0.6)	-0.30 ± 0.05 (0.1-0.4)	-0.29 ± 0.03 (0.2-1)
Temperature/ °C	160	160	130	160

*LWGS TOF normalized by Pt surface area from TEM to Reaction Conditions:
T = 160°C, P_{CO} = 0.4 MPa, P_{H_2} = 4 bar, P_{CO_2} = 0.02 MPa, P_{H_2O} = 0.5 MPa

Table 2.4 Kinetics of WGS reaction in gas-phase and liquid-phase for Pt and Pt-Mo catalysts

	WGS Pt/C	WGS PtMo/C	WGS Pt/MWCNT	WGS PtMo/MWCNT
TOF*/ 10^{-3} s^{-1}	11.7 ± 1.8	6.2 ± 1	2.7 ± 0.4	6.8 ± 1
E_{app}/ kJ mol^{-1} (Temperature Range/ °C)	71 ± 6 (290-320)	72 ± 6 (270-300)	82 ± 2 (260-290)	61 ± 3 (215-245)
N_{CO} (P_{CO} Range/ MPa)	0.14 ± 0.06 (0.004-0.021)	0.19 ± 0.01 (0.004-0.021)	0.12 ± 0.03 (0.004-0.021)	0.15 ± 0.02 (0.004-0.021)
N_{H2} (P_{H2} Range/ MPa)	-0.33 ± 0.04 (0.014-0.055)	-0.24 ± 0.03 (0.014-0.055)	-0.44 ± 0.01 (0.014-0.055)	-0.28 ± 0.01 (0.014-0.055)
N_{CO2} (P_{CO2} Range/ MPa)	-0.08 ± 0.03 (0.005-0.025)	-0.09 ± 0.01 (0.005-0.025)	-0.06 ± 0.01 (0.005-0.025)	-0.04 ± 0.02 (0.005-0.025)
Temperature[a]/ °C	300	278	270	225

a: Temperature used in the order measurements and for rate measurement

*Gas-phase WGS TOF normalized to Pt surface area from chemisorption to Reaction conditions:

$P_{CO} = 0.007$ MPa, $P_{H_2} = 0.037$ MPa, $P_{CO_2} = 0.011$ MPa, $P_{H_2O} = 0.022$ MPa

2.4.4 Gas-phase WGS vs. LWGS (Pt/C and Pt/MWCNT)

Table 2.3 and 2.4 entails the experimental conditions and kinetics measured for liquid-phase WGS (LWGS) and gas-phase WGS for all the catalysts. The measured apparent activation energies of all the catalysts are within the range 65-85 kJ mol^{-1}. However, it is important to note that the temperature range over which the activation energies were measured differs for liquid and gas-phase WGS. The carbon monoxide order in LWGS is observed to be 0.5 for Pt/C, significantly higher than 0.14 obtained for gas-phase WGS. When compared with gas-phase WGS, the hydrogen order is similar to that obtained for LWGS, however, it is measured at a high pressure range. The carbon dioxide order in LWGS is -0.30 whereas for gas-phase WGS the order is -0.08.

Pt/MWCNT catalyst was investigated for LWGS to check whether the CO activation phenomenon was observed as in Pt/ C, or the CO activation is attributable to the carbon support. We found that the TOF for Pt/MWCNT ($7.4 \pm 0.6 \cdot 10^{-3}$ s^{-1}) was comparable to Pt/C ($6.9 \pm 0.6 \cdot 10^{-3}$ s^{-1}). We did not observe any change in measured TOF when the catalyst was exposed to 2.6 MPa CO. This tells us that CO activation phenomenon is an artifact of the norit-C support. Kinetic measurements were also performed on this Pt/MWCNT catalyst. The activation energy (~75 kJ mol^{-1}), hydrogen order (~-0.35) and carbon dioxide order (~-0.30) were similar to corresponding measurements for Pt/C. However, the CO order of 0.88 for Pt/MWCNT was higher than the value of 0.5 reported for Pt/C.

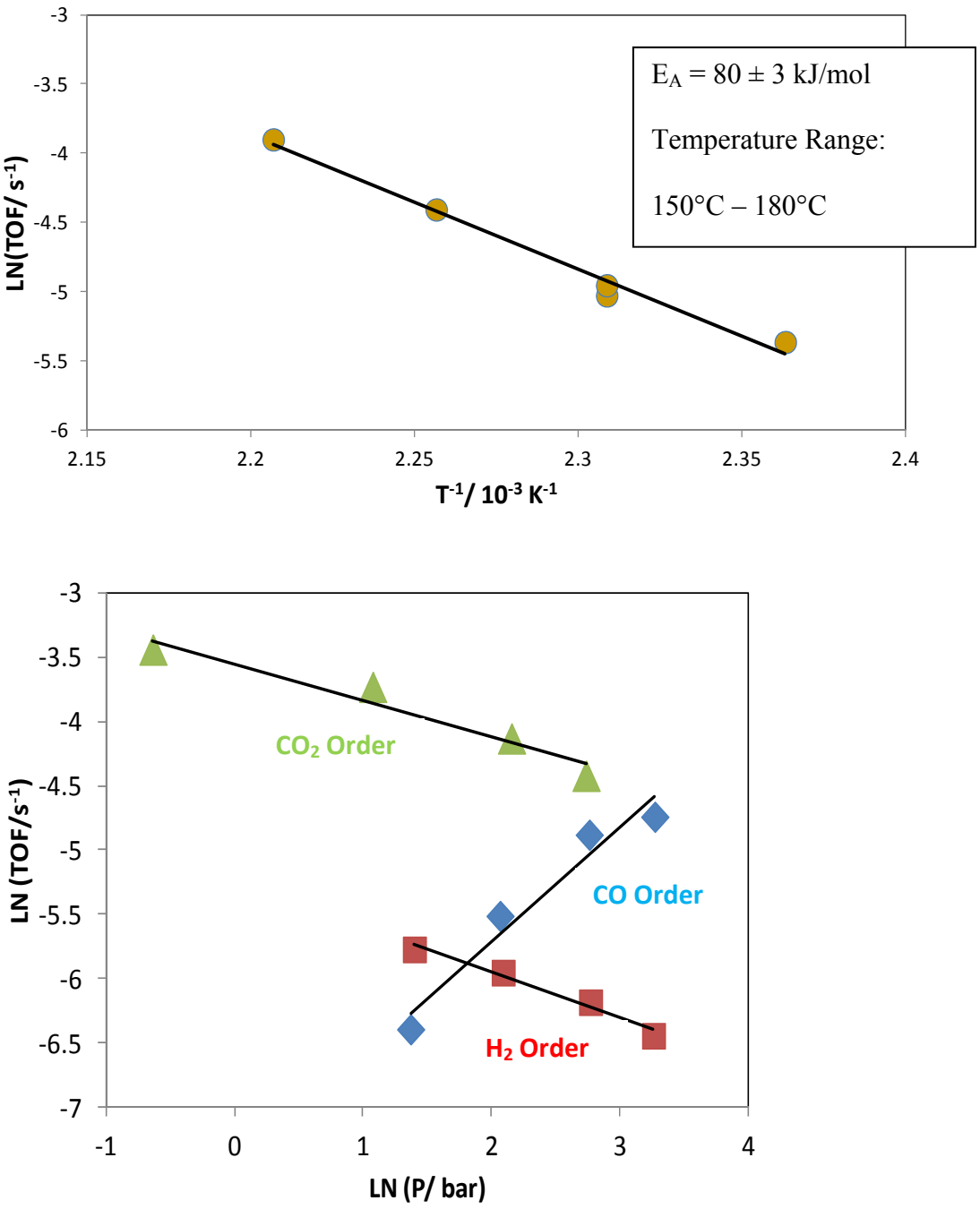

Figure 2.4 Kinetic studies on Pt/MWCNT (a) Arrhenius plot for estimating activation energy, (b) Order plot for CO, H2 and CO_2

2.4.5 Pt/MWCNT and Pt-Mo/MWCNT

One of the objectives of this study was to evaluate the effect of Mo as a promoter for WGS reaction. The TOF obtained for Pt-Mo/MWCNT is $3.3 \cdot 10^{-2}$ s^{-1}, or approximately 4 times higher than $7.4 \cdot 10^{-3}$ s^{-1} for Pt/MWCNT. The apparent activation energy for Pt-Mo/MWCNT is lower than Pt/MWCNT for both LWGS and gas-phase WGS [Table 2.3 and 2.4]. The reaction orders were similar between both catalysts for CO (0.88 and 0.89), H2 (-0.35 and -0.32) and CO_2 (-0.28 and -0.29). For Pt/C and Pt-Mo/C, measured kinetics were similar except for CO order (0.47 and 0.22), which was higher for Pt/C.

2.5 Discussion

2.5.1 Comparison between LWGS and gas-phase WGS – Pt

It is important to identify the relevant parameters when comparing the gas-phase WGS results to LWGS. Gas phase kinetics were measured at a temperature of 280°C and a pressure of 0.1 MPa (Partial pressure of CO = 0.011 MPa, H_2 = 0.037 MPa, CO_2 = 0.005 MPa, H_2O = 0.022 MPa, balance Ar) compared to a temperature of 160°C and a pressure of 4 MPa (Partial pressure of CO = 0.4 MPa, H_2 = 0.4 MPa, CO_2 = 0.02 MPa, H_2O = 0.5 MPa, balance Ar) for LWGS. Apparent activation energy was found to be within the range of 65-85 kJ mol^{-1} for both catalysts in gas-phase WGS and LWGS. However, during LWGS it is not possible to decouple the effects of water partial pressure and temperature due to the vapor-liquid equilibrium of water. We have assumed that vapor pressure of water is equal to the partial pressure of water, a valid assumption under Raoult's law for a single component liquid. Because partial pressure of water is a function of temperature, what is measured is actually a lumped parameter encompassing

effects of temperature and water partial pressure, not apparent activation energy alone. However, as the operating water partial pressure (0.5 MPa) is much greater than gas-phase WGS water partial pressure (0.022 MPa), the water order in LWGS should be lower than the observed water order for gas-phase WGS (order ~0.6). The equation given below shows the relationship between water order and activation energy derived by fitting the exponential dependence of water vapor pressure with temperature (see Appendix A for details).

$$E_{app} = E_{app}^{measured} - 41 \times N_{H_2O}$$

There were three main parameters affecting the coverage of reactants or products on the catalyst, and thus the observed reaction orders. The first parameter was reaction temperature. LWGS rates were measured at a lower temperature of 160°C as opposed to gas-phase WGS rates at 300°C. It is expected that the coverage will increase at lower temperatures. The second parameter was the partial pressure range. For each gas the pressure range over which the order was measured for LWGS was much higher than the range for gas-phase WGS, which leads to increased coverage for each gas. Also, water partial pressure is much higher in LWGS (0.5 MPa) as compared to gas-phase WGS (0.022 MPa), so it is very likely that water coverage in LWGS will be higher compared to gas-phase WGS. This higher coverage of water will have an adverse effect on coverage of other gases because of competitive adsorption. It has been established that the coverage of each gas component will be higher in LWGS than gas-phase WGS due to lower temperature and higher partial pressure of gases, but will decrease due to the higher

partial pressure of water. For reactants the order is inversely related to coverage. Conversely, as the coverage of products increases as it inhibits the reaction, leading to a more negative order.

Carbon monoxide order for Pt/MWCNT in LWGS is 0.88, compared to 0.19 in WGS; this means that the carbon monoxide coverage in LWGS is lower than in WGS. Thus, competitive adsorption between carbon monoxide and water plays a major role. Hydrogen order is similar for LWGS and WGS, and this can be explained by competition between pressure of operation and competitive adsorption with water. Carbon dioxide is more inhibiting in LWGS compared to WGS. This could be due to higher partial pressure of CO_2 and lower temperature of operation

2.5.2 Comparison between Pt and Pt-Mo/MWCNT

LWGS is observed to be 4 times faster for Pt-Mo/MWCNT as compared to Pt/MWCNT. A similar promotion ratio (~ 3) is also observed for gas-phase WGS. Also, it can be seen that for both LWGS and gas-phase WGS the apparent activation energy is lower for Pt-Mo/MWCNT compared to Pt/MWCNT. This shows that Mo modifies the kinetics of LWGS in a similar way as in gas-phase WGS.

However, in the case of norit-carbon supported catalysts, a promotion factor of about 10 was observed for Pt-Mo when compared to Pt for both LWGS and gas-phase WGS. When comparing kinetics it is observed that only CO order is different. There is one

caveat while comparing kinetic parameters between Pt/C and Pt-Mo/C: The temperature of operation for Pt/C (160°C) was higher than Pt-Mo/C (130°C).

2.5.3 Effect of high pressure CO on Pt/C reaction rate and possible presence of sulfur

When the Pt/C catalyst was exposed to 2.6 MPa CO for the first time, an increase in the measured rate was observed. The high rate value was reproducible for subsequent runs. One of the reasons for this phenomenon could be presence of sulfur covering the Pt on the catalyst. During catalyst preparation the catalyst is pre-reduced at 400°C before being loaded into the reactor. Sulfur impurities from the carbon support could migrate to the platinum due to high temperature of pre-reduction. A sulfur-poisoned Pt catalyst would have shown a low rate initially. Sulfur could then have been driven out on exposure to a high pressure of carbon monoxide, increasing the observed rate. Studies on model catalysts have suggested that carbon monoxide has the capability to drive out or compress sulfur on Pt.[51,52] This theory is corroborated by the chemisorption results. Since the carbon support is high surface area, degassing for used catalyst (exposed to liquid water) requires treatment at 300°C for 6-8 hours. The prolonged exposure to high temperature can result in sulfur covering Pt again. On the other hand, the fresh Pt/C sample was degassed at 150°C. The dispersion shown after chemisorption is lower by 5-6 times as compared to the one calculated from TEM images for the used sample, in contrast to similar values of dispersion obtained for fresh sample by chemisorption and TEM. Lower dispersion can be caused by either increased particle size or a decrease in surface Pt sites by a catalyst poison. Since TEM indicated only a modest increase in the particle size, we suspect sulfur as a poison, because it is a known contaminant in carbon supports.

Table 2.5 Comparison of dispersion of fresh and used Pt/C samples using TEM and chemisorption

	Dispersion from TEM	Dispersion from Chemisorption
Fresh 5% Pt/C	0.45	0.34
Used 5% Pt/C	0.23	0.05

We tested the hypothesis that sulfur could be covering Pt aggregates on the support by XAS experiments on three samples of Pt/C catalysts. Samples that were fresh (after reduction at 400°C), used in LWGS, and used LWGS samples after chemisorption were each scanned. Sulfur co-ordinated with Pt in catalysts would be evidenced by a large peak at about 1.8 Å as detailed in Pazmiño et al.[44]

This evidence of Pt-S bonds was absent in all three samples. The XAS spectrum is shown in Figure 2.5 for all three catalysts along with the interpretation.

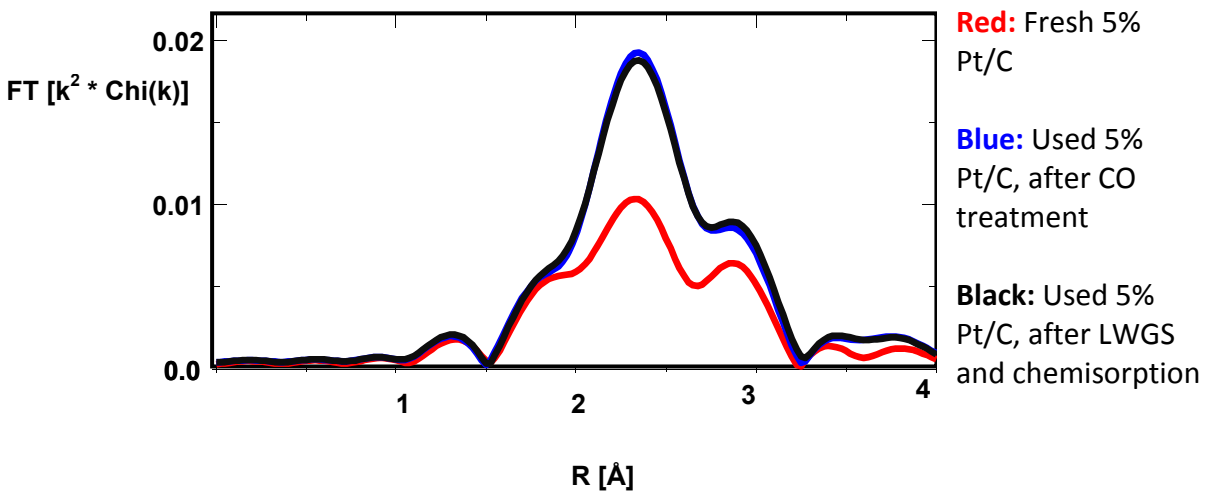

Figure 2.5 Fourier transform of the Pt L_{III} edge of 5% Pt/C reduced at 300°C

2.6 Conclusions

In this work, we have reported the TOF and full set of kinetics for the WGS reaction under liquid-phase reforming conditions for Pt and Pt-Mo catalysts supported on norit-carbon and multi-walled carbon nanotubes. It has been observed that for LWGS compared to gas-phase WGS, the apparent activation energy remains similar, the CO order increases, and the H_2 and CO_2 orders remain similar. These results can be attributed to the competitive adsorption with water, the lower temperature of operation, as well as the partial pressure range of each gas over which reaction orders were measured. The primary message from this comparison was that the kinetics significantly change due to presence of liquid water and this should be carefully accounted for when extrapolating WGS reaction rates from gas-phase to liquid-phase reforming conditions.

Additionally, the effect of the addition of Mo as a secondary metal to Pt catalysts was studied on both liquid-phase and gas-phase WGS. The ratio of TOF for Pt-Mo/MWCNT to Pt/MWCNT is similar for LWGS and gas-phase WGS. Also, the apparent activation energy is lower in case of Pt-Mo/MWCNT compared to Pt/MWCNT for both LWGS and gas-phase WGS. The reaction orders with respect to CO, H_2 and CO_2 for Pt/MWCNT and Pt-Mo/MWCNT are similar. This indicates that Mo alters the kinetics of each set of reaction conditions in a similar way.

2.7 Acknowledgements

Dr. Paul J. Dietrich and Dr. Jeffrey T. Miller carried out XAS experiments and data analysis. Dr. M. Cem Akatay performed transmission electron microscopy over the fresh and used catalysts.

CHAPTER 3. FAST HYDROPYROLYSIS OF CELLULOSE IN A NOVEL MILLISECOND RESIDENCE TIME CONTINUOU-FLOW REACTOR

3.1 Abstract

Design and operation of a lab-scale continuous-flow millisecond residence time hydropyrolysis reactor capable of operation up to 4.1 MPa has been successfully demonstrated. The entire process of fast hydropyrolysis including cooling the reaction product stream to ambient temperature was completed under 70 milliseconds. There is no consensus in the literature on the reaction pathway of cellulose pyrolysis. The goal in this work was to perform experiments at a millisecond timescale in order to not only identify but also quantify primary products of cellulose pyrolysis. The reactor design was based on a gaseous hydrogen-oxygen torch igniter that ensured extremely low residence time as well as dilute stream in excess of hydrogen which was envisioned to minimize secondary reactions. Liquid chromatography-mass spectrometry was used for identification and quantification of products accounting for >80% carbon in the bio-oil. The major compounds from cellulose hydropyrolysis at 535°C, 3.6 MPa hydrogen pressure and 70 milliseconds residence time, were levoglucosan and its isomers, cellobiosan, glycolaldehyde and glucopyranosyl-β-glycolaldehyde. As the temperature was increased up to 700°C, the yield to levoglucosan and cellobiosan decreased and was compensated by an increase in yield of C_2-C_5 light oxygenates, notably glycolaldehyde and formic acid.

3.2 Introduction

Transportation energy sector utilize petroleum based feedstocks due to the ease of use especially the very high energy density (34 MJ/L).[7] Hydrogen as well as electric powered batteries are plagued by relatively lower volumetric energy density which implies that new infrastructure would be required for their widespread use.[53] Fast pyrolysis of lignocellulosic biomass has been touted as one of the potential routes to produce liquid transportation fuel from a renewable source.[54] In this process, biomass is typically heated to moderate temperatures (~500°C) and quenched to collect a liquid product in about 2-10 s. The collected liquid, called bio-oil usually retains most of the oxygen from the parent biomass and is prone to degradation reactions unless upgraded.[55,56]

There is a debate in the literature on the primary products of pyrolysis of biomass. It has been reported in the literature that secondary reactions are responsible for the formation of light oxygenates.[11,30,57] Most papers in the area of biomass pyrolysis use reactor systems with residence time in the order of seconds which can lead to secondary and even tertiary degradation reactions.[55,58] Previously, Venkatakrishnan et al.[59] have shown that high-pressure hydrogen has little or no effect on cellulose pyrolysis. Our objective in this work was to minimize these secondary and tertiary reactions and collect the primary products of hydropyrolysis on a continuous-feed lab scale reactor while still providing valuable quantitative information. Our aim was to minimize secondary reaction both lowering the residence time and reducing the molecule-molecule collisions between the primary products of pyrolysis. This was achieved by diluting the stream in excess hydrogen. Additionally, Furfari and Cypres[60] have shown that for coal hydropyrolysis

increasing temperature of pyrolysis resulted in lower yield of desired products due to secondary reactions. We have also investigated the effect of temperature on biomass hydropyrolysis in the range of 500-700°C in terms of the product distribution and production of light oxygenates.

To accomplish these experimental goals, a modified version of a torch igniter operated in a sub-stoichiometric oxygen regime was used to generate hydrogen flow at temperatures of 500-700°C. This flow was used to heat the cellulose in a 10 ms residence time in the reactor section with a static mixer. Water cooled heat exchangers cooled down the reactor exit stream to ambient temperature within a total of 70 ms. This allowed us to complete the entire pyrolysis process in < 70 ms in a very dilute stream and thus minimize secondary reactions.

3.3 Experimental methods

3.3.1 Reactor design

The reactor design was based on a gaseous hydrogen-oxygen torch igniter developed to ignite various rocket combustors tested at Purdue University's High Pressure Laboratory in the Maurice J. Zucrow laboratories complex. The torch utilized additional hydrogen downstream to control the temperature of the combustion products as well as to cool internal components. All the experiments were conducted in hydrogen to oxygen molar ratio of 16 to 20 (indicating the extent of excess hydrogen flow) resulting in output temperatures of 750°C to 920°C. Cellulose entrained in hydrogen flow entered the reactor

in the axial direction which also caused a reduction of reactor temperature to the range of 520°C to 775°C.

The reactor system comprised of three sections: a) head-end, where the initial mixing of cellulose and hydrogen occurred along with rapid heat addition, b) main chamber which was fitted with a six element static mixer and c) sonic nozzle, which was used to step down pressure and split the flow evenly. Each of these reactor components were fabricated from SS 304, except for the torch igniter where Ni 200 was used to account for higher temperature. Figure 3.1 shows the schematic of the entire reactor, and Figure 3.2 depicts the internals and major components of the reactor with a labeled cross section view.

The hydrogen-oxygen torch flow enters the upper manifold via a SS 316 tube (igniter tube). Here the radial momentum of the flow is removed and the flow then travels axially to the lower manifold through eight rectangular passages. From the lower manifold, the flow enters the reactor radially through four injector orifices, 90° apart, one chamber diameter (2.54 cm) downstream from the cellulose-hydrogen injector as shown in Figure 3.2.

In order to ensure uniform heat and mass distribution the momentum of all the four injector orifices was matched to that of cellulose stream. Due to this requirement, the cellulose-hydrogen injector is removable and can be changed to allow running at different conditions. At the intersection of the four flows, the momentum of the resultant flow is

almost cancelled and the residence time is maximized to ensure uniform temperature. As the flow travels downstream, it enters a turbulence ring to increase velocity and turbulence. Upon exiting the turbulence ring and entering the chamber, the flow is subjected to a rearward facing step, where the sudden change in area results in the generation of vortices. All of these design features promote mixing and create uniformity in the resultant flow. The different head-end views shown in Figure 3.2 (a,b,c), illustrate these flow paths.

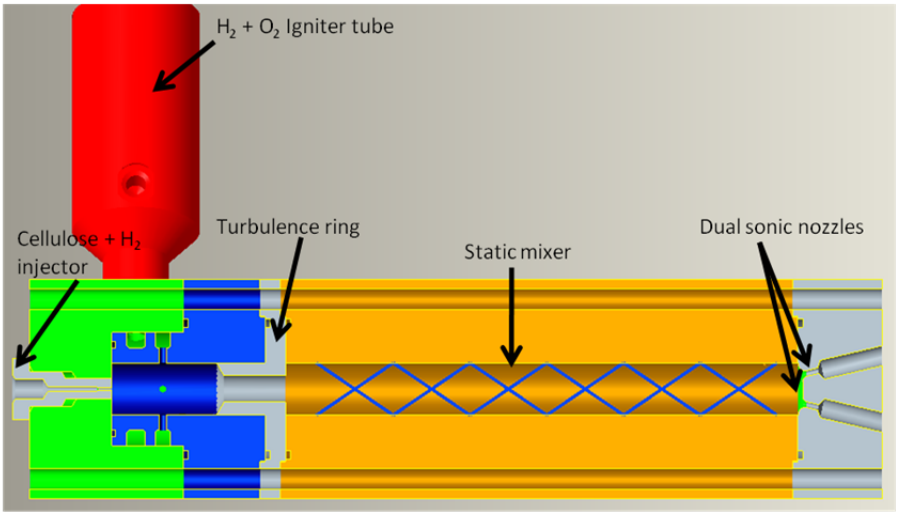

Figure 3.1 Schematic of the hydropyrolysis reactor to accomplish the process in a millisecond timescale

Initially two runs were conducted without the static mixer which resulted in >40% of feed cellulose remaining unpyrolyzed and stuck in the reactor section. Therefore, in next experiments a six element static mixture was installed to enhance mixing and reduce the portion of unpyrolyzed cellulose. Two identical sonic nozzles were placed downstream to

split the flow in to half. The total flow rate in the reactor was ~7000 slpm and to keep the heat exchanger size within the available space, half of the total flow was vented directly.

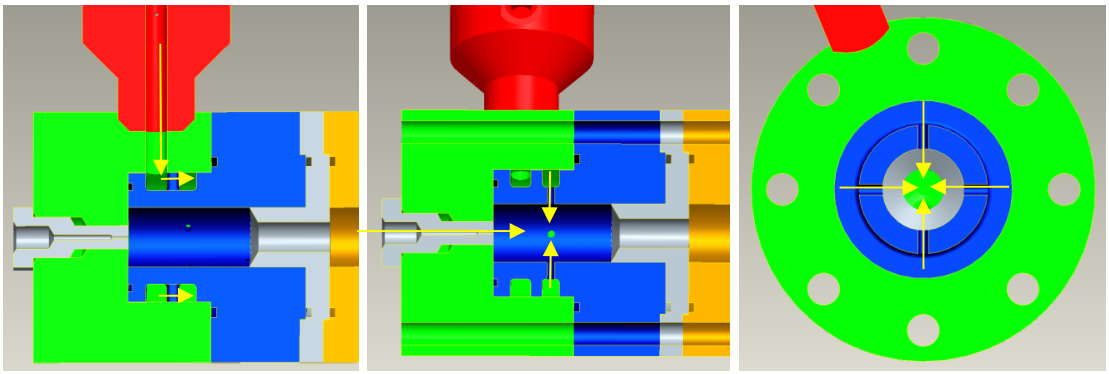

Figure 3.2 (a) Cross section view taken at the reactor injector depicting the hydrogen-rich torch igniter flow path (b) Cross section view of reactor injector, at a different radial location, showing injection orifices and head-end mixing region with flow path represented by arrows and (c) Cross section view taken at injector orifices and looking from the top down through the reactor

Quenching and cooling the reactor exhaust quickly is critical and is accomplished by using water-cooled, concentric tube, stainless-steel heat exchangers in series. The exhaust travels through one of the tubes and water, at a controlled mass flow rate, flows through the concentric annulus. The water flow rate can be varied to adapt the temperature of the exhaust exiting each exchanger if desired.

The exhaust travels through the first heat exchanger and any liquids coalesce in a polytetrafluoroethylene coalescing filter just downstream. The filter housing was modified so additional capture volume could be connected allowing more liquid to be collected. After the flow exits the first filter it passes through the second heat exchanger

and the remaining liquid is collected in another modified coalescing filter. At the exit of the second filter the flow is at room temperature and is vented to an exhaust stack. Backpressure is controlled with a sharp edge orifice downstream of the second filter.

Initially, it was hypothesized that the exhaust should be cooled to an intermediate level so the bio-oil would be liquid and the large amount of water produced in the hydrogen-oxygen reaction would be mostly steam. Consequently, bio-oil would have been the principal fraction collected in the first filter and would thus be easier to analyze due to the high concentration. The second filter collection vessel would contain mostly water and would be collected for use in the mass balance. This necessitated the use of two heat exchangers and two coalescing filters. In the end, it was found the analysis technique had no problem in analyzing the small concentrations of bio-oil in the large quantity of water, which allowed using the first heat exchanger to cool the exhaust to room temperature further reducing the quenching time.

3.3.2 Experimental procedure

Experiments were run for 3 minutes with the first 1.5 minutes allotted for pre-heating of the reactor only. As an example, the temperature profile in the reactor for run ID RR09 is shown in Figure 1. At 0s, flow of cellulose was initiated. After the run, a nitrogen purge was placed in the unit to clear out any hydrogen and to transfer any residual liquids from the heat exchangers to the collection filters. The reported temperature is equal to the average of the head-end and aft-end temperatures during the last 1.5 minutes of the experiment, i.e. the time of cellulose flow. Permanent gas production was quantified by an online FTIR (MKS 2030 Gas Analyzer). The cellulose feedstock used in all

experiments was 20 μm microcrystalline cellulose from Sigma Aldrich (St. Louis, MO). Ultra high purity (99.999%) grade hydrogen, high purity (99.99%) grade nitrogen were used for the experiments.

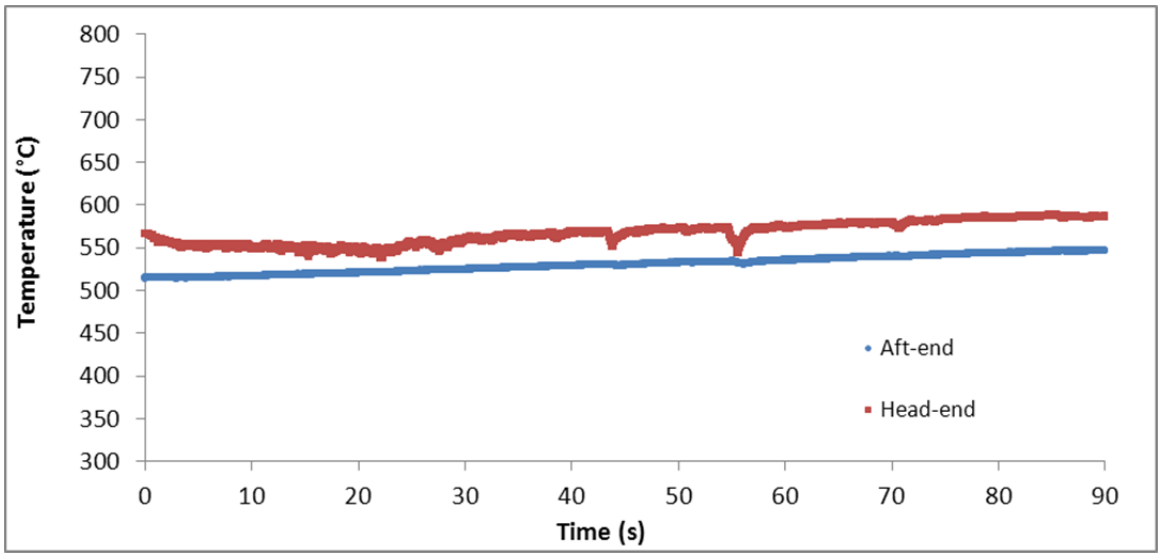

Figure 3.3 Temperature profile of the hydropyrolysis section plotted at both the head-end and aft-end during cellulose pyrolysis, for RR09.

3.3.3 Design of experiments

In previous studies, there is lack of understanding of the hydropyrolysis temperature range on the product distribution as well as the reaction pathway partly due to equipment constraints. Accurate control over hydropyrolysis temperature was obtained by tuning the molar hydrogen to oxygen ratio in the torch igniter. In this work, hydropyrolysis was performed over a range of 500-700°C and its effect is demonstrated over liquid product distribution.

Table 3.1 Hydropyrolysis temperature as a function of hydrogen to oxygen molar feed ratio in the torch igniter

Run ID	H_2/O_2 molar ratio	Average hydropyrolysis temperature/ °C
RR02	16.2	700
RR03	16.8	630
RR06	17.4	600
RR07	19.8	553
RR08	19.7	535
RR09	20.3	523

3.3.4 Bio-oil analysis

Bio-oil was analyzed by multiple techniques to get the overall carbon content, product quantification and molecular structure identification.

3.3.4.1 Total organic carbon (TOC)

Neat liquid products were analyzed for total carbon by the Total Organic Carbon (TOC) analysis (EPA 415.1) carried out by Galbraith Labs (Knoxville, TN). TOC was chosen, since the bio-oil collected consisted mostly of water formed by hydrogen combustion prior to the reactor and the organic carbon concentration was of the order of 5000-10000 ppm.

3.3.4.2 Liquid chromatography – mass spectrometry (LC-MS)

LC-MS setup and methodology used in this work is described in detail in a previous paper.[59] Briefly, an Agilent 1200 LC equipped with Rezex ROA column supplied by Phenomenex (Torrance, CA) and Refractive index detector (RID) was used for product quantification. Additionally, chromatographic separation was followed by Agilent single quadrupole MS G6130A with an atmospheric pressure chemical ionization source. This MS technique has been shown to be optimized to detect sugar molecules without fragmentation.[61,62] The mobile phase used was 0.1% formic acid in water at a total flow rate of 0.5 ml min^{-1} and the column temperature was held constant at 80°C. With this LC-MS technique we are able to identify and quantify the top 10 most abundant compounds present in the bio-oils produced from this reactor system accounting for 80-90% of carbon in liquid.

Both retention time, based on pure compound injections, and their mass spectra were used for identification. For quantification of most of these compounds, the RID was calibrated in the observed range using commercially purchased pure chemicals. All liquid samples were prepared were first diluted in mobile phase in a 1:1 gravimetric ratio and 10 µl of the resulting sample was injected using an autosampler. Each of the bio-oil samples was analyzed with repeats to give us an error in measurement of the analytical technique. Below is a representative RID spectrum from RR09 and RR06 that has been presented with the labeled peaks.

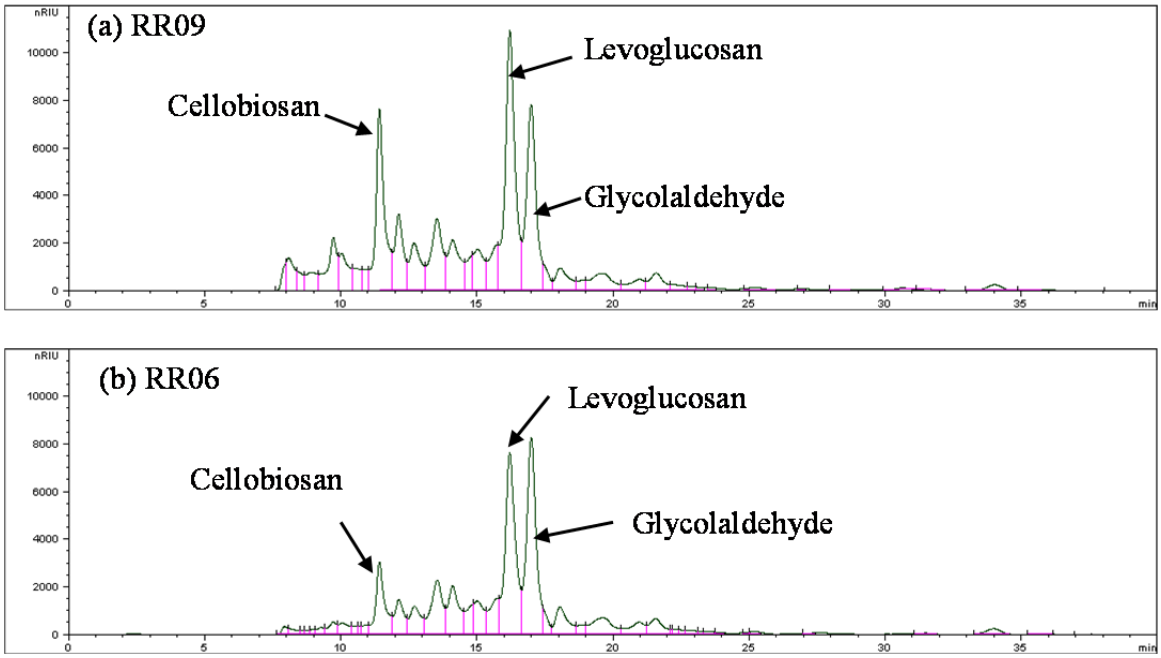

Figure 3.4 RID spectrum of a bio-oil sample from cellulose hydropyrolysis carried out at (a) RR09, 553°C and (b) RR06, 600°C

3.3.4.3 Linear quadrupole ion trap mass spectrometry (LQIT-MS)

Vinueza et al.,[61] have reported the utility of using chlorine ion attachment in atmospheric pressure chemical ionization for molecular weight determination and structure interpretation for a variety of sugars. This method has been shown to identify xylose, levoglucosan, glucose, cellobiose and other higher mass sugars with almost equal ionization efficiency. Recently, similar methodology was applied to ionize cellobiosan using chloride attachment by Hurt et al.[62] This method has also been successfully integrated with a commercially available pyrolysis reactor to identify primary pyrolysis products of cellulose and other anhydro-sugars.

3.4 Results

3.4.1 Overall and carbon mass balance

Here, we report the overall and carbon mass balance of three hydropyrolysis experiments. The amount of cellulose fed was calculated by weighing the feed hopper before and after the experiment. After the experiment, wet filter elements were dried in air at room temperature for 24 h and weighed to determine the amount of unconverted cellulose embedded in the filters. With this procedure, the unreacted solids fraction is over estimated because much of the organic product dissolved in the bio-oil is composed of non-volatile carbohydrate derivatives which will remain in the filter upon drying.

Bio-oil collected in the trap was sent to Galbraith Labs for TOC analysis for estimating the amount of carbon present. The extent of carbon present in permanent gas is measured using a FTIR (MKS 2030) analyzer downstream of coalescing filter. We were only able to detect CO, CO_2.

Table 3.2 Overall and Carbon mass balance

Experiment ID	RR07	RR08	RR09	Average
Average Reactor Temperature / °C	523	535	553	537 ± 15
Overall mass balance / %	71	80	67	72.7 ± 7
Carbon Mass Balance (50% of total flow)				
Feed / g	9.1	9.1	9.9	
C as solids / g	0.9	0.9	1.4	
C as liquids / g	4.7	5.3	5	
C as gases / g	0.2	0.6	0.7	
Total C accounted for / g	5.8	6.8	7.1	
Carbon balance / %	63.7	74.7	71.7	70.1 ± 6
Carbon / overall balance / %	89.8	93.4	107	96.7 ± 9
Distribution of Carbon in Products				
Solids / %	15.5	13.2	19.7	16.2 ± 3
Liquids / %	81	77.9	70.4	76.5 ± 5
Gases / %	3.4	8.8	9.9	7.4 ± 3

Carbon balance for all the three runs was relatively low at about 70%. This could be attributed to two factors. As discussed previously, the reactor effluent was split in two streams, one of which was vented, and the other goes through heat exchangers and coalescing filters. This was accomplished by means of two identical orifices, which were designed to provide a 50/50 split; however, since the split was dependent on the pressure drop in the downstream sections, the split deviates slightly from 50/50. We can take the

overall mass balance as a measure of how imperfect the split was; hence dividing the carbon balance by the overall mass balance gives an accurate measure of how much carbon we can account for. This number was comparatively higher at close to 96%. Another reason could be the underestimation of carbon in solids. We assumed that collected solid was unreacted cellulose thus contains only ~50% carbon, however, it was light brown in color indicating it was partially pyrolyzed and potentially could have a higher contribution of carbon.

3.4.2 Product distribution from LC-MS

As reported in Table 1, liquids account for 76% of carbon in the product comparable with other published reports.[55,57,59] Naturally, it would be interesting to identify the major products in liquid to interpret the effect of pyrolysis parameters. Traditionally, gas chromatograph coupled with mass spectrometer (GC-MS) has been used to identify compounds present in bio-oil. However, GC-MS is unable to account for cellobiosan or higher molecular weight saccharides and is susceptible to degradation reactions of heavier sugar molecules. Therefore, LC-MS was chosen as a preferred analysis technique to both identify and quantify compounds present in the bio-oil. A compiled list of top 10 most abundant compounds present in each bio-oil is presented in Table 2 accounting for > 80% carbon present in the bio-oil.

Table 3.3 % Carbon distribution for bio-oils estimated by LC-MS (normalized by TOC analysis)

Run ID	RR07	RR08	RR09	RR06	RR03	RR02
Temperature/ °C	523	535	553	600	630	700
Cellobiosan/ % Carbon	9.9	10.9	10.6	6.2	7.0	5.2
Glucopyranosyl-β-glycolaldehyde/ % Carbon	6.9	5.3	5.7	11.9	13.4	7.9
Levoglucosan and isomers/ % Carbon	42.5	48.2	40.4	43.8	34.4	29.6
Glycolaldehyde/ % Carbon	11.8	12.4	13.4	19.5	21.5	23.7
Formic Acid/ % Carbon	2.7	3.4	3.5	5.3	7.2	9.5
Acetic Acid/ % Carbon	4.0	4.5	0.0	0.0	0.0	2.0
1,6,2,3 dianhydromannopyranose/ % Carbon	1.7	2.1	2.7	4.0	4.1	4.2
Hydroxyacetone/ % Carbon	2.5	2.7	2.8	3.4	3.4	3.8
Ethanol/ % Carbon	0.0	0.0	0.0	0.3	0.6	0.9
5-hydroxymethyl furfural/ % Carbon	0.9	0.8	0.7	0.9	0.4	0.4
Furfural/ % Carbon	0.0	0.1	0.1	0.0	0.2	0.3
Total % Carbon accounted	82.8	90.4	79.9	95.2	92.3	87.5

For every test temperature in the range of 523-700°C, levoglucosan was the major product. Glycolaldehyde and cellobiosan were the next most abundant products in the bio-oil. Although, the identities of the top 4 or 5 compounds in all the bio-oil samples remain the same, their relative amounts change significantly depending on the temperature.

3.4.3 Comparison with literature reports

Below given is the comparison of product distribution from pyrolysis of cellulose at ~500°C at significantly different residence times. Although hydrogen pressure of operation is also different across the comparison, Venkatakrishnan et al. have reported that hydrogen pressure up to 2.5 MPa does not alter product distribution from cellulose pyrolysis.[59] The major dissimilarity is in the yield of heavier molecules, namely cellobiosan and glucopyranosyl-β-glycolaldehyde. The analytical technique used for both continuous feed systems: millisecond timescale reactor and cyclone reactor was LC-MS whereas micropyrolyzer used direct injection into GC-MS. However, cellobiosan has been shown before to undergo degradation reactions to levoglucosan or condense in the capillary column of the GC.[63–65]

Table 3.4: % Carbon distribution in top five compounds from cellulose pyrolysis at ~500°C across reactor configurations with 70-2000 ms residence time

	Millisecond timescale reactor	Cyclone reactor	Micropyrolyzer (followed by GC/MS)
Residence time/ ms	70	2000	15-20 (excluding time in GC/MS)
Temperature/ °C	523	520	500
Cellobiosan/ % carbon	9.9	1.5	-
Glucopyranosyl-β-glycolaldehyde/ % carbon	6.9	-	-
Levoglucosan/ % carbon	42.5	52	62.8
Glycolaldehyde/ % carbon	11.8	7.5	6.7
Formic acid/% carbon	2.7	10	6.6

3.4.4 Product distribution from LQIT-MS

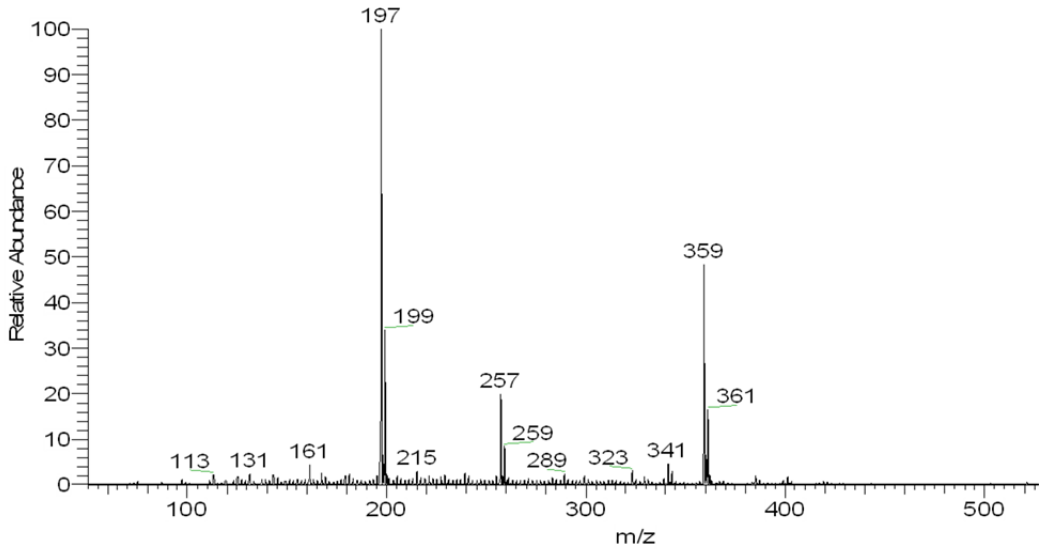

Figure 3.5 LQIT-MS spectra for RR09

In the spectra only three major peaks are observed, corresponding to m/z of 197, 257 and 359 (Figure 3.5). Since, these ions are chloride attached, the molecular weight of these compounds are 162, 222 and 324 whose molecular identities are discussed below. As already discussed before, this method has been optimized for identifying sugar derived molecules. An interesting feature of this setup is the capability to perform tandem mass spectrometry experiments where a single ion can be isolated and bombarded with He. The resulting fragments carry information regarding the molecular structure of the parent molecule and is a useful technique to elucidate the molecular structure of some of the compounds.

3.5 Discussion

3.5.1 Product distribution at hydropyrolysis temperature of 535°C

In the bar graph shown below, the relative proportion of the top four compounds present in bio-oil are presented (Figure 3.6). Nearly, 90% of carbon estimated from the total organic carbon (TOC) analysis was accounted for all the identified compounds using the LC-MS. Thus, LC-MS is able to give us an accurate representation of the product distribution in the bio-oil. It is important to note that nearly 70% of carbon in bio-oil was accounted for by only three compounds – levoglucosan, cellobiosan and glycolaldehyde. This suggests a relatively simple product distribution. Another interesting result is a significantly higher abundance of cellobiosan compared to previous reports from lab-scale pyrolysis and hydropyrolysis reactors.[59] In literature, anhydro-oligosaccharides (such as cellobiosan) are reported to be either primary products of pyrolysis[66–68] or are claimed to be present as a result of polymerization of anhydrosugars.[11,57] Degenstein et al., report the possibility of small anhydrooligosaccharides (such as cellobiosan) being the primary product of cellulose pyrolysis which can subsequently react to form levoglucosan and other light oxygenates. Given that the product stream was relatively dilute and the overall residence time in the reactor was on the order of milliseconds, the extent of secondary reactions are greatly minimized. For that reason, we assigned cellobiosan and other oligomeric sugars such as cellotriosan present in bio-oil as primary pyrolysis products.

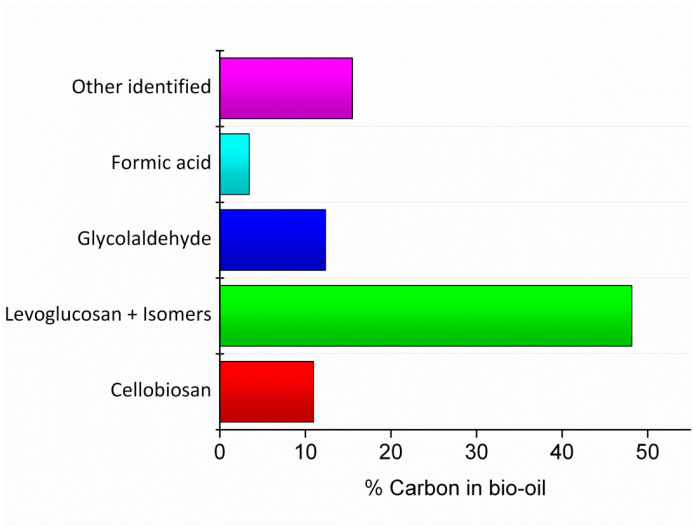

Figure 3.6 Product distribution for hydropyrolysis temperature 535°C

However, each of these top three compounds retain nearly the same oxygen content as the parent cellulose. Consequently, it can be established that hydropyrolysis as a standalone process breaks down the polymer structure of cellulose into smaller units, but there is no deoxygenation without a catalyst. This result is comparable to that reported in literature for cellulose pyrolysis in a variety of reactors.[57,59]

3.5.2 Trends with temperature

3.5.2.1 Levoglucosan and cellobiosan

One of the parameters that was tunable in our reactor setup was the oxygen to hydrogen ratio in the igniter allowing us to accurately control pyrolysis temperature. Some studies have previously reported the effect of temperature on coal hydropyrolysis as well as biomass pyrolysis; however, most focus only on the overall liquid and gas yields. It would be interesting to study how product composition is affected in the bio-oil as a

consequence of temperature variation over a reasonably significant change. As we increase the pyrolysis temperature from 535 to 700°C, we observe that there is a decrease in yield of levoglucosan from nearly 50% to 30% (Figure 3.7). A similar decrease was also observed in the yield of cellobiosan. At the higher temperatures, it is possible that enough thermal energy is provided to promote secondary reactions which lead to production of light oxygenates via either anhydrosugar degradation or new pathways for cellulose chain scission.

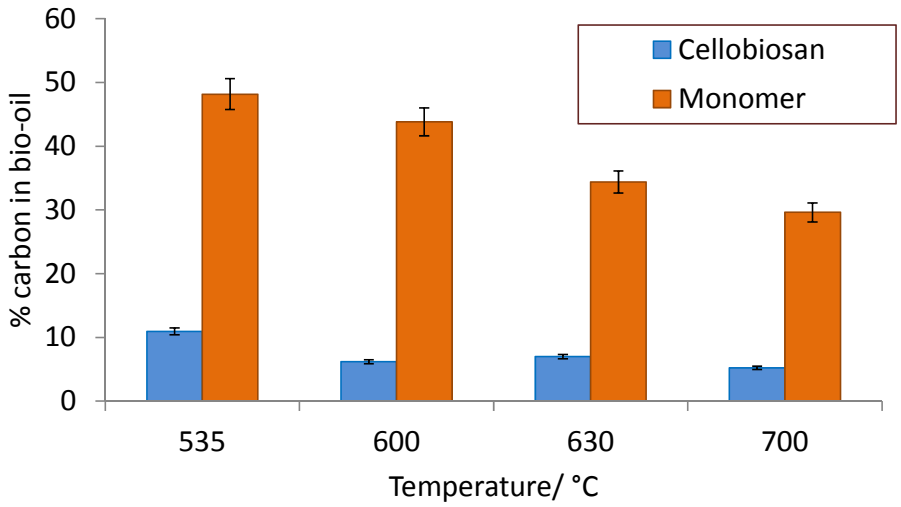

Figure 3.7 Dependence of levoglucosan and cellobiosan production on temperature

3.5.2.2 C_2-C_5 oxygenates

When we followed the yields of light oxygenate hydrocarbons (C_2-C_5), we observe that unlike levoglucosan their yields increased with increasing temperature (Figure 3.8) in agreement with other reported results.[59,69] Glycolaldehyde was the most abundant light

oxygenate accounting for as high as 25% of carbon in the bio-oil at 700°C. Notable increases were also observed in the yield of formic acid as the hydropyrolysis temperature was increased. At high temperatures, cellulose may undergo *in-situ* production of reducing end functionality which can then fragment to light oxygenates after ring opening. It can also be argued that primary products from cellulose are still anhydrosugars which may then undergo further ring opening reactions either from the terminal anhydro unit or other glucopyranosyl units to give glycolaldehyde and formic acid.

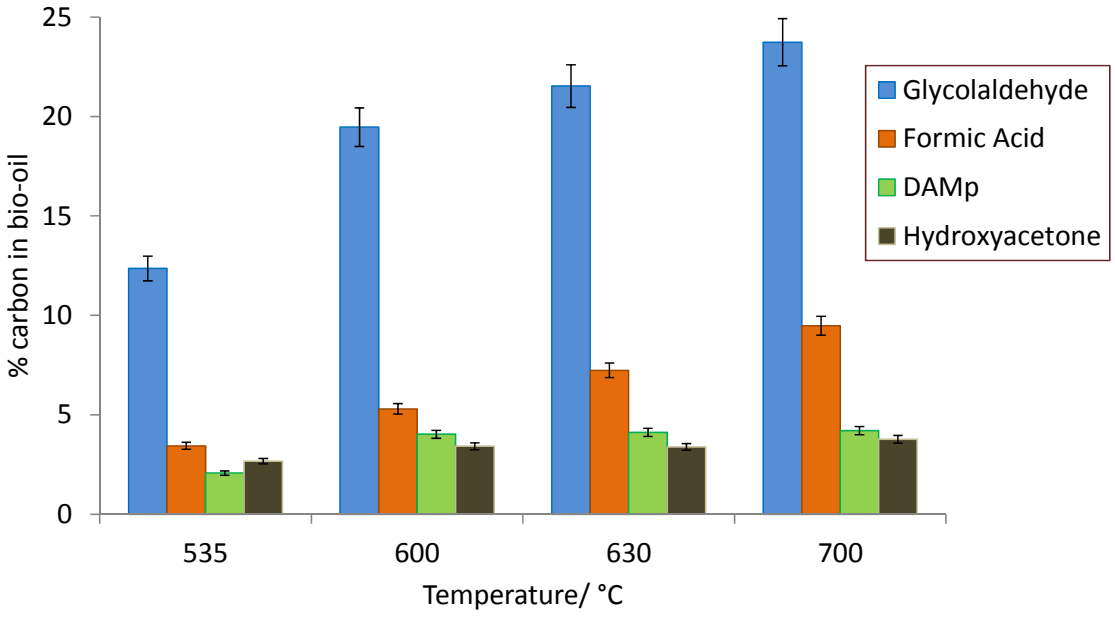

Figure 3.8 Dependence of C_2-C_5 oxygenate production on temperature
DAMP: 1,6,2,3 dianhydromannopyranose

3.5.3 Comparison of analytical techniques (LC-MS vs. LQIT-MS)

One of the advantages of using LC-MS is that it is quantitative, and can be used to estimate relative amounts of various products present in the bio-oil. Unlike LC-MS, LQIT-MS does not provide absolute quantitation, but it is a useful tool to identify molecular structure of ionizable molecules. Even with a relatively simple structure that of cellulose, the product distribution can be quite complex, in such a scenario MS^n experiments on LQIT-MS can help elucidate the structure. In the case of bio-oil from Run ID RR09, we find that LQIT-MS shows three significant peaks at molecular weights 197, 257, 359 which are all chloride adducts (Figure 3.5). The products with molecular weight 162 and 324 can be assigned to levoglucosan and cellobiosan respectively. The compound corresponding to molecular weight 222 was identified as glucosylpyrano-β-glycolaldehyde from the LQIT-MS setup in absence of commercially available pure compound.[62] Comparing this result with LC-MS we find that, these three are among the top 4 compounds present in the bio-oil on the basis of % carbon. One of the compounds that is present in significant amounts and does not ionize appreciably using the current LQIT-MS method is glycolaldehyde.

3.6 Conclusions

In this study a novel millisecond residence time high-pressure continuous-flow fast-hydropyrolysis reactor was designed and tested. Cellulose was used as a model feedstock to identify and quantify primary products of hydropyrolysis and their sensitivity to the hydropyrolysis temperature. The product distribution at 535°C revealed that 70% of carbon was accounted for by glycolaldehyde, cellobiosan, levoglucosan and its isomers.

This product distribution can be controlled by tuning the hydropyrolysis temperature. As the temperature of hydropyrolysis was increased the yield of anhydrosugars decreased and it was compensated by increase in the yield of light oxygenates notably, glycolaldehyde. Furthermore, reactor residence time has been shown to have a significant influence on the product distribution from cellulose hydropyrolysis, especially in the production of cellobiosan. However, these compounds still retain the same oxygen content as cellulose and the challenge going forward would be to find a suitable catalyst that would be able to deoxygenate selectively without cleaving the C-C bonds.

3.7 Acknowledgements

Design and operation of the reactor system was performed in collaboration with Dr. Nick Nugent and Dr. Andrew Smeltz under the guidance of Prof. William Anderson. Experiments were conducted in ZL-4 (Zucrow Laboratories No. 4) in Purdue University under the supervision of Dr. Scott Meyer. LC-MS analytical technique was developed by John Degenstein and Vinod Kumar Venkatakrishnan. LQIT-MS analysis on the bio-oil samples were carried out by Dr. Matt Hurt in Prof. Hilkka Kenttämaa's lab.

CHAPTER 4. HYDRODEOXYGENATION KINETICS OF FURFURAL OVER PLATINUM-BASED CATALYSTS

4.1 Abstract

Previously, hydrogen pressure (up to 3.6 MPa) in standalone pyrolysis was shown to have little or no effect on deoxygenation of cellulose. Catalytic hydrodeoxygenation therefore holds the key to production of fungible hydrocarbon fuels from biomass. Furfural was chosen as a model compound representing furan-ring based compounds typically produced from cellulose and hemicellulose constituents of biomass. Under the reaction conditions and over Pt-based catalysts, furfural underwent four major primary transformations in presence of hydrogen: a) decarbonylation to furan, b) reduction to furfuryl alcohol, c) furan ring-opening reaction and d) furan-ring hydrogenation. In this work, kinetics of furfural hydrodeoxygenation including apparent activation energy are presented over monometallic Pt catalysts. Furthermore, influence of hydrogen pressure and oxophilic promoter (Mo) over the dominant pathway, especially the selectivity of C-O bond scission is presented. In order to gain an in-depth understanding of the role of Pt and Mo in the reaction network, a series of catalysts with varying Pt to Mo (1 to 5) proportions were tested.

4.2 Introduction

Cellulose and hemicellulose account for 60-70% by weight and up to 55% of carbon of intact biomass.[70] Furan-ring based compounds are one of the major classes of products from cellulose and hemicellulose processing.[71] Many methods have been proposed to breakdown cellulose and hemicellulose to produce a variety of platform chemicals that can be further utilized to supplant petroleum-based fuels and chemicals.[10,72] Hydropyrolysis of cellulose and intact biomass results in a complex product distribution of oxygenated derivatives.[54,55] Typical oxygen functional groups include carboxylic acids, aldehydes, alcohols, ethers et cetera.[20,73] Thus, understanding the kinetics of hydrodeoxygenation reactions using representative model compounds is essential.[74] Furfural was chosen as a model compound of choice, since it included two distinct oxygen functional groups (aldehyde and ether), and an aromatic ring that can be used to compare hydrodeoxygenation kinetics. In literature, hydrodeoxygenation of biomass model compounds have been covered in detail in reviews by Furimsky, Elliot, Resasco.[20,75,76]

Resasco and co-workers have reported Pd, Cu, Ni based catalysts for furfural hydrodeoxygenation.[77–79] Cu-based catalyst have a lower overall rate of reaction but selectively reduce the aldehyde to furfuryl alcohol compared to Pd or Ni catalyst. Xiong et al. and Lee et al. have reported molybdenum carbide catalytic system to exhibit selective deoxygenation to produce 2-methylfuran.[80–82] However, molybdenum carbide catalysts are prone to continuous deactivation possibly due to buildup of oxygen species. Pushkarev et al. have shown that the Pt nanoparticle size affects the selectivity of vapor-

phase furfural hydrodeoxygenation pathway.[83] Furfural has also been shown to undergo esterification with acetic acid over Pd catalysts to increase the carbon number of the liquid product which opens up a possibility of using lighter C_2 by-products that are obtained through various thermochemical methods.[84] Furthermore, Prasomri et al. report Mo-oxide based catalyst to have selective deoxygenation toward many bio-derived oxygenates.[85,86] Most of these studies were carried out at ambient pressure of hydrogen and there is a need to explore the effect of hydrogen pressure on pathway selectivity. Mo has also been reported previously for enhancing C-O bond scission.[87] A bimetallic Pt-Mo catalyst system has been tested in this work, with Pt providing the hydrogenation function and Mo is responsible for selective C-O bond scission.

4.3 Experimental methods

4.3.1 Catalyst synthesis

The catalysts used in this study were monometallic platinum and a series of bimetallic platinum-molybdenum supported on multi-walled carbon nanotubes (MWCNT, sourced from Cheaptubes Inc.). The Pt-Mo bimetallic catalysts were prepared by sequential incipient wetness impregnation (IWI) of aqueous solution of tetraammineplatinum (II) nitrate ($Pt(NH_3)_4(NO_3)_2$, Sigma Aldrich) to obtain required wt. loading of Pt followed by aqueous solution of ammonium heptamolybdate ($(NH_4)_6Mo_7O_{24}.4H_2O$), Sigma Aldrich) to obtain a desired loading of Mo. The catalyst was dried in air for 12 hours at 60°C after the Pt loading and then at 150°C for 12 hours in air after the Mo loading. Bimetallic catalysts were prepared with Pt-Mo weight loadings of 5%-1.25%, 5%-2.5%, 2.5%-2.5% and 2%-4.9% corresponding to atom ratios of 1:0.5, 1:1, 1:2 and 1:5. The monometallic

Pt catalyst was prepared by IWI of aqueous solution of tetraammineplatinum (II) nitrate ($Pt(NH_3)_4(NO_3)_2$, Sigma Aldrich) to achieve 5 wt% loading followed by drying in air at 150°C for 12 hours.

4.3.2 Catalyst characterization

4.3.2.1 Oxygen and carbon monoxide chemisorption

Oxygen and carbon monoxide uptake was measured for each of the catalysts in a Micromeritics ASAP 2020 instrument. About 120 mg of as-prepared catalyst was loaded in between two plugs of quartz wool in a flow-through tube. The catalyst was then degassed at a temperature of 250°C until the increase in pressure rate was <10 μmHg/min. The next step was *in-situ* catalyst reduction under hydrogen flow through a 2 hour ramp to 450°C and a subsequent hold for another 2 hours. This procedure was identical to the one used in reactor for kinetic measurement. Following reduction, catalyst was evacuated at 450°C for 2 hours and subjected to a leak test at 35°C to check for the outgas rate. The analysis was carried out with oxygen in a pressure range of 100-400 mmHg at 35°C. Following oxygen chemisorption, the sample was reduced and evacuated at 250°C for 2 hours followed by analysis with CO in a pressure range of 200-400 mmHg at 35°C.

4.3.2.2 Transmission electron microscopy (TEM)/ Scanning transmission electron microscopy (STEM)

High resolution transmission electron microscopy was used for particle size distribution analysis for all catalysts tested in the study, described in detail elsewhere.[42] Catalyst

samples were dispersed in pure ethanol (1-2 mg of catalyst in 1-3 ml ethanol) and an ultrasonic bath was used to stir the suspension for ~5 min. An FEI Titan 80-300 operating at 300kV was used to collect the TEM images, and an aberration corrected Hitachi HD-2700C microscope was used to conduct STEM and electron energy loss spectroscopic analysis.[88]

4.3.2.3 X-ray absorption spectroscopy (XAS)

XAS experiments were conducted in transmission mode at the Sector 10 materials research collaborative access team insertion device (10-ID) and bending magnet (10-BM) beamlines at Advanced photon source, Argonne national laboratory. *Ex-situ* experiments were conducted over catalysts reduced at 450°C for at least 30 min under a total flow rate of 50 sccm (25% H_2/ 75%He). The catalyst samples were then cooled down to room temperature and then scanned in the He atmosphere. Experiments and data analysis was carried out using the procedure described previously in Dietrich et al.[87]

4.3.2.4 X-ray photoelectron spectroscopy (XPS)

A Kratos Axis Ultra DLD with monochromatic Al Kα radiation (hν = 1486.6 eV) was used to perform X-ray photoelectron spectroscopy (XPS). As prepared catalysts were loaded into a sample holder and were reduced under 35 sccm hydrogen and 50 sccm argon at 450°C for 2 hours. These samples were transferred in to the XPS chamber via a transfer arm without air exposure.

4.3.2.5 Temperature programmed reduction

TPR experiments were performed in a Micromeritics Autochem II 2920 chemisorption analyzer equipped with a thermal conductivity detector (TCD) and an Agilent 5975C mass spectrometer.[89] As prepared catalyst was loaded directly in a U-shaped quartz cell between two plugs of quartz wool for TPR measurements in the Autochem II unit. The sample was first treated with UHP helium at a flow rate of 50 sccm for 30 min at ambient temperature. The temperature was ramped from 25 to 500°C with a rate of 10 °C/min in a total flow rate of 100 sccm hydrogen flow.

4.3.3 Flow reactor to measure kinetics

Kinetic measurements were made in a vapor-phase fixed bed reactor capable of operation of up to 3.4 MPa. Furfural (Sigma Aldrich, 99%) was fed as a liquid through an HPLC (Lab Alliance Series III) pump capable of operation in the range of 0.05-5 ml/min. Hydrogen (0-5 slpm, 99.995% Praxair) and nitrogen (0-500 sccm, 99.99% Indiana Oxygen) were used as carrier gases. Furfural was vaporized at the top of reactor before mixing with the carrier gas. The mixture then was passed over a fixed bed of catalyst whose temperature was controlled by an applied test systems furnace. The post-reactor lines were kept at 200°C via heating tape. The reaction mixture was then passed over an ice-bath condenser fitted with a trap to collect the liquids. The permanent gas then was scrubbed in a coalescing filter to remove any aerosols/ vapor. Back pressure regulator (GO regulators) was used to control the pressure in the reactor system. Two condensers were used in parallel to ensure continuous reactor operation while liquid samples were collected every 2 hours (~20 ml).

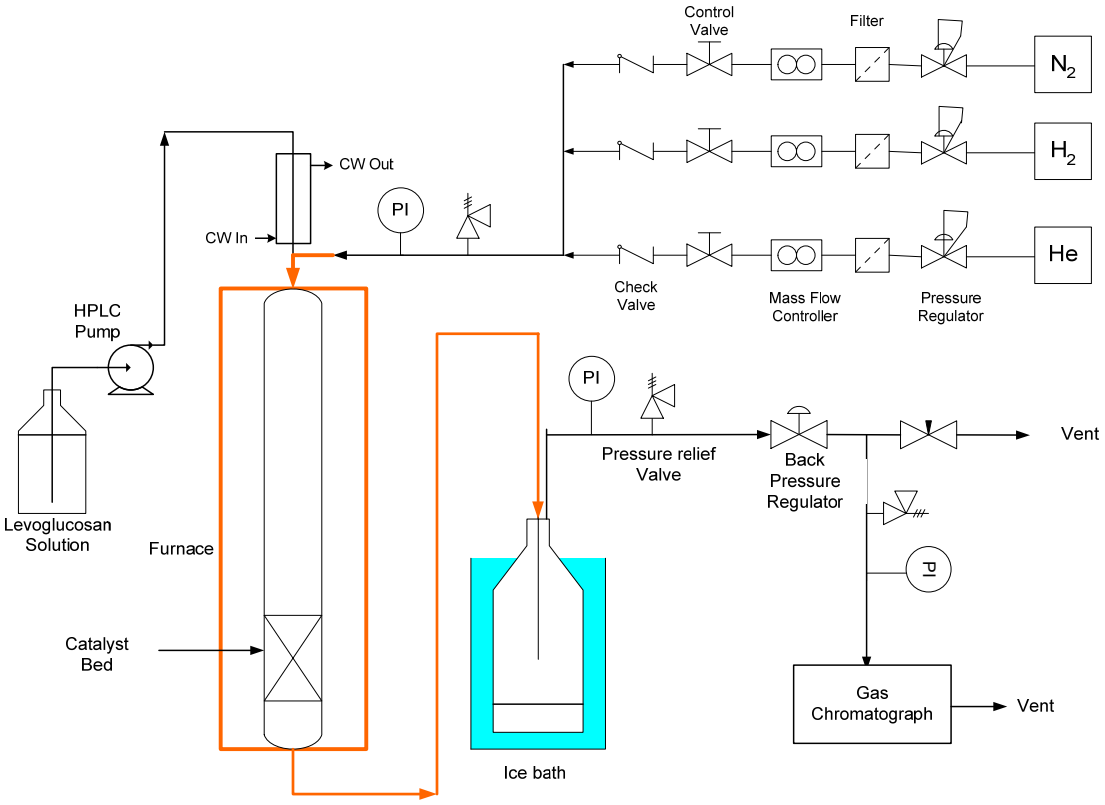

Figure 4.1 Reactor schematic for vapor-phase hydrodeoxygenation of furfural capable of operation up to 5 MPa with online analysis of permanent gas

The permanent gases were analyzed online in an Agilent 7890A gas chromatograph (GC) fitted with a Carboxen 1000 column followed by thermal conductivity detector (TCD) using helium as a carrier gas. The condensate liquid was analyzed off-line in an Agilent 7890A gas chromatograph equipped with a 5975C mass spectrometer and an Autosampler 7693. A split/splitless injector was connected to a DB1701 capillary column followed by a 3-way splitter to a flame ionization detector (FID) and mass spectrometer (MS) for quantification and identification of compounds.

Furfural conversion was estimated by $X = \frac{\text{moles of furfural reacted}}{\text{moles of furfural fed}} \cdot 100\%$ and carbon product selectivity was defined as $S_c = \frac{\text{carbon moles of product}}{\text{moles of furfural} \cdot 5} \cdot 100\%$. Overall STYs were estimated as $STY_{Pt} = \frac{X \cdot \text{moles of furfural fed}}{\text{moles of Pt} \cdot s}$, product STYs as $STY_{Pt} = \frac{X \cdot S_c \cdot \text{moles of furfural fed}}{\text{moles of Pt} \cdot s}$.

4.4 Results

4.4.1 Catalyst characterization

4.4.1.1 CO chemisorption

Carbon monoxide and oxygen uptake was measured on a series of as-prepared Pt-Mo catalysts after *in-situ* reduction and degassing. Corresponding isotherms are presented in the Appendix C. The CO uptake on the series of catalysts progressively decreased as relative Mo loading increased, and an opposite trend was observed for the oxygen uptake.

Table 4.1 CO and O_2 uptake for the series of as prepared Pt-Mo bimetallic catalysts

Catalyst	CO uptake/ μmol g^{-1}	O_2 uptake/ μmol g^{-1}
5%Pt	55	41
5%Pt-1.25%Mo	49	37
5%Pt-2.5%Mo	21	76
2.5%Pt-2.5%Mo	8	-
2%Pt-4.9%Mo	0	98

4.4.1.2 Transmission electron microscopy/ Scanning transmission electron microscopy

Particle size analysis performed on fresh 5%Pt and 5%Pt-2.5%Mo catalyst revealed the average nanoparticle size to be 2.2 ± 0.7 nm and 2.4 ± 1.4 nm. STEM measurements coupled with EELS were utilized to track the morphology and metal distribution of nanoparticles. Typical STEM-EELS micrographs of 5%Pt-2.5%Mo representing Pt-only particles, Pt-Mo coordinate particles and Pt-Mo alloy particles are presented below:

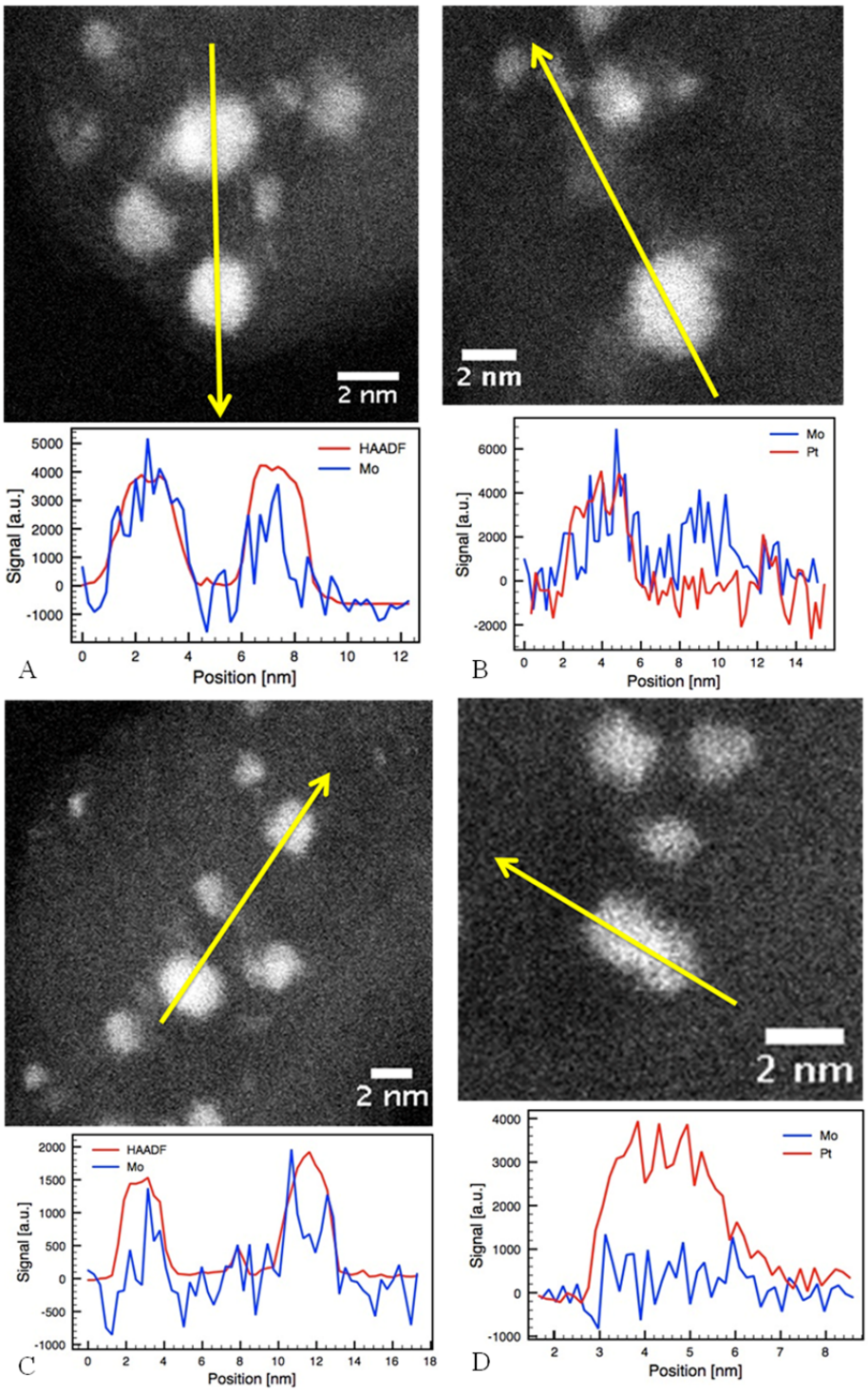

Figure 4.2 HAADF STEM micrographs and STEM-EELS elemental line-scans showing Pt (red) and Mo (blue) signals of representative particles on the 5%Pt-2.5%Mo/MWCNT catalyst. A) Pt-Mo alloy (Left) and PtMo alloy particle at support edge showing Mo patch underneath the PtMo alloy particle (Right), B) PtMo alloy particle (Left) and Mo patch (Right), C) PtMo coordinated particles, and D) Pt only particle.[31]

4.4.1.3 X-ray absorption spectroscopy

X-ray absorption near edge spectroscopy (XANES) at the Pt edge compared to a 5%Pt/MWCNT foil revealed a shift to a higher energy for 5%Pt-2.5%Mo/MWCNT catalyst for a similar nanoparticle size. Moreover, there was also an increase in white line intensity which indicated alloying between Pt and Mo. The Mo edge XANES pointed out that 5%Pt-2.5%Mo/MWCNT catalyst had an intermediate degree of reduction after undergoing reduction at 450°C in hydrogen.

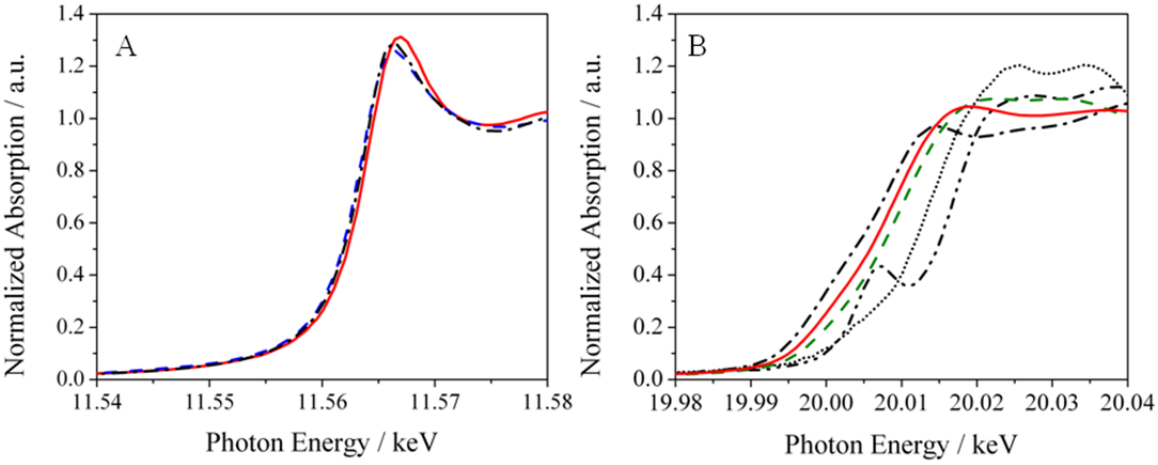

Figure 4.3 XANES spectra for fresh catalysts reduced at 450°C and scanned in He at RT: A) Pt LIII edge (11.54 – 11.58 keV) for Pt foil (dashed/dotted black), 5%Pt/MWCNT (dashed blue), and 5%Pt-2.5%Mo/MWCNT (solid red); B) Mo K edge (19.98 – 20.04 keV) for Mo foil (dashed/ dotted black), MoO_2 (dotted black), MoO_3 (dashed/dot/dot black), 2.46%Mo/MWCNT (dashed green) and 5%Pt-2.5%Mo/MWCNT (solid red).[31]

Extended X-ray absorption fine structure (EXAFS) experiments were conducted at the Pt L_{III} and Mo K edge. The 5%Pt-2.5%Mo catalyst had a Pt-Pt coordination number of 8.6 and a Pt-Mo coordination of 3.1. Over the Mo edge the fit parameters showed a Mo-Mo

coordination of 1.1 and a Mo-Pt coordination of 1. These results are consistent with a Pt-rich core and a Mo shell structure.

4.4.1.4 X-ray photoelectron spectroscopy

XPS measurements were carried out on as-prepared Pt-Mo catalysts reduced *in-situ* to obtain overall quantification of Pt: Mo atomic ratio as well as attempt to deconvolute the distribution of Mo oxidation states. From XAS and chemisorption analysis, it was evident that Mo was present in multiple oxidation states; however they cannot quantify the proportion of individual Mo oxidation states. Determination of corresponding species with binding energies for Mo was based on reports in literature.[90–92] The Mo3d envelopes were fit with four species: Mo^0 (B.E. ~228.2 eV), Mo carbide-like (B.E. ~228.9 eV) and Mo^{4+} (B.E. ~230.5 eV) and Mo^{6+} (B.E. ~232.5 eV). On 5%Pt-2.5%Mo catalyst after reduction at 450°C, Mo composition is estimated to be: Mo^0 (26%), Mo carbide-like (38%), Mo^{4+} (18%) and Mo^{6+} (18%).

4.4.1.5 Temperature programmed reduction

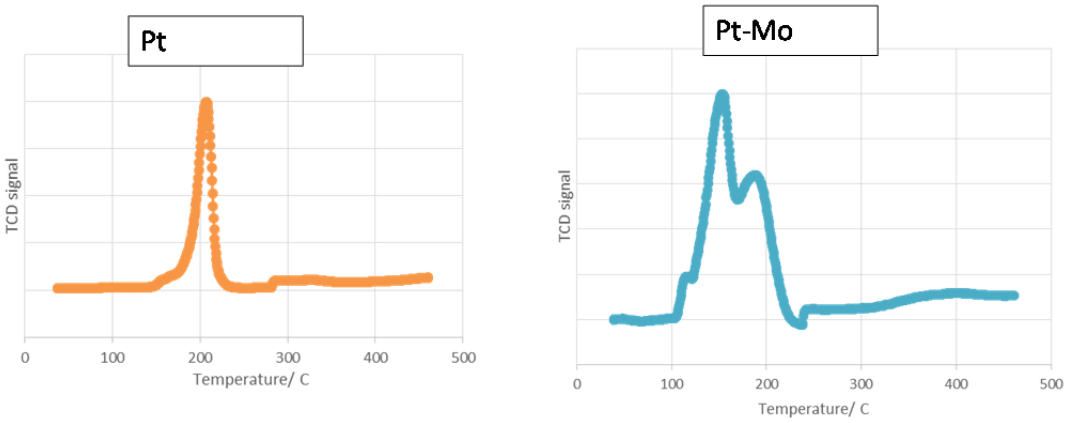

Figure 4.4 Temperature programmed reduction profile of as prepared 5%Pt and 5%Pt-2.5%Mo catalyst

Temperature programmed reduction was carried out over monometallic 5%Pt and 5%Pt-2.5%Mo as synthesized catalyst samples to estimate the overall hydrogen consumption as a function of temperature. Temperature of reduction also indicates the affinity of site and may be used to differentiate Pt and Mo sites. As expected, surface Pt reduced in a single peak at a temperature of ~200°C, compared to the bimetallic Pt-Mo which exhibited three distinct peaks. However, the quantification of overall hydrogen consumption was not useful as MWCNT support itself was found to adsorb hydrogen.

4.4.2 Reaction classes and products

Four classes of reaction were observed over Pt-based catalysts in a range of 0.1-1.9 MPa hydrogen pressure and a temperature range of 260-290°C represented below:

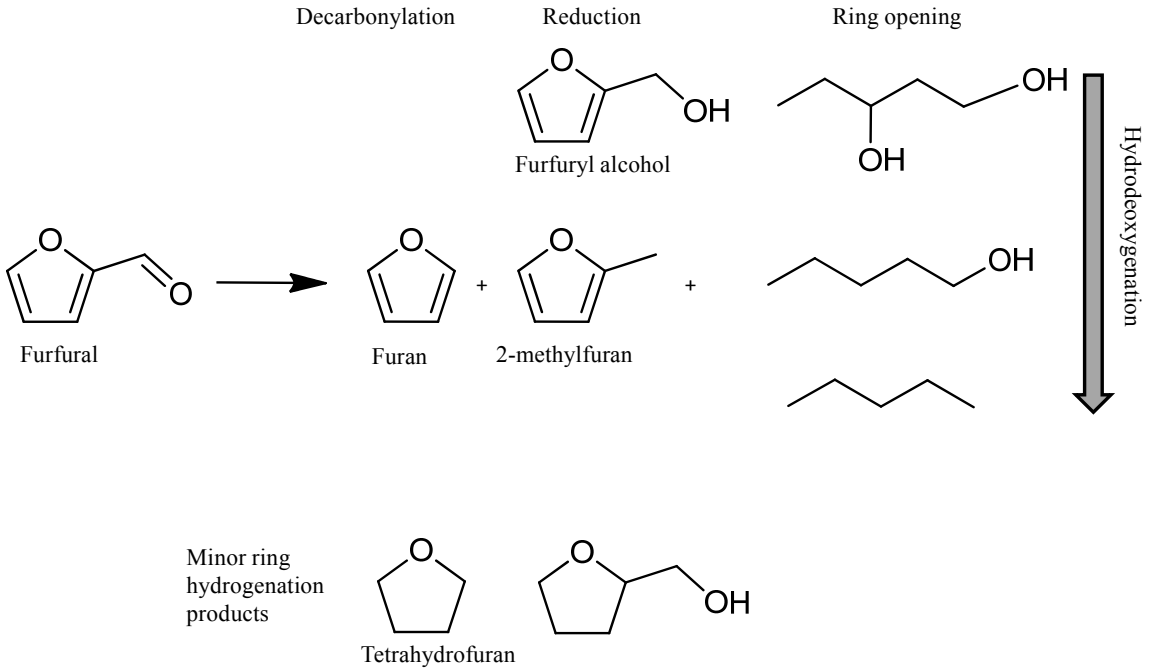

Figure 4.5 Major products and reaction classes observed for furfural hydrodeoxygenation

Decarbonylation led to loss of carbon in gas-phase as carbon monoxide and hence was undesirable. Ring opening and reduction reactions were desirable as they were a result of selective C-O bond scission through hydrogen addition. Ring hydrogenation was a minor pathway under the reaction conditions.

4.4.3 Kinetics over Pt/MWCNT

4.4.3.1 Catalyst stabilization

In literature, there are reports of catalyst deactivation attributed to particle sintering or coke formation over Pt-based catalysts. Before recording the rate measurement, catalyst was stabilized for 10-15 hours at standard conditions (furfural flow rate = 0.2 ml/min, hydrogen partial pressure = 1.9 MPa, temperature = 284°C).

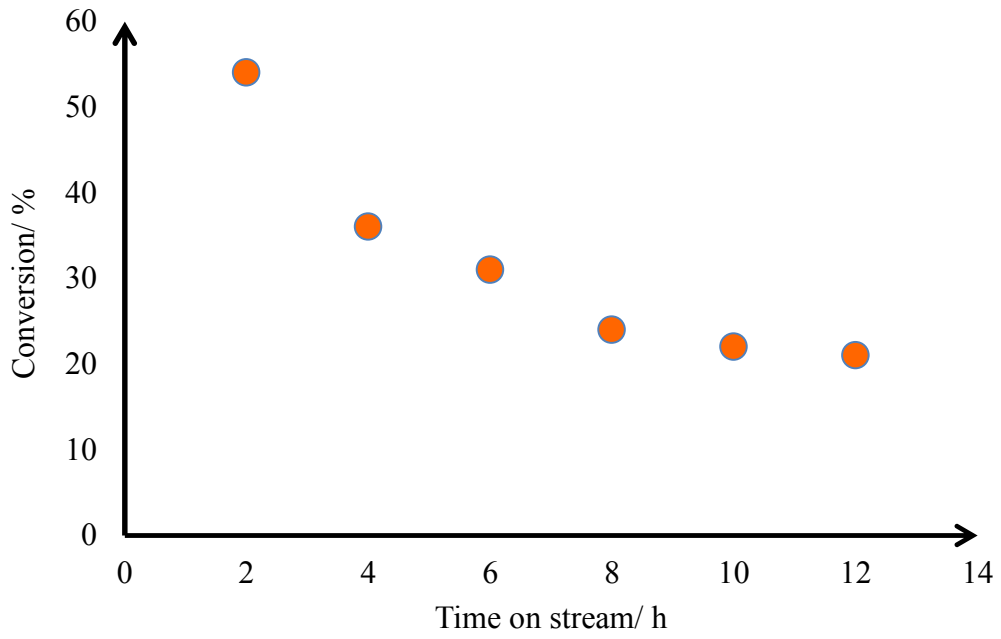

Figure 4.6 Catalyst stabilization studies over the 5%Pt-2.5%Mo/MWCNT catalyst at 1.9 MPa hydrogen pressure and a temperature of 290°C

Deactivation behavior was first-order in nature with respect to time, but the cause for deactivation could not be attributed to particle size as TEM analysis showed no significant size increase. Coking could be one of the possible causes; however quantification could not be carried out as the catalyst support itself was carbon based.

Table 4.2 Comparison of STY_{Pt} at 0.1 and 1.9 MPa hydrogen pressure for overall, decarbonylation and reduction reaction

STY_{Pt}/ 10^{-2} s^{-1}	P_{H2} = 0.1 MPa	P_{H2} = 1.9 MPa
Overall	5.6	28
Decarbonylation	4.2	9.5
Reduction	0.90	18

Decarbonylation STY_{Pt} signifies the rate of product of furan, presumably resulting from direct C-C bond scission to produce carbon monoxide as a by-product. Reduction STY represents the rate of aldehyde reduction to produce furfuryl alcohol which may further hydrodeoxygenate to 2-methylfuran.

The overall STY_{Pt} at 1.9 MPa hydrogen pressure was ~5 times higher than the STY_{Pt} at 0.1 MPa, indicating that hydrogen plays an important role in promoting the furfural consumption rate. Hydrogen also plays an influencing role in the dominant pathway and is shown to favor the desirable C-O bond scission for furfural hydrodeoxygenation. At the higher hydrogen pressure the STY_{Pt} of aldehyde reduction increased nearly 20 times compared to decarbonylation which is promoted only ~2 times.

4.4.3.2 Apparent activation energy

To elucidate the role of temperature in influencing the relative proportion of competitive decarbonylation and aldehyde reduction pathway, experiments were conducted in a range of 260-283°C. The data is presented in terms of an arrhenius plot, with apparent activation energy estimated from the slope. Decarbonylation reaction to furan exhibited an apparent activation energy of 68 kJ mol^{-1} compared to 63 kJ mol^{-1} reported in Sitthisa et al. over a Pd/SiO_2 catalyst.[93] Furthermore, reduction reaction demonstrated apparent activation energy of 83 kJ mol^{-1}, which was a minor pathway at atmospheric hydrogen pressure conditions reported in Sitthisa et al.[93]

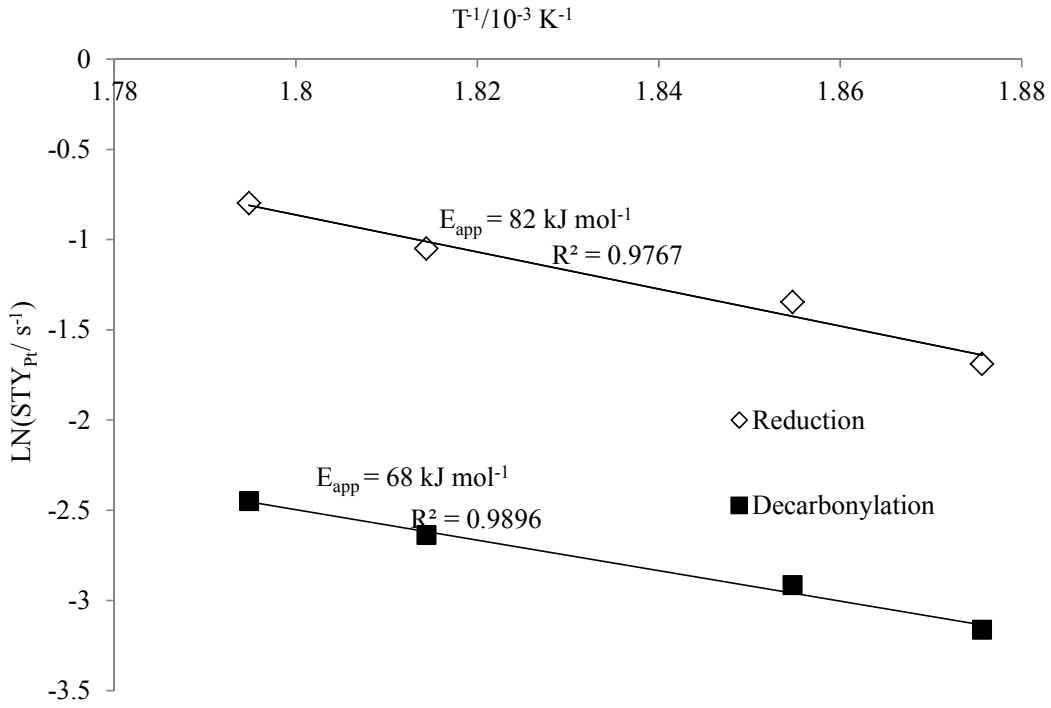

Figure 4.7 Arrhenius plot for 5%Pt/MWCNT catalyst for furfural decarbonylation and reduction in a temperature range of 260-283°C at a hydrogen partial pressure of 1.9 MPa to estimate the apparent activation energy

4.4.4 Mo promoter to Pt catalyst

Platinum even at 1.9 MPa hydrogen pressure, exhibited 20% selectivity toward decarbonylation. Adding an oxophilic promoter such as Mo has been shown to have increased C-O bond scission selectivity. Overall STY_{Pt} over 5%Pt-2.5%Mo ($2.8 \cdot 10^{-1}$ s^{-1}) catalyst was lower by ~4 times compared to 5%Pt catalyst (1.3 s^{-1}), however the selectivity of products was significantly different. Figure 4.7 shows the comparison between 5%Pt-2.5%Mo and 5%Pt catalyst at a conversion of ~20%. The undesirable decarbonylation pathway was a minor pathway over the bimetallic catalyst accounting

only for 1.5% selectivity compared to ~20% over the monometallic Pt catalyst. This was corresponded by an increase in selectivity of ring opening and reduction reactions both of which were a result of C-O bond scission.

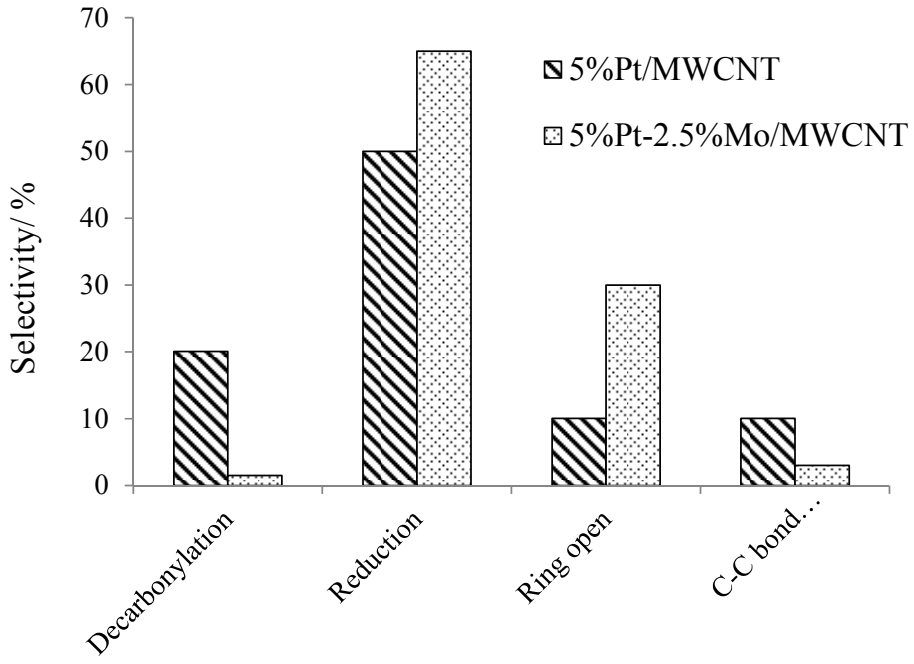

Figure 4.8 Comparison of selectivity of major reaction pathways between 5%Pt/MWCNT and 5%Pt-2.5%Mo/MWCNT catalyst at a temperature of 283°C and a hydrogen pressure of 1.9 MPa

4.4.5 Role of Pt and Mo

Since Mo significantly alters the pathway of furfural hydrodeoxygenation and also lowers the overall rate of reaction, kinetic reactions were carried out over a series of Pt-Mo catalysts. The objective of the study was to obtain a structure-activity relationship in order to elucidate the role of Pt and Mo in the overall reaction pathway. In figure below, STY_{Pt} of the aldehyde reduction is plotted against the Mo/Pt atomic ratio.

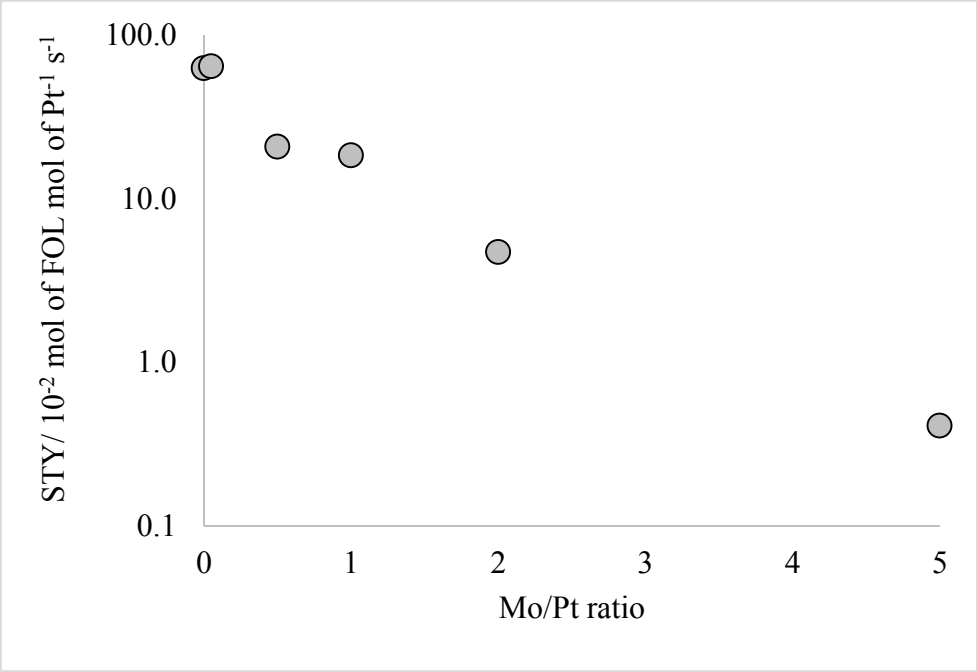

Figure 4.9 Site-time yield of aldehyde reduction as a function of Mo to Pt atomic ratio at a temperature of 280°C, hydrogen pressure of 1.9 MPa and a conversion of ~20%

There is a steady decrease in the STY_{Pt} of aldehyde reduction as Mo loading is increased from left to right. This could be a result of lower surface Pt which may directly affect the hydrogen coverage on the catalyst surface. The selectivity toward decarbonylation decreases as Mo/Pt ratio is increased with undetectable quantities of furan, direct decarbonylation product. The ring opening reaction was the dominant reaction over the 2%Pt-4.9%Mo (1:5) catalyst at 20% conversion.

4.5 Discussion

4.5.1 Catalyst characterization

The CO uptake on the series of catalysts progressively decreased as relative Mo loading increased, and an opposite trend was observed for the oxygen uptake. This qualitatively

indicates that surface Pt is lower as relative proportion of Mo is increased which might be responsible for lower CO uptake.

Combined analysis between XPS, XAS and STEM-EELS pointed out that there were observable structural and phase changes on the Pt-Mo catalysts as the Mo loading was varied.[31] The proportion of monometallic Pt particles decreased as the relative Mo loading was increased. However, the fraction of Mo in the Pt-Mo alloy particles did not show a particular trend, but the Mo-oxide and Mo carbide-like phase showed a marked increase as the Mo loading was increased. Over the 2%Pt-4.9%Mo catalyst, ~92% of particles analyzed by STEM-EELS were bimetallic opposed to ~77% over the 5%Pt-2.5%Mo catalyst. Furthermore, TPR confirmed presence of partially reduced Mo, as three distinct reduction peaks were observed over the 5%Pt-2.5%Mo catalyst as compared to a single peak over the monometallic 5%Pt catalyst.

4.5.2 Role of hydrogen

Hydrogen partial pressure has been reported to play a vital role in hydrotreating reactions such as hydrodesulphurization. However, there is a lack of fundamental studies on understanding the role of hydrogen pressure on hydrodeoxygenation of biomass model compounds partly due to equipment constraints. On 5%Pt/MWCNT catalyst, experiments were performed at 0.1 and 1.9 MPa pressure, to realize the effect on selectivity of C-C vs. C-O bond scission. At 0.1 MPa hydrogen pressure, the dominant pathway from furfural was decarbonylation to produce carbon monoxide accounting for 75% selectivity. This pathway is undesirable, as it leads to loss of carbon to gas-phase. As hydrogen partial

pressure is increased to 1.9 MPa, reduction of aldehyde to hydroxyl group becomes the dominant reaction. Hence, hydrogen pressure was shown to have an enhancing influence on keeping carbon in the liquid products. It is worth noting that decarbonylation does not result in hydrogen consumption unlike both ring-opening and reduction reactions. Furthermore, furan-ring hydrogenation was a minor pathway even at 1.9 MPa hydrogen pressure accounting in <2% overall selectivity.

4.5.3 Role of Pt and Mo

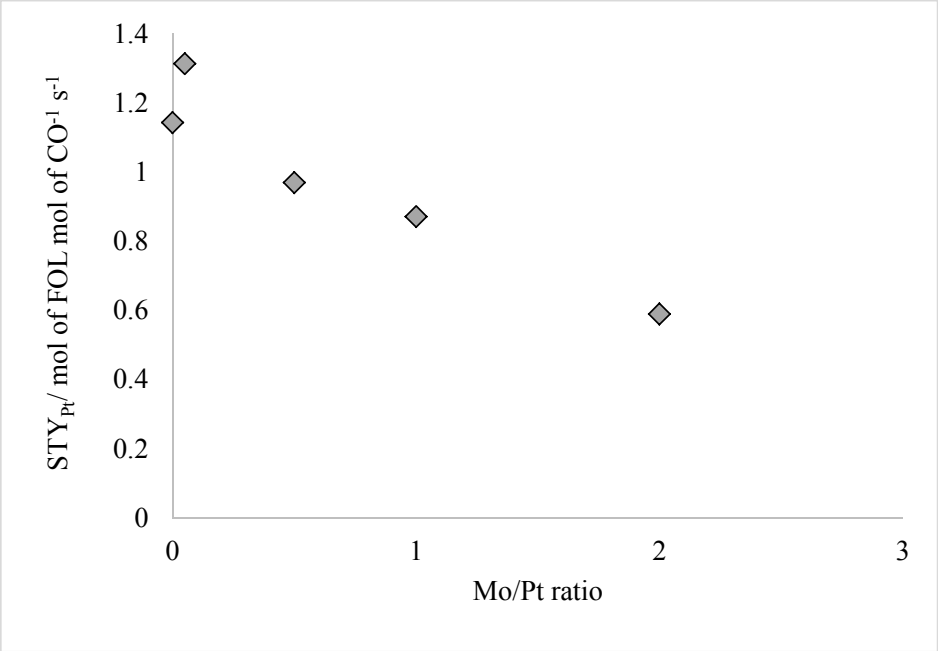

Figure 4.10 STY_{Pt} of aldehyde reduction normalized by CO chemisorption as a function of Mo/Pt ratio

The STY of aldehyde reduction normalized by total Pt loading decreased by over two orders magnitude as relative Mo loading was increased from 0 to 5 times the Pt loading (Figure 4.9). When this STY was normalized by CO chemisorption, the difference

between 5%Pt and 2.5%Pt-2.5%Mo was only ~2 times. This indicates a strong correlation between surface Pt and the rate of reaction. It is hypothesized that hydrogen activation by platinum may have a role in increased reaction rates.

As relative Mo loading is increased, the C-C bond scission pathway is shut-down indicating that sites for decarbonylation reaction were monometallic Pt nanoparticles or surface Pt atoms. The proportion of monometallic particles decreases from 50% for 5%Pt-1.2%Mo to 7.7% for the 2%Pt-4.9%Mo catalyst. The ring opening reaction was a minor pathway over the 5%Pt catalyst, however over the Pt-Mo bimetallic catalyst especially on 2.5%Pt-2.5%Mo catalyst ring opening reaction was the dominant pathway accounting for 45% selectivity.

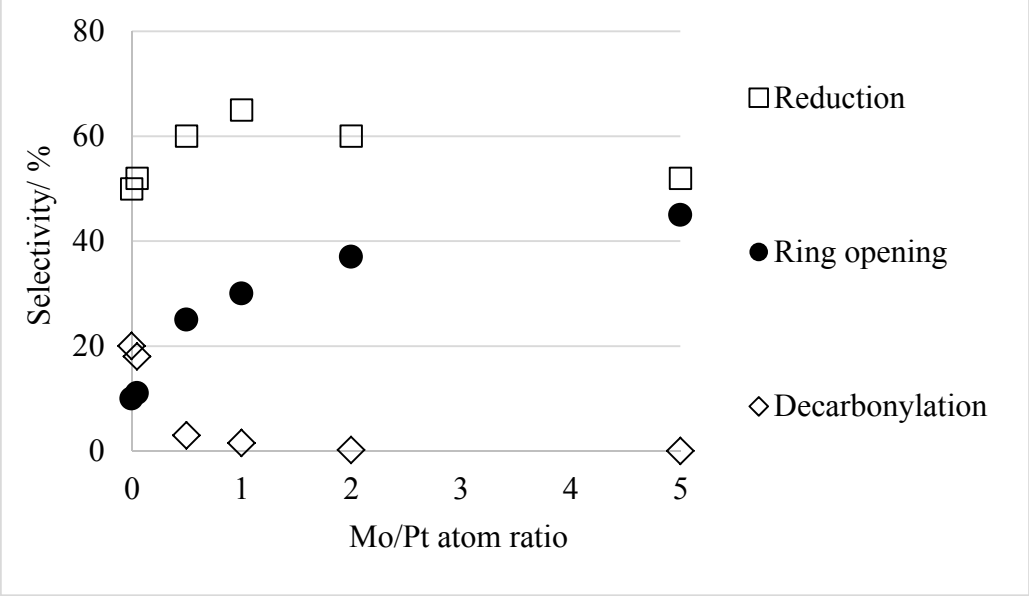

Figure 4.11 Selectivity toward reduction, ring-opening and decarbonylation reactions over the Mo/Pt atomic ratio from 0 to 5

4.6 Conclusions

Furfural hydrodeoxygenation was carried out over the bimetallic Pt-Mo catalytic system over a hydrogen pressure range of 0.1-1.9 MPa and a temperature range of 260-284°C. At 1.9 MPa hydrogen pressure over the 5%Pt/MWCNT catalyst at 284°C, the decarbonylation selectivity was ~20% compared to ~75% at 0.1 MPa at a conversion of ~20%. Furthermore, Mo promoter is shown to diminish the decarbonylation selectivity to 1.5% at 1.9MPa hydrogen pressure indicating the role of Mo in favoring the C-O bond scission. As Mo/Pt ratio was increased in the range of 0.05:1 to 5:1, the overall STY_{Pt} decreased by over two orders of magnitude. As relative Mo loading is increased the ring opening became the dominant reaction leading to aliphatic C_4 and C_5 alcohols and hydrocarbons. This suggests a trade-off between lower rate of reaction and the higher selectivity toward C-O bond scission as Pt: Mo ratio is decreased.

4.7 Acknowledgements

TEM and STEM/EELS experiments and analysis was carried out by Dr. M. Cem Akatay at Brookhaven national laboratory. XAS experiments were performed by Dr. Paul J. Dietrich and Fred Sollberger at Argonne national laboratory. XPS experiments were carried out by Dr. Dmitry Zemlyanov. Help and advice from Michael Detwiler in analysis of XPS data is appreciated.

CHAPTER 5. KINETICS OF DIHYDROEUGENOL HYDRODEOXYGENATION: ROLE OF PLATINUM, MOLYBDENUM AND HYDROGEN

5.1 Abstract

Hydrogen plays an influencing role in the pathway to dihydroeugenol deoxygenation and hence the determination of the final product. Furthermore, the platinum and molybdenum catalytic functions are shown to both be necessary and have distinct roles in the deoxygenation pathway. The bimetallic 5%Pt-2.5%Mo catalyst supported on multi-walled carbon nanotubes is able to achieve >96% yield to C_9 hydrocarbons in the range of 0.1-2.4 MPa hydrogen pressure. C-C bond scission is a minor pathway and >98% of products have a propyl-substituted six-membered carbon ring. The methoxy group undergoes reaction either through a direct cleavage to form methanol and 4-propylphenol or through a demethylation to form 4-propyl-1,2-benzendiol. The phenolic hydroxyl group undergoes a direct deoxygenation pathway at atmospheric pressure hydrogen whereas at higher hydrogen pressures, aromatic ring hydrogenation takes precedence followed by dehydration. From a comparison of pathways and site time yields, methoxy group cleavage is proposed to occur over Pt, while for phenol deoxygenation the presence of both the Pt and Mo functions is deemed critical.

5.2 Introduction

Lignocellulosic biomass is a promising renewable source to replace the petroleum-based fossil fuels in order to meet the ever-growing energy demand.[19,26] Cellulose (30-50%), hemicellulose (15-30%) and lignin (10-30%) are the three major components of lignocellulosic biomass.[10] Out of these, lignin accounts for 25-40 % of the energy content of intact biomass. Moreover, lignin is a heterogeneous polymer consisting of an aromatic backbone which can be utilized to produce aromatic compounds currently produced primarily from petroleum sources.[94] Lignin can be depolymerized via several routes including liquid-phase catalytic transformation,[18] pyrolysis/ hydropyrolysis[22,95] and extraction processes using organic solvents[96,97] which retain the oxygen content of lignin.[73,98,99] This work addresses the role of hydrogen in selective catalytic hydrodeoxygenation (HDO) of these oxygen-containing aromatic depolymerization products to hydrocarbons. Dihydroeugenol (2-methoxy-4-propylphenol) has been chosen as a representative model compound, given that it consists of phenol, methoxy and alkyl substitutions to benzene and thus contains the most important functional groups retained after lignin transformations as described in Xu et al.[97] Furthermore, a single step lignin conversion process recently reported dihydroeugenol to be one of the two major lignin-products.[18]

There is considerable interest in selective deoxygenation of phenol and methoxy-substituted aromatic compounds derived from lignin as reflected in reviews by Furimsky, Hicks, Bu et al., Wang et al. and Saidi et al.[75,100–103] The hydrodeoxygenation catalysts can be classified in to one or more of sulfided hydrotreating, zeolite and noble-metal

based catalyst categories. Lercher and co-workers have reported a combined Pd/C and phosphoric acid or HZSM-5 catalytic system to produce cyclohexane from phenol in a batch reactor system at 5 MPa of hydrogen.[104,105] Zhu et al. have utilized a bifunctional Pt/HBeta catalytic system for studying the transalkylation and hydrodeoxygenation reactions on anisole where they demonstrate the synergy of Pt and HBeta functions for deoxygenation efficacy as well as increasing carbon recovery in the liquid product.[106] Pt-Ni and Pt-Co catalysts supported on alumina have also been shown to enhance the overall deoxygenation as well as aromatic ring hydrogenation activity compared to monometallic Pt catalysts.[107] Mo has been shown to have C-O bond scission activity in its oxide form[85] or when alloyed with Pt.[87,88]

There is debate in the literature about the HDO reaction pathway to hydrocarbons, especially the deoxygenation of phenol group and influence of hydrogen pressure on the dominant pathway. Two major pathways are proposed in the literature, i) direct deoxygenation (DDO)[106,108,109] or ii) aromatic ring hydrogenation followed by deoxygenation (HYD).[104,105,107,110] The main bone of contention between the two pathways is if ring saturation is a necessity for hydroxyl removal. In the direct deoxygenation pathway the argument is that phenolic hydroxyl group can undergo deoxygenation either via C_{sp2}-O hydrogenolysis or through a partial hydrogenation/ keto-enol tautomerism followed by dehydration to recover the aromatic hydrocarbon product. Whereas in the HYD pathway it is postulated that the primary reaction is aromatic hydrogenation followed by dehydration and then dehydrogenation to aromatic hydrocarbon. Quite often these studies are carried out at disparate hydrogen pressures

ranging from 0.05 up to 10 MPa. Saidi et al.[103] in their recent review have expressed a need for a detailed analysis on the effect of hydrogen pressure on hydrodeoxygenation catalytic performance. The objective of this work was to quantify the influence of hydrogen pressure on dominant pathway to hydrocarbon as well as elucidate the roles of Pt and Mo in selective deoxygenation to produce hydrocarbons at yield approaching 100%.

5.3 Experimental methods

5.3.1 Catalyst preparation

Monometallic Pt and bimetallic Pt-Mo catalysts were prepared using the method described in Chapter 4. The monometallic Mo catalyst was synthesized by IWI of aqueous solution of ammonium heptamolybdate ($(NH_4)_6Mo_7O_{24}.4H_2O$), Sigma Aldrich) to obtain 20% wt. loading. Following this catalyst was dried in air at 150°C for 12 hours.

5.3.2 Catalyst characterization

CO uptake was measured for each of the catalysts in a Micromeritics ASAP 2020 instrument. About 120 mg of as-prepared catalyst was loaded in between two plugs of quartz wool in a flow-through tube. The catalyst was then degassed at a temperature of 250°C for 8 hours. The next step was *in-situ* catalyst reduction under hydrogen flow through a 2 hour ramp to 450°C and a subsequent hold for another 2 hours. This procedure was identical to the one used in the reactor for measurement of kinetics. Following reduction, the catalyst was evacuated at 450°C for 2 hours and subjected to a leak test at 35°C to check if the increase in pressure rise due to outgassing was <10

μmHg/min. The analysis was carried out with CO in a pressure range of 200-400 mmHg at 35°C.

5.3.3 Dihydroeugenol hydrodeoxygenation

Kinetic measurements were made in a vapor-phase fixed bed reactor capable of operating at pressures up to 7 MPa (Figure 5.1). The liquid model compound dihydroeugenol (>99%, SigmaAldrich) was fed to the top of the reactor, using an ISCO syringe pump in a flow rate range of 0.009-0.113 ml/min. Hydrogen (99.999%, Praxair, 0-5 slpm), helium (99.995%, Indiana Oxygen, 0-5 slpm), and argon (99.995%, Indiana Oxygen, 0-100 sccm) were used as carrier gases. Dihydroeugenol was vaporized at a temperature of ~150°C before mixing with the carrier gas at the top of reactor. A shielded K-type thermocouple was inserted in the catalyst bed to measure the reaction temperature. The post-reactor lines were heated to a temperature of 240°C via resistive heating to avoid product condensation. A precision orifice (Micro-orifice, O'Keefe Controls Co.) was used to step-down the pressure as well as take a slipstream (~10% of overall flow) to be sent to an online Agilent 6890N gas-chromatograph equipped with a 5973N mass spectrometer (GC-MS) through heated lines. The rest of the flow was passed through an ice-bath cooled condenser and the non-condensable gases were then dried in a coalescing filter. A back-pressure regulator was used to control the system pressure and the outlet of the regulator was vented in to the top of the hood. All products were quantified online in a previously described GC-MS system. Briefly, GC was equipped with a Supelco SPB-1 non-polar methylsilicone capillary column connected to a Flame Ionization detector and the Mass Spectrometer through a 3-way splitter to identify and quantify reaction products.

Permanent gases were quantified using a Supelco Carboxen 1000 packed column connected to a Thermal Conductivity detector. A Supelco 12718-U pre-column was used to scrub heavy reaction products before sending the permanent gases to the Carboxen 1000 packed column. The pre-column was back-flushed between every two consecutive injections. Overall and carbon mass balance was closed to within 95±5% for each experimental condition.

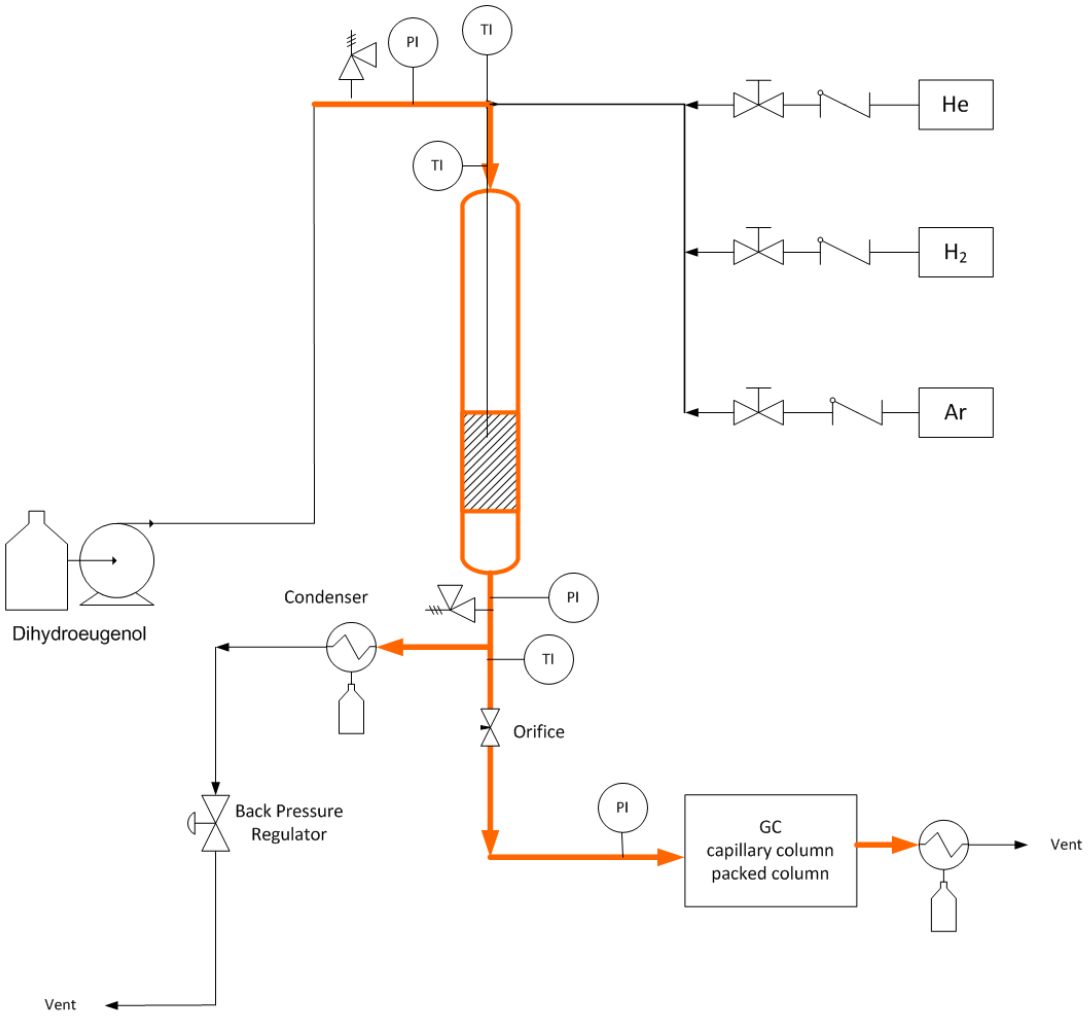

Figure 5.1 Experimental setup for DHE hydrodeoxygenation

Typical catalyst loadings were in the range of 10-500 mg, diluted with quartz powder (ground from chips sourced from Quartz Plus Inc.) to achieve enough bed height (3 times reactor internal diameter) in order to avoid channeling. Both the catalyst and quartz powder were individually sieved between 60 to 120 mesh (125-250 μm) before physically mixing them. The mixture then was loaded in a SS reactor between two plugs of quartz wool held in place by a wire mesh frit at the bottom. This catalyst was reduced *in-situ* in a flow of 50% hydrogen (100 sccm) at a total pressure of ~1.4 MPa. The temperature was linearly ramped from ambient to 450°C in 2 hours followed by a soak at 450°C for 2 hours. All kinetic measurements were conducted at 300°C with total pressure maintained at 2.4 MPa. For each experiment, the catalyst was stabilized for at least 10 hours by flowing 0.06 ml/min of dihydroeugenol and 2700 sccm of carrier gas. The carrier gas flow was comprised of 50 sccm of argon, 20-2650 sccm of hydrogen depending on the desired hydrogen partial pressure and balance helium. The catalyst was considered to be stabilized once the conversion and selectivity to major products did not vary more than ±2% between consecutive GC injections. The definitions of weight hourly space velocity (WHSV), conversion, ring product selectivity, carbon selectivity, site time yield (STY) are presented below.

The weight hourly space velocity ($\text{WHSV} = \frac{\text{gram dihydroeugenol fed}}{\text{gram catalyst} \cdot \text{h}}$) for 5%Pt-2.5%Mo/MWCNT catalyst was varied in the range of 1.6-82 h^{-1} for 0.1 MPa hydrogen pressure, 3-264 h^{-1} for 0.7 MPa hydrogen pressure and 5-661 h^{-1} for 2.4 MPa hydrogen pressure to span the conversion range from 10-99.99%. Dihydroeugenol conversion was

estimated by $X = \frac{\text{moles of dihydroeugenol reacted}}{\text{moles of dihydroeugenol fed}} \cdot 100\%$ and ring-product selectivity was defined as $S_{ring} = \frac{\text{moles of ring product}}{\text{moles of dihydroeugenol reacted}} \cdot 100\%$. Carbon selectivity estimated as $S_c = \frac{\text{moles of carbon in product}}{\text{moles of carbon in DHE feed} \cdot X} \cdot 100\%$ and was used to compare light gas products (methane, methanol, carbon monoxide and carbon dioxide). Overall STYs were estimated as $STY_{Pt} = \frac{X \cdot \text{moles of DHE fed}}{\text{moles of Pt} \cdot s}$, product STYs as $STY_{Pt} = \frac{X \cdot S_{ring} \cdot \text{moles of DHE fed}}{\text{moles of Pt} \cdot s}$. For comparing rates between Pt, Mo and Pt-Mo catalysts the STYs were normalized by total moles of metal instead of moles of Pt and were calculated as $STY_m = \frac{X \cdot S_{ring} \cdot \text{moles of DHE fed}}{\text{moles of metal} \cdot s}$.

5.4 Results

5.4.1 Catalyst characterization

CO chemisorption was performed to quantify CO uptake values for freshly reduced Pt, Mo and 5%Pt-2.5%Mo catalysts reported in Table 5.1, corresponding isotherms can be found in Appendix C. Metal dispersion was estimated by assuming a metal/CO stoichiometry of 1:1. The monometallic 20%Mo catalyst used in this study showed a CO uptake corresponding to a 9% metal dispersion. The dispersion value of Pt-Mo catalyst was lower than monometallic Pt catalyst since Mo does not chemisorb CO with the same stoichiometry as Pt.

Table 5.1 CO uptake on as prepared Pt, Pt-Mo and Mo catalyst in a range of 200-400mmHg pressure range

Catalyst	CO uptake/ μmol g^{-1}	Molar ratio of CO to metal loading
5%Pt-2.5%Mo/MWCNT	50.2	0.1
5%Pt/MWCNT	39.8	0.16
20%Mo/MWCNT	185	0.09

Detailed characterization of the 5%Pt/MWCNT and 5%Pt-2.5%Mo/MWCNT catalyst was described earlier. Briefly, transmission electron microscopy revealed that freshly reduced 5%Pt-2.5%Mo/MWCNT catalyst had an average particle size of 2.4±0.2 nm. Around 77% of nanoparticles were bimetallic Pt-Mo and the rest were monometallic Pt as shown by scanning transmission electron microscopy combined with electron energy loss spectroscopy. Moreover, X-ray absorption spectroscopy also confirmed the presence of Pt-Mo alloy. X-ray photoelectron spectroscopy showed a distribution of Mo species ranging from Mo^0 (26%), Mo carbide-like (38%), Mo^{4+} (18%) and Mo^{6+}, with an average oxidation state of 1.77 on the freshly reduced Pt-Mo bimetallic catalyst.

5.4.2 Reaction classes and major products

Three major classes of reaction were observed under the experimental conditions employed in this study viz. aromatic ring hydrogenation, methoxy transformation and phenolic hydroxyl deoxygenation. In the figure below the products are categorized according to the reaction class that they belong to:

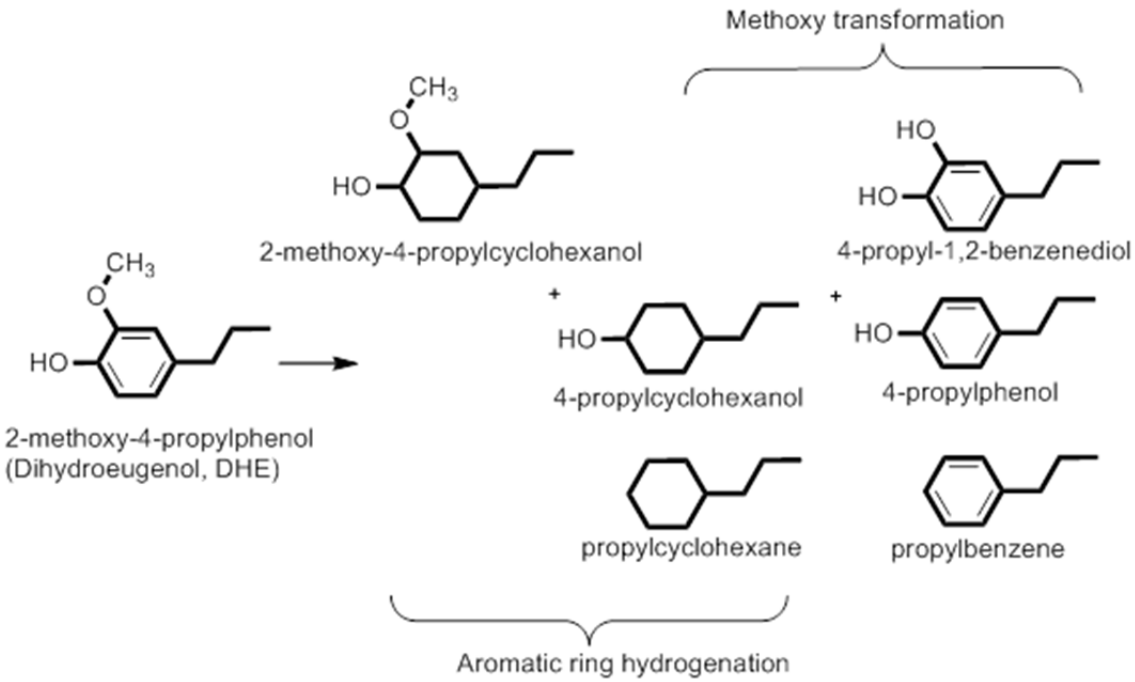

Figure 5.2 Major products and reaction classes observed for DHE hydrodeoxygenation

5.4.3 Effect of hydrogen pressure

5.4.3.1 Catalyst stabilization

The hydrodeoxygenation catalytic activity is dependent on presence of hydrogen.[111] Previously, Gualda and Kasztelan[112] have shown that decreased hydrogen partial pressure leads to increased coking in hydrotreating processes which is responsible for catalyst deactivation. Therefore, it was considered important to stabilize the catalyst at each hydrogen partial pressure for at least 10 hours before recording the rate measurement. In Figure 2 below, catalyst deactivation behavior for 0.1 MPa hydrogen partial pressure case was demonstrated over a period of 30 hours. At the end of every day the DHE flow was stopped after which the catalyst was left overnight at 300°C in a flow of 50 sccm of hydrogen and a 10-20% regeneration of catalytic activity was observed. The stabilized

conversion was achieved in a matter 2-4 hours after the start of DHE flow. The observed deactivation could be due to coking, however it could not be quantified as the catalyst support was also carbon-based.

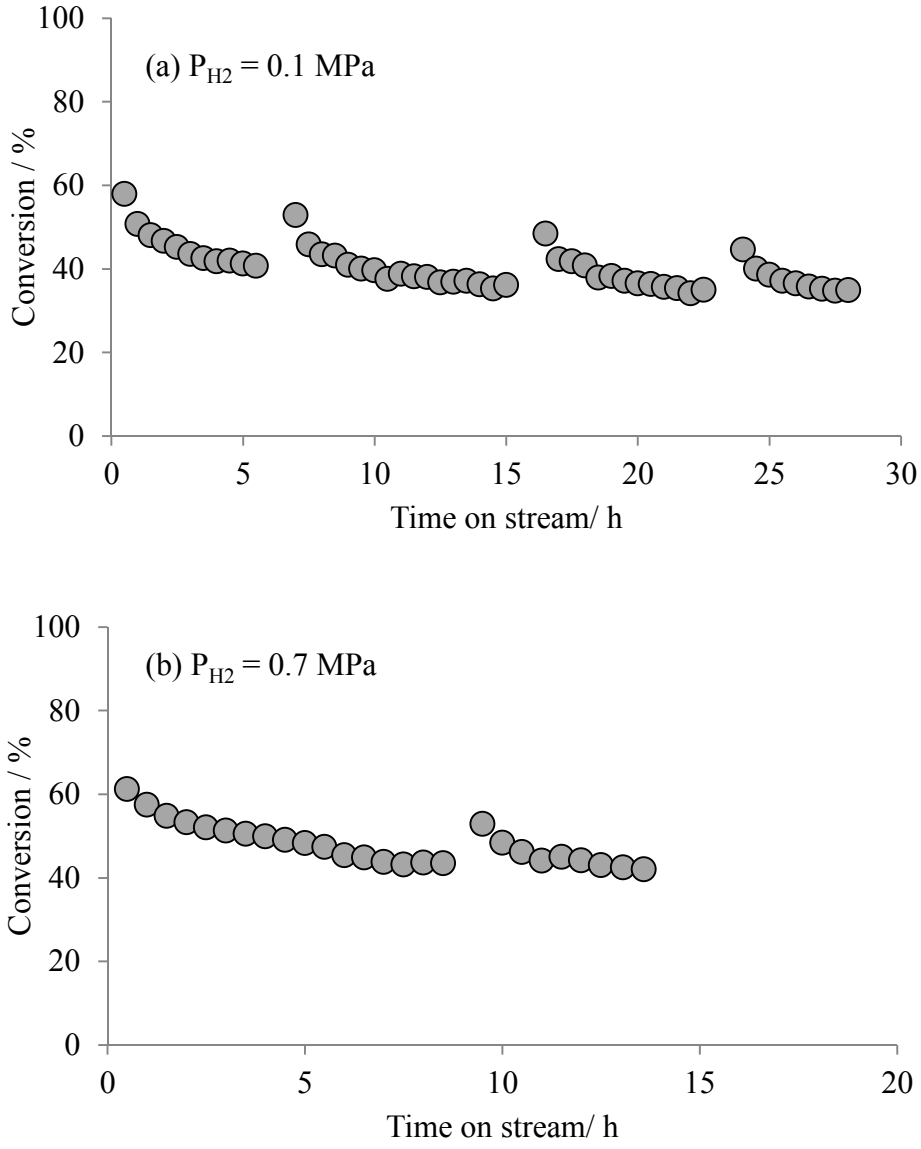

Figure 5.3 Time on stream studies for 5%Pt-2.5%Mo/ MWCNT catalyst at (a) 0.1 MPa and (b) 0.7 MPa hydrogen partial pressure at a temperature of 300°C and a weight hourly space velocity of 16 and 56 h^{-1} respectively

In a typical catalyst loading, after an initial stabilization period of 10-15 hours, space velocity studies were performed by adjusting the DHE and carrier gas flow rates given the flow constraints. At each hydrogen partial pressure, to span the entire conversion range from 10-99.99%, two to three loadings of catalyst were performed, each stabilized before measuring the rate. Rate measurements were deemed to be free of mass-transfer limitations by using the Weisz-Prater criterion,[113,114] details presented below.

5.4.3.2 Proof of kinetic control

Weisz-Prater criterion was applied to ensure that the rate measurements were free of mass transfer effects for the case of 5% Pt-Mo (1:1) catalyst, 0.1 MPa hydrogen pressure at a temperature of 300°C. Following are the details:

Rate of reaction, $r = 1.45 \cdot 10^{-5}$ mol of DHE/s/g-cat

Bulk density of the catalyst = 0.27 g-cat/cm^3

Volumetric rate of reaction, $r_v = 3.9 \cdot 10^{-6}$ mol of DHE/s/cm^3

Catalyst particle size, Rp = 125 μm

Partial pressure of reactant (DHE), P = 1.16 psi

Temperature of reaction, T = 573.15 K

Concentration of reactant at surface, Cs = concentration in the gas-phase =

$P/RT = 1.7 \cdot 10^{-6}$ mole/cm^3

Effective diffusion coefficient, D_{eff} = Knudsen diffusion coefficient = $1.8 \cdot 10^{-2}$ cm^2/s

Weisz-prater number, $N_{w\text{-}p} = 0.02$

In the case of 5%Pt-Mo (1:1) catalyst at a pressure of 2.4 MPa hydrogen pressure at a temperature of 300°C, $N_{w-p} = 0.16$

Since Nw-p value for both cases are <0.3, Weisz-Prater criterion states that the measured rate values are free of mass transfer influences.[114]

5.4.3.3 Comparison with literature

Nimmanwudipong et al.[115] have reported guaiacol hydrodeoxygenation kinetics on 1%Pt/Al_2O_3 at 300°C and 0.05 MPa hydrogen partial pressure. Their results have been extrapolated to our conditions using an assumed guaiacol order of 1 and an estimated hydrogen order of 0.7. The results indicate that the overall rate of reaction is within the same order of magnitude and a higher selectivity to direct methoxy cleavage could be attributed to acidic alumina support.

Table 5.2: Comparison of overall, demethylation and direct methoxy cleavage rate of reaction between 1%Pt/Al_2O_3 and 5%Pt/MWCNT catalysts at T=300°C, $P_{Gua/DHE}$=1.16 psi, P_{H2}=0.1 MPa

Catalyst	Rate of reaction/ 10^{-1} mole of product mole of Pt^{-1} s^{-1}		
	Overall	Demethylation	Direct methoxy cleavage
1% Pt/Al_2O_3	2.3	0.97	0.93
5%Pt/MWCNT	0.90	0.54	0.29

5.4.3.4 Aromatic and saturated hydrocarbon production

At 99.99% conversion over 5%Pt-2.5%Mo/MWCNT catalyst the overall hydrocarbon yield was in excess of 96% in a range of 0.1 to 2.4 MPa hydrogen pressure. The aromatic to saturated C_9 hydrocarbon ratio increases from 0.002 to 27.4 as hydrogen pressure decreases from 2.4 to 0.1 MPa. As shown in Figure 5.4, the relative proportion of propylbenzene and propylcyclohexane was strongly dependent on the hydrogen partial pressure. The yield of propylbenzene was 93.2% at the lowest hydrogen partial pressure of 0.1 MPa, whereas propylcyclohexane was the dominant hydrocarbon product accounting for 97.8% yield at 2.4 MPa hydrogen partial pressure. The WHSV required to achieve 99.99% conversion decreased from 5 to 1.6 h^{-1} as hydrogen pressure was varied from 2.4 to 0.1 MPa.

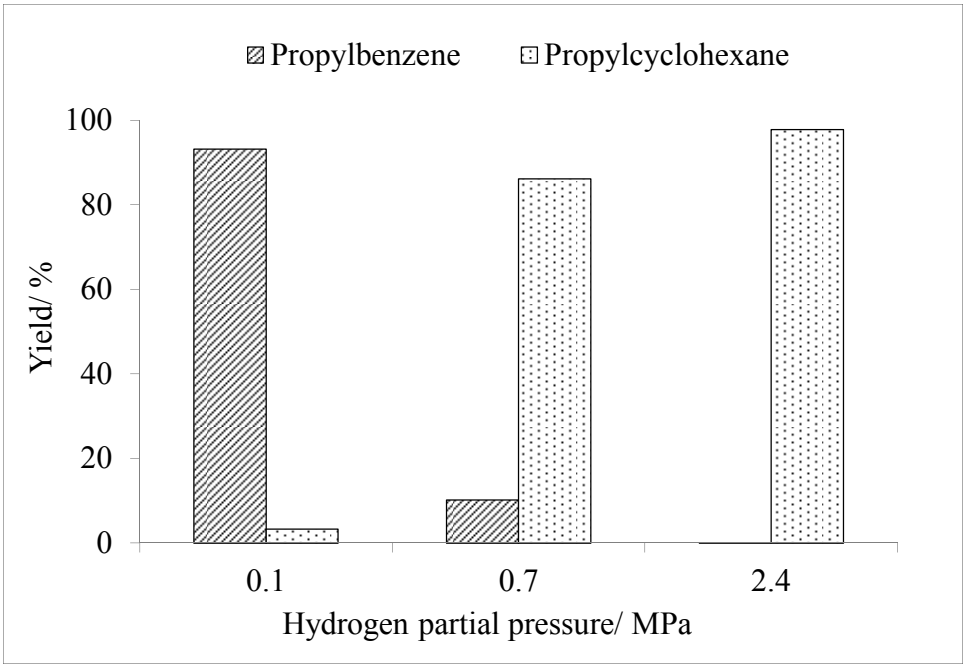

Figure 5.4 Saturated propylcyclohexane and aromatic propylbenzene hydrocarbon product distribution as a function of hydrogen partial pressure at 300°C, a DHE partial pressure of 1.16 psi, hydrogen partial pressure of 0.1 MPa, 0.7 Mpa, and 2.4 MPa using a 5%Pt-2.5%Mo catalyst

Given that noble metals (including Pt) are well-known hydrogenation-dehydrogenation catalysts, the source of aromatic hydrocarbons is often debated in the literature. The objective in this study was to track the source of propylbenzene and also compare to theoretically calculated equilibrium ratio.

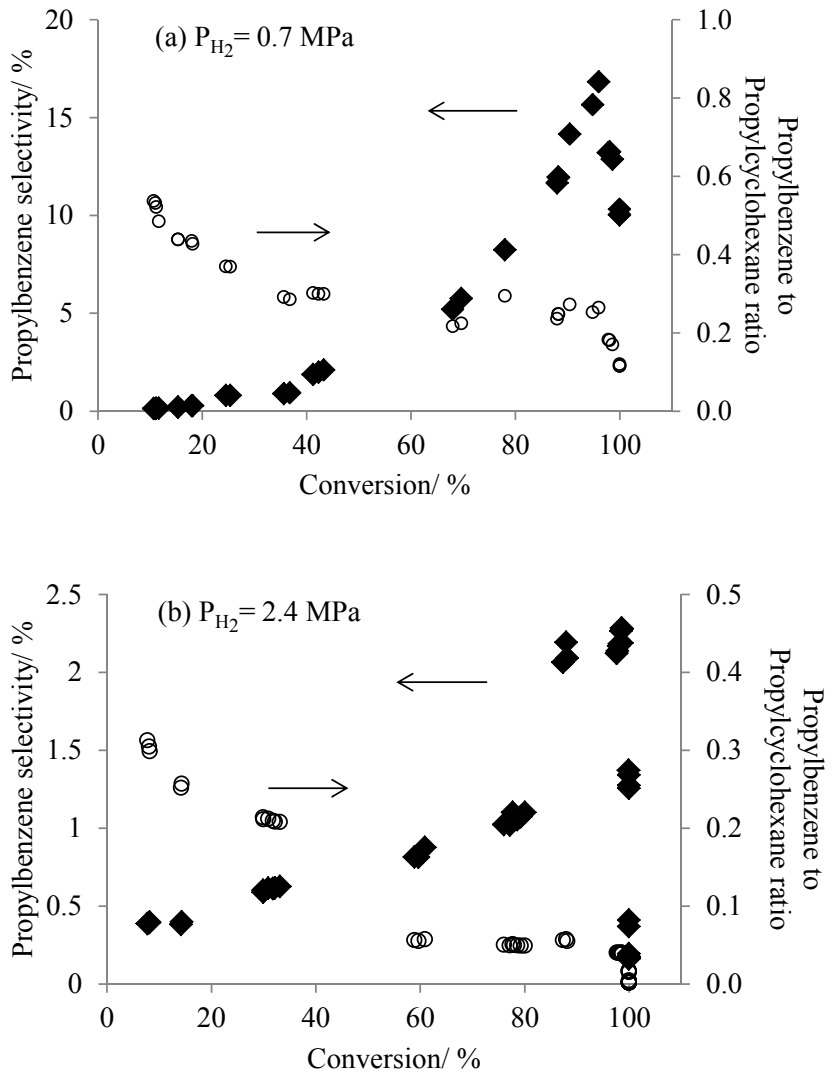

Figure 5.5 Propylbenzene selectivity (diamonds) and the ratio of propylbenzene to propylcyclohexane (circles) as a function of conversion at a hydrogen partial pressure of (a) 0.7 MPa and (b) 2.4 MPa

As shown in Figure 5.5 at 0.7 and 2.4 MPa hydrogen partial pressures, propylbenzene was consumed at a lower range of space velocities to produce propylcyclohexane. On the right-side y-axis, dependence of experimentally obtained ratio of propylbenzene to propylcyclohexane on conversion is shown. The ratio decreases from 0.54 to 0.12 at 0.7

MPa hydrogen pressure, and from 0.31 to 0.002 at 2.4 MPa indicating that proportion of ring saturated hydrocarbon increases as conversion is increased. Equilibrium constant for benzene hydrogenation at 300°C was estimated to be 0.1 atm^{-3} from Prigogine et al.[116,117] The theoretically estimated equilibrium ratios of benzene to cyclohexane at 0.7 and 2.4 MPa hydrogen pressure are then 0.03 and 0.0008 respectively, suggesting that thermodynamics would favor aromatic ring hydrogenation to saturated hydrocarbon under the reaction conditions and not the reverse reaction.

5.4.3.5 Comparison of primary reaction rate at different hydrogen pressures

As noted previously, DHE undergoes one or more of aromatic ring hydrogenation, methoxy transformation and hydrodeoxygenation reactions to produce hydrocarbon. Herein, we compare the effect of hydrogen pressure on each of these reaction classes and the overall rate of DHE consumption. Reaction rates have been defined as site time yields (STY) and normalized by Pt loading. Since the reaction network consists of consecutive series and parallel reactions and several intermediate products it was deemed impractical to co-feed all the possible products to achieve differential conditions. In the table below, STYs have been compared at a similar conversion value of ~11% to elucidate the role of hydrogen in the hydrodeoxygenation kinetics.

Table 5.3 STY_{Pt} of DHE consumption, aromatic ring hydrogenation, methoxy cleavage and total hydrocarbon production over the 5%Pt-2.5%Mo/MWCNT catalyst maintained at a temperature of 300°C, partial pressure of DHE of 1.16 psi and conversion ~11%

STY_{Pt}/ 10^{-2} mol of product (mol of Pt)$^{-1}$ s^{-1}					Apparent hydrogen order
Hydrogen partial pressure/ MPa	0.02	0.1	0.7	2.4	
Overall	1.5	5.8	19	48	0.7
Aromatic ring hydrogenation	0	0.09	6	30	1.6
Methoxy transformation	1.4	5.4	10	8.4	0.5
C_9 Hydrocarbon	0.009	0.09	0.70	0.78	1

The overall STY pertains to the consumption rate of DHE and hence is representative of the total catalytic activity. Aromatic ring hydrogenation is the sum total of STYs of primary saturated ring products for instance 2-methoxy-4-propylcyclohexanol and 4-propylcyclohexanol. Methoxy transformation takes in to account products from only methoxy cleavage such as 4-propyl-1,2-benzenediol and 4-propylphenol. Finally, C_9 hydrocarbon STY represents the total rate of propylcyclohexane and propylbenzene production.

The apparent hydrogen order was estimated from the slope of plot of the log of STY_{Pt} of product versus the log of hydrogen partial pressure (Appendix C, Figure C.2). The aromatic ring hydrogenation rate has a hydrogen order of 1.6, compared to 0.7 for the

overall reaction rate, indicating that as hydrogen pressure is increased the ring saturated products will be favored. This value is comparable to ones reported in the literature for benzene hydrogenation over Pt-based catalyst.[118,119] The C_9 hydrocarbon (propylcyclohexane and propylbenzene) rate shows a stronger dependence on hydrogen pressure compared to methoxy cleavage or the overall rate. At lower hydrogen partial pressure, 0.02 and 0.1 MPa, the primary reaction was methoxy transformation whereas at 2.4 MPa the aromatic ring hydrogenation was the principal primary reaction. Thus, the hydrogen partial pressure plays a key role in not only the overall rate of reaction but also the selectivity of products. Previously, a comparison of rates with those reported in Nimmanwudipong et al.[115] have been presented along with the details of extrapolation.

5.4.4 Pathway to methoxy deoxygenation

The methoxy group compared to phenolic hydroxyl group was relatively labile and was first to undergo transformation. However, depending on hydrogen partial pressure the methoxy cleavage either goes through a 4-propyl-1,2-benzenediol intermediate or directly to 4-propylphenol. Quantification of the relative proportion of the competitive pathway was not straightforward since 4-propyl-1,2-benzenediol also undergoes hydrogenolysis to 4-propylphenol. Furthermore, at higher hydrogen partial pressures, primary reaction was aromatic ring hydrogenation. Therefore, computing the ratio of 4-propylphenol to 4-propyl-1,2-benzenediol selectivity allows us to make a fair assessment on the favored pathway without interference from other competing reactions.

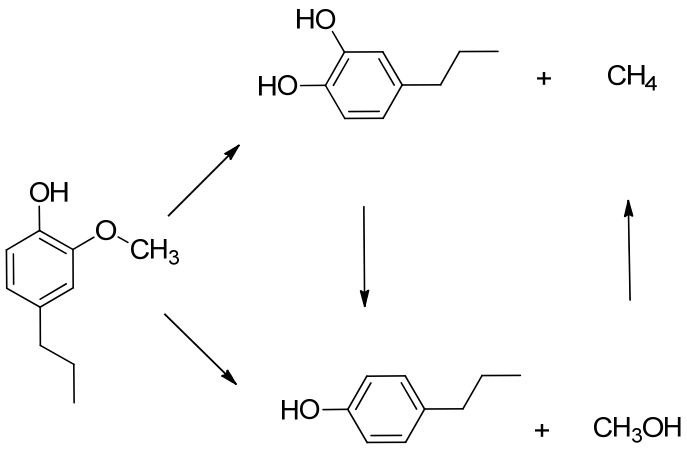

Figure 5.6 Methoxy-only transformation reaction pathway over the 5%Pt-2.5%Mo catalyst at a temperature of 300°C and a hydrogen pressure range of 0.02-2.4 MPa

Comparing at a similar conversion of ~11%, the ratio of 4-propylphenol to 4-propyl 1,2-benzenediol decreases from 5 to 0.61 as hydrogen pressure is decreased from 2.4 to 0.02 MPa. The total selectivity of 4-propylphenol and 4-propyl-1,2-benzenediol was >90% at 0.02 and 0.1 MPa hydrogen pressure, however they are minor products as hydrogen pressure is increased to 2.4 MPa.

Table 5.4 Comparison of methoxy cleavage pathway to 4-propylphenol and 4-propyl-1,2-benzenediol as a function of hydrogen partial pressure at a temperature of 300°C and an overall conversion of ~11% over the 5%Pt-2.5%Mo catalyst

Hydrogen partial pressure/ MPa	Selectivity/ %		Ratio of 4-propylphenol to 4-propyl-1,2-benzenediol
	4-propylphenol	4-propyl-1,2-benzenediol	
0.02	35.0	57.4	0.61
0.1	44.3	46.2	0.96
0.7	33.4	14.1	2.4
2.4	14.6	2.90	5.0

5.4.5 Pathway to phenol deoxygenation

In order to map the reaction pathway and distinguish the primary, secondary and tertiary reactions, trends in product selectivity as a function of conversion (WHSV studies) were plotted. Figure 5.7 shows the plots of selectivity of (a) primary, (b) secondary, and (c) tertiary products for 0.1 and 0.7 MPa hydrogen partial pressure conditions. The dominant reaction pathway for each condition was represented as a series of 3 reactions, A→B→C→D, with (A) being DHE and (D) the final C_9 hydrocarbon product. The WHSV plots for other minor products are presented in the SI along with a discussion on their role.

At 0.1 MPa hydrogen pressure, the first step was demethylation to 4-propyl-1,2-benzenediol followed by deoxygenation to 4-propylphenol or 3-propylphenol. This pathway is further corroborated by tracking the molar flow rate of methane and 4-propyl-

1,2-benzenediol as a function of conversion in the lower range. At higher conversions it is conceivable that methane may also be a result of hydrogenation of methanol, carbon monoxide and carbon dioxide. Selectivity of the ring hydrogenation product 2-methoxy-4-propylcyclohexanol was <0.6% in the entire conversion range indicating that at 0.1 MPa hydrogen pressure it was only a minor pathway. The 4-propylphenol WHSV plot went through a maximum selectivity of 71% compared to propylcyclohexanol which only reached up to 3%. Propylbenzene, as previously shown was a product of 4-propylphenol direct deoxygenation. At the lowest achieved space velocity corresponding to a conversion of 99.99%, the maximum achieved yield of propylbenzene was 93.2%.

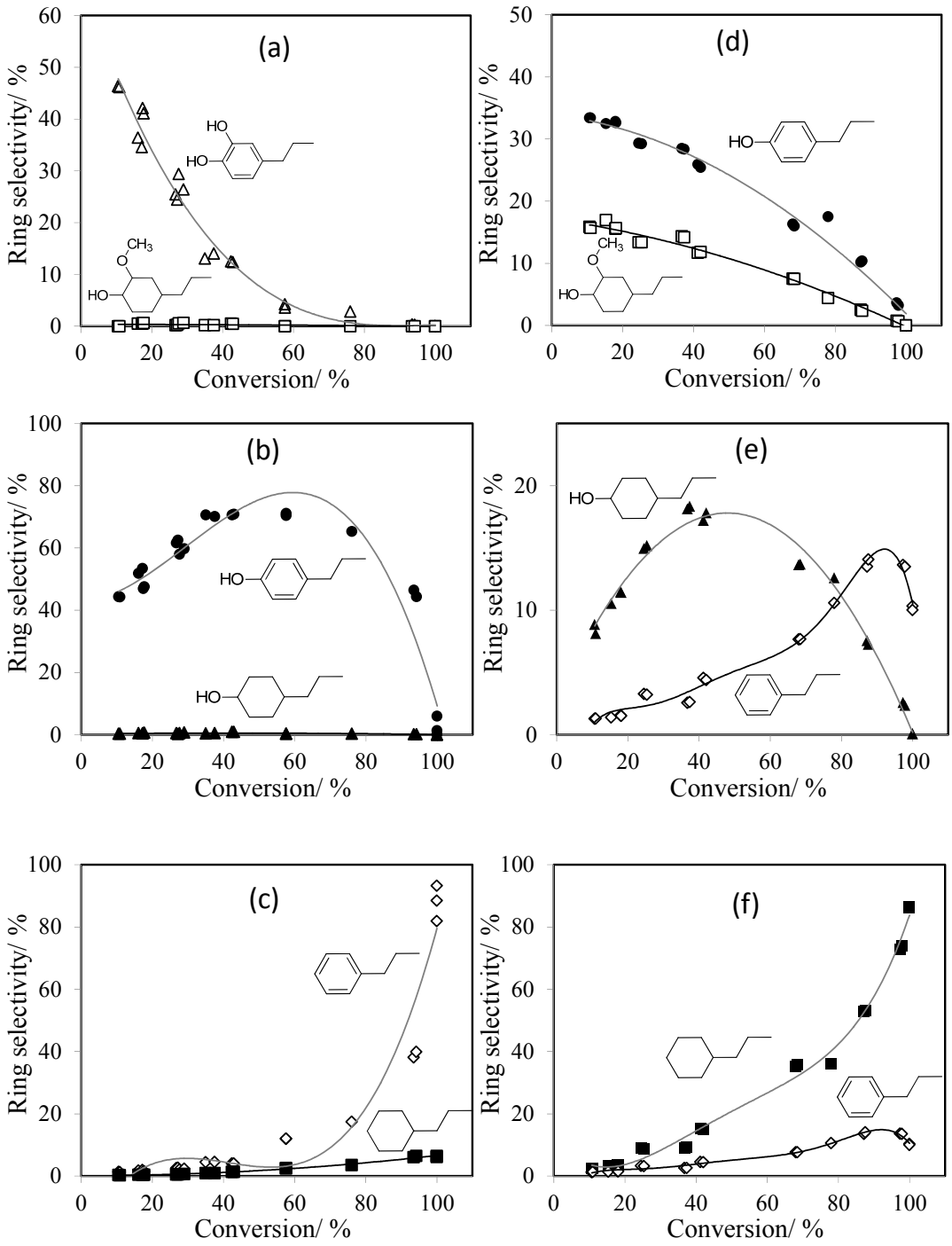

Figure 5.7 Selectivity vs. conversion (WHSV) plots for major primary (a, d); secondary (b, e); and tertiary (c, f) products at 0.1 (a, b, c) and 0.7 (d, e, f) MPa hydrogen partial pressure. Products represented in these plots are 4-propyl-1,2-benzenediol (hollow triangles), 2-methoxy-4-propylcyclohexanol (hollow squares), 4-propylphenol (circles), 4-propylcyclohexanol (triangles), propylbenzene (hollow diamonds) and propylcyclohexane (squares)

At a higher hydrogen partial pressure of 0.7 MPa, the primary reaction was methoxy loss to 4-propylphenol with a lower proportion of 4-propyl-1,2-benzenediol compared to 0.1 MPa hydrogen pressure. As opposed to the direct deoxygenation pathway, 4-propylphenol underwent ring hydrogenation to propylcyclohexanol as the major pathway. Propylcyclohexane was produced subsequently from propylcyclohexanol deoxygenation, accounting for 86.2% selectivity at 99.99% conversion. Propylbenzene accounted for 10.3% selectivity at that conversion produced through the direct deoxygenation route from 4-propylphenol.

The pathway at 2.4 MPa hydrogen partial pressure was discussed previously in detail,[31] where it was concluded that aromatic ring hydrogenation was the primary reaction followed by successive methoxy and hydroxyl group losses to give propylcyclohexane.

5.4.6 Monometallic Pt and Mo catalysts

Pt and Mo catalysts were tested to ascertain the role of each metal in the reaction pathway. Experiments were conducted at both 0.1 and 2.4 MPa hydrogen pressures, because the bimetallic Pt-Mo catalyst exhibited a distinct pathway at each of these pressures. At 2.4 MPa hydrogen pressure, data was obtained in a range of 11-97.6% conversion for 5%Pt/MWCNT and 10-99.99% conversion for 20%Mo/MWCNT. At 0.1 MPa hydrogen pressure, over the 20%Mo catalyst maximum conversion achieved was only 41%, constrained by the amount of catalyst that can be loaded in the reactor. To compare the results in a similar conversion range, data was collected over 5%Pt catalyst at 0.1 MPa hydrogen pressure from 20-60%.

5.4.6.1 5%Pt/MWNCT

At 2.4 MPa hydrogen pressure aromatic ring hydrogenation and methoxy cleavage are the dominant reaction resulting in 4-propylcyclohexanol as the major product even at 97.6% conversion. Comparatively, the selectivity toward propylcyclohexane was <5% indicating the inability of Pt to deoxygenate the hydroxyl group.

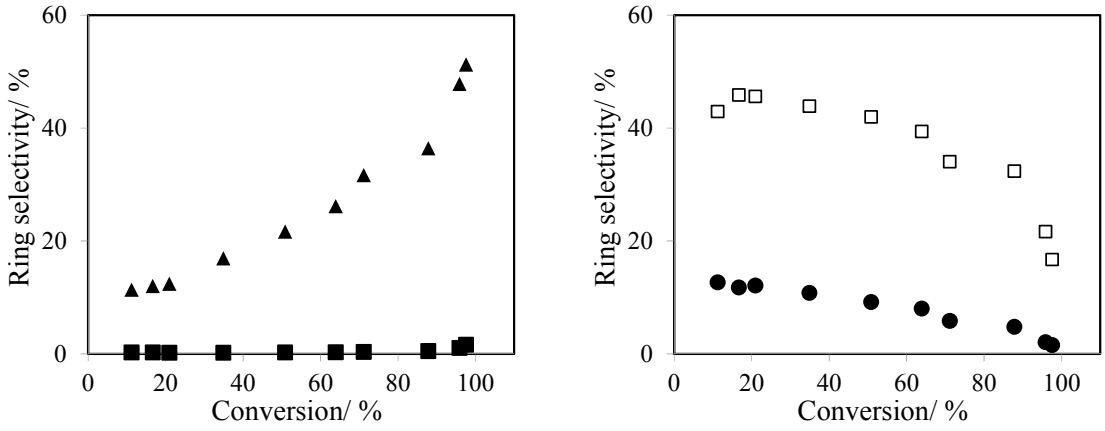

Figure 5.8 Product ring selectivity over 5%Pt/MWCNT catalyst a temperature of 300°C and a hydrogen pressure of 2.4 MPa. Legend: 2-methoxy-4-propylcyclohexanol (hollow squares), 4-propylphenol (circles), 4-propylcyclohexanol (triangles), and propylcyclohexane (squares)

At a lower hydrogen pressure of 0.1 MPa, the only major transformation occurred over methoxy group, first resulting in 4-propyl-1,2-benzenediol followed by dehydration to 4-propylphenol. This was a similar pathway to the 5%Pt-2.5%Mo catalyst at the same temperature and hydrogen pressure. The WHSV plot is presented in Appendix C.

5.4.6.2 20%Mo/MWCNT

The weight loading on the monometallic Mo catalyst was set at 20%, because the overall rate of reaction was orders of magnitude lower than Pt-based catalysts. At 2.4 MPa hydrogen pressure the pathway over the 20%Mo catalyst was direct methoxy cleavage to form 4-propylphenol accounting for ~80% selectivity. Other minor pathway over the monometallic Mo catalyst was both methoxy and methyl reattachment resulting in C10 and C11 compounds. However, to a large extent the phenolic hydroxyl group was unaffected resulting in relatively lower proportion of hydrocarbon product. In the light gas products, Mo exhibited a higher proportion of methanol to methane ratio compared to Pt-based catalysts, which may have been the reason for higher fraction of methyl reattachment products.

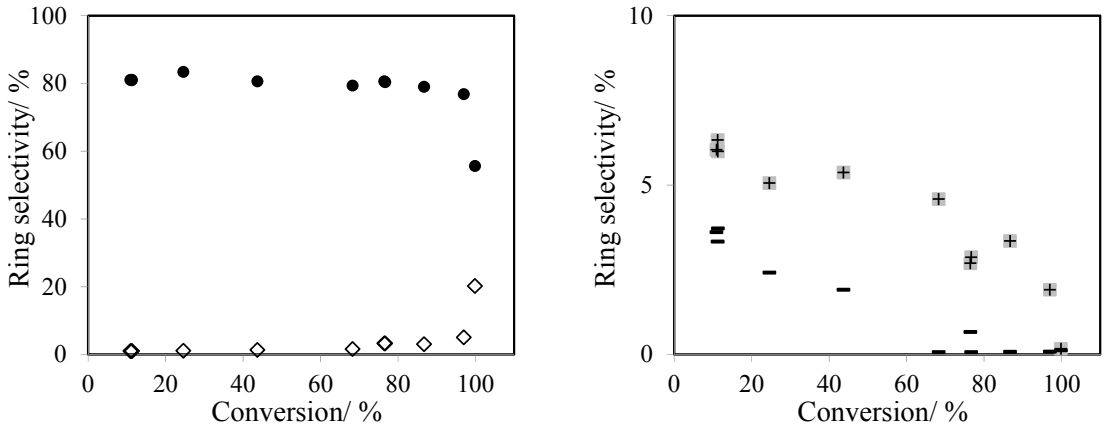

Figure 5.9 Product ring selectivity over 20%Mo/MWCNT catalyst a temperature of 300°C and a hydrogen pressure of 2.4 MPa. Legend: 4-propylphenol (circles), propylbenzene (hollow diamonds), DHE isomer (-) and 4-propyl-1,2-dimethoxybenzene (+)

5.4.6.3 Comparison between Pt, Mo and Pt-Mo

At 0.1 MPa hydrogen pressure the overall STY normalized by total metal loading (STY_m) on monometallic Pt ($8.94 \cdot 10^{-2}$ s^{-1}) was ~3 times higher than Pt-Mo ($2.90 \cdot 10^{-2}$ s^{-1}). STYs normalized by Pt loading only differ by a factor of ~1.5. The methoxy removal reaction on Pt goes through a 4-propyl-1,2-benzenediol intermediate similar to the Pt-Mo catalyst and STY was within the same order of magnitude in contrast to the monometallic Mo catalyst where the STY was an order of magnitude lower and exhibits direct methoxy cleavage. Since the STYs were computed in a low conversion range, the primary reaction STY in this case methoxy transformation, represents the key share for each of the catalytic system.

Table 5.5 STY normalized to metal loading over Pt, Mo and Pt-Mo catalysts at a hydrogen pressure of 0.1 MPa, DHE partial pressure of 1.16 psi and a temperature of 300°C in a conversion range of 11-20%

Catalyst	STY_m/ 10^{-4} mol of product mol of $metal^{-1}$ s^{-1}		
	Overall	Methoxy transformation	C_9 hydrocarbon
5%Pt/MWCNT	894	832	1.70
20%Mo/MWCNT	14.1	8	0.0197
5%Pt-2.5%Mo/MWCNT	290	270	4.37

It is worth noting that C_9 hydrocarbon STY was highest on the Pt-Mo catalyst compared to both monometallic Pt and Mo. Even though the overall STY was lower on the Pt-Mo catalyst compared to Pt by about 3 times, the C_9 hydrocarbon STY was ~3 times higher. On the monometallic Mo catalyst, the overall STY_m was 20 times lower than the bimetallic Pt-Mo catalyst and the C_9 hydrocarbon STY_m by about ~200 times. This indicates that over the Pt-Mo catalyst, Pt plays a vital role in enhancing the rate of consumption of DHE, but the presence of both Pt and Mo is critical of C_9 production.

In Figure 5.10 below, selectivity of C_9 hydrocarbon was plotted as a function of conversion across Pt, Mo and Pt-Mo catalysts. It was evident that hydrocarbon selectivity was an order of magnitude higher on the Pt-Mo catalyst compared against either Pt or Mo in a similar conversion range (10-70%).

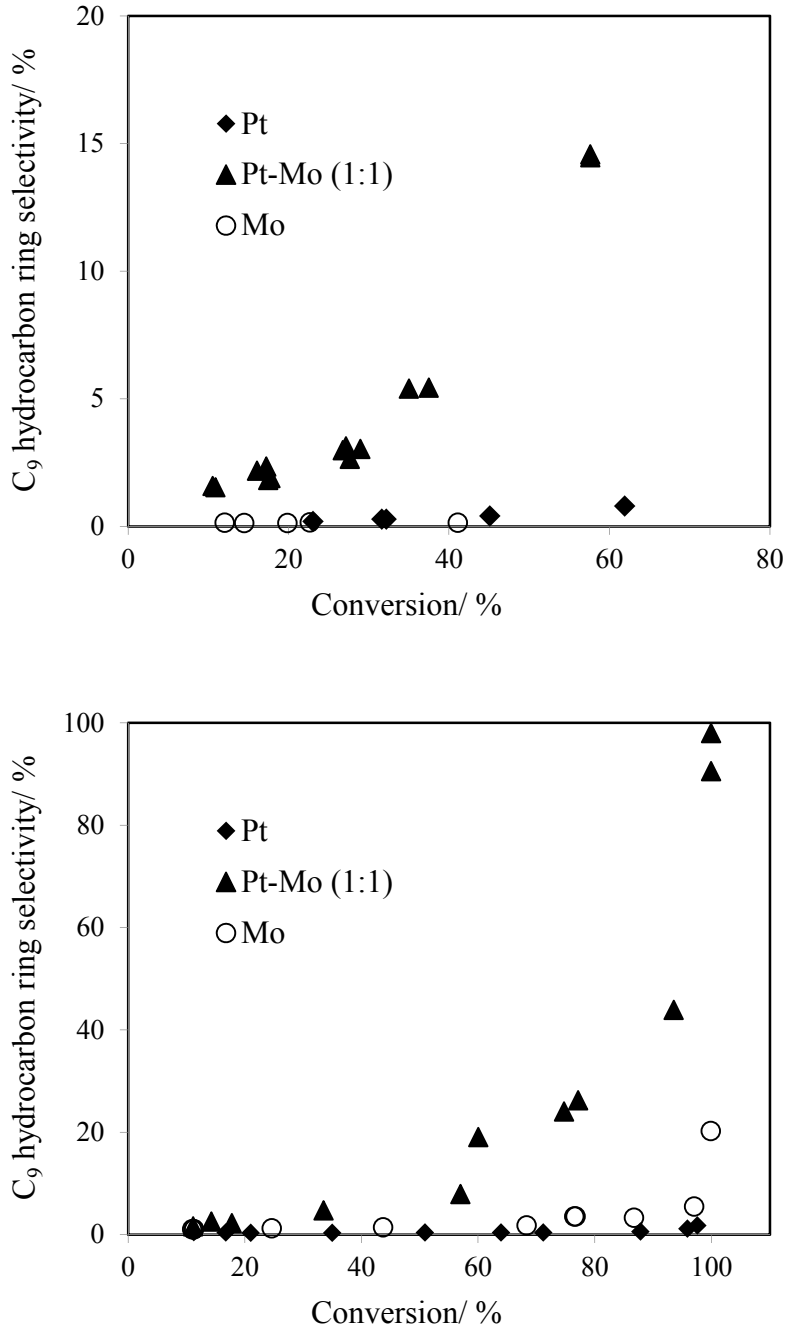

Figure 5.10 Comparison of selectivity to C_9 hydrocarbon between 5%Pt (diamonds), 20%Mo (hollow circles) and 5%Pt-2.5%Mo (triangles) catalysts at a temperature of 300°C, (a) 0.1 MPa hydrogen pressure (b) 2.4 MPa hydrogen pressure, and 1.16 psi DHE pressure.

Figure 5.10 shows that even at 2.4 MPa hydrogen pressure, Pt-Mo was proficient at deoxygenation whereas over Pt or Mo catalysts by itself the C_9 hydrocarbon was a minor product even at >97% conversions. On the monometallic Pt catalyst the major reactions were aromatic ring hydrogenation and methoxy cleavage resulting in 4-propylcyclohexanol. However, propylcyclohexane was only a minor product. Over the Mo catalyst, the major reaction was direct methoxy cleavage to 4-propylphenol at both 0.1 and 2.4 MPa hydrogen pressures. The synergy between Pt and Mo was evident in selective deoxygenation of DHE over a range of 0.1-2.4 MPa hydrogen pressure.

5.4.7 Light gas products

Methoxy group was the primary contributor to gas products including methane and methanol since the tested Pt-Mo catalyst exhibited no observed C-C cracking. That is why under most experimental conditions and catalysts the total carbon yield of C_1 products was around 10%, representing the original proportion of methoxy carbon in DHE. Carbon monoxide and carbon dioxide were secondary gas products observed from methanol reforming and water-gas shift. Methane can be produced directly through demethylation of methoxy group or through methanol / carbon monoxide / carbon dioxide hydrogenation. The relative proportion of each of these species was a function of hydrogen partial pressure as well as the conversion (Figure 5.11).

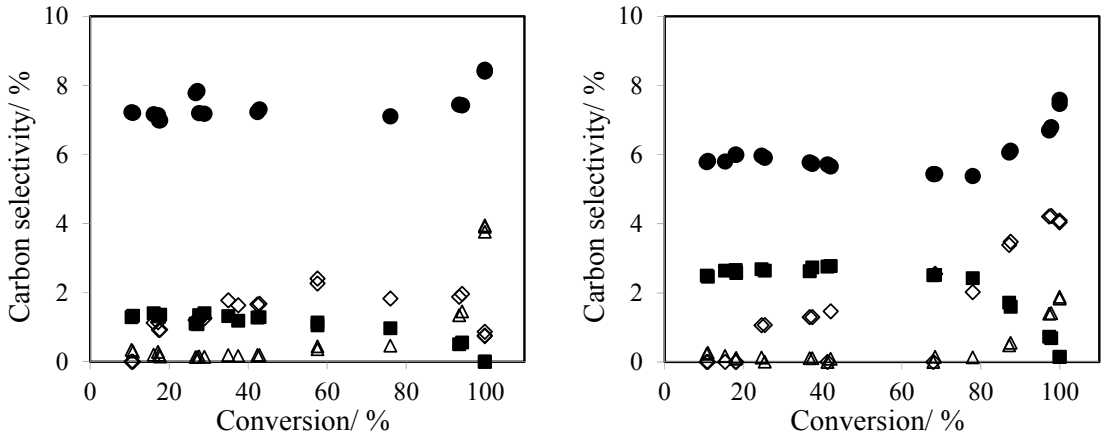

Figure 5.11 Carbon selectivity of methane (circles), methanol (squares), carbon monoxide (diamonds) and carbon dioxide (triangles) as a function overall conversion at (a) 0.1 MPa and (b) 0.7 MPa hydrogen pressure over the 5%Pt-2.5%Mo catalyst at a temperature of 300°C and DHE partial pressure of 1.16 psi.

5.5 Discussion

5.5.1 Catalyst characterization

Based on multiple characterization techniques described previously, the freshly reduced 5%Pt-2.5%Mo/MWCNT catalyst was shown to have bimetallic Pt_xMo_y, monometallic Pt nanoparticles as well as bulk Mo-oxide or carbide-like regions. The average particle size increased from 2.4 ± 1.4 nm to 2.5 ± 1.3 nm indicating no significant change in particle before and after the reaction. CO chemisorption gives a lower dispersion value than was expected from the particle size due to one of the two reasons, a) Mo does not adsorb CO with a 1:1 stoichiometry and b) the bimetallic Pt-Mo catalyst has fewer Pt surface sites.

5.5.2 Direct deoxygenation pathway to propylbenzene

For propylbenzene, the space velocity studies at 0.7 and 2.4 MPa show that at >95% conversion propylbenzene was being consumed to produce propylcyclohexane. This

proves that under experimental conditions the thermodynamics favor hydrogenation of aromatic ring and that propylbenzene was not a dehydrogenation product of propylcyclohexane. Further support was obtained by comparing the saturated to aromatic hydrocarbon ratios to the estimated equilibrium ratio under the experimental conditions. Even at the lowest space velocity, corresponding to the highest conversion the ratio of propylbenzene to propylcyclohexane is higher than the equilibrium ratio at both 0.7 and 2.4 MPa hydrogen pressure. Therefore, equilibrium calculations also predict that aromatic ring hydrogenation was the favored reaction and the propylbenzene was a result of direct deoxygenation of 4-propylphenol. This result is in agreement to a recent report published by Nie and Resasco.[109] This could be done via either of three pathways, i) direct C_{sp2}-O hydrogenolysis or ii) partial hydrogenation of the aromatic ring, and dehydration back to give propylbenzene or iii) keto-enol tautomerization followed by keto hydrogenation and dehydration. The intermediate products in each of these pathways are hypothesized to be very reactive and therefore not present in detectable limits of the analytical system.

5.5.3 Methoxy transformation

Methoxy group undergoes transformation either through demethylation or direct cleavage to produce methanol and 4-propylphenol. As noted above, the product of demethylation, 4-propyl-1,2-benzenediol itself undergoes reaction to form 4-propylphenol. However, the presence of methanol also indicates a portion of 4-propylphenol was a result of direct methoxy cleavage from DHE. Methanol yield cannot be used to estimate the rate of direct cleavage because methanol itself undergoes reforming or hydrogenation to produce

carbon monoxide, carbon dioxide and methane. Therefore, the trend in ratio of 4-propylphenol to 4-propyl-1,2-benzenediol should only be taken as qualitative indicator of the relative effect of hydrogen pressure on both the reactions. The increased hydrogen pressure leads to the ratio in favor of 4-propylphenol signifying that either the direct methoxy cleavage or the 4-propyl-1,2-benzenediol hydrogenolysis are preferred over demethylation. Another implication was on the relative yield of methane (from demethylation) and methanol (direct methoxy cleavage). As a consequence, when compared in the10-60% conversion range the yield of methane was higher at lower hydrogen pressure. In literature there are reports on utilizing methanol to add a methyl substituent to an aromatic ring.[120] Over Pt and Pt-Mo catalysts, <1% of products have methyl reattached back to the aromatic ring since methanol hydrogenation to methane was preferred. Therefore, the theoretical carbon yield of the liquid product was 90% with the current process. However, increasing the methanol yield over an alternative catalyst could lead to a C_{10} product with potential to recover 100% carbon in the liquid product.

5.5.4 Phenolic hydroxyl deoxygenation

WHSV studies were carried out at 0.1, 0.7, 2.4 MPa hydrogen pressure to decipher the major primary, secondary and tertiary products. Typically, products demonstrating a monotonically decreasing selectivity as conversion increases were categorized as primary products. Secondary products commonly exhibited a maximum in the WHSV plot in the mid-conversion range (40-80%). Additional information regarding the relative value of rate constants of series reactions can be obtained by locating the position of maximum. However, given that products were not co-fed, the concentration of intermediates varied

along the catalyst bed, comparison was not made between the rate values of individual steps of the series reaction. Tertiary products in this case hydrocarbons, demonstrated a continuous upswing in selectivity as conversion was increased. The presented pathway was based on the observed products and there are likely reactive intermediates that were not included in the discussion since they were not present in identifiable quantities.

Previously, methoxy group deoxygenation pathway was shown to be dependent on the hydrogen partial pressure. At 0.1 MPa hydrogen pressure (Figure 5.12a), 4-propylphenol was observed as a secondary product resulting from 4-propyl-1,2-benzenediol hydrogenolysis. Direct deoxygenation of 4-propylphenol led to propylbenzene with an overall yield of 93.2%.

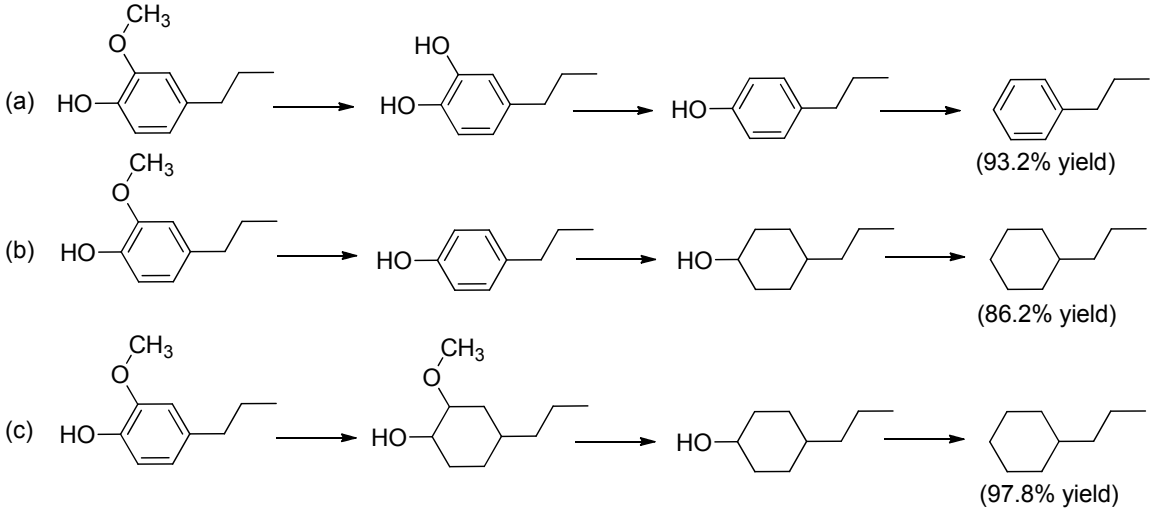

Figure 5.12 Major DHE hydrodeoxygenation pathway at (a) 0.1 MPa, (b) 0.7 MPa and (c) 2.4 MPa hydrogen partial pressure represented as a series of 3 reactions, A→B→C→D at a temperature of 300°C over Pt-based catalysts.

Figure 5.12b shows the major pathway at 0.7 MPa hydrogen pressure, with 4-propylphenol as the leading primary product compared to ring hydrogenation product, 2-methoxy-4-propylcyclohexanol. Unlike 0.1 or 2.4 MPa hydrogen pressure, there was not one dominant deoxygenation pathway and the competitive pathways had selectivity within the same order of magnitude. Under these conditions, aromatic ring hydrogenation was preferred over direct deoxygenation to produce 4-propylcyclohexanol. The deoxygenation of 4-propylcyclohexanol resulted in propylcyclohexane with an overall yield of 86.2%. The competitive direct deoxygenation pathway resulted in 10.3% yield of propylbenzene. The dominant pathway at 2.4 MPa hydrogen pressure was aromatic ring hydrogenation to 2-methoxy-4-propylcyclohexanol followed by methoxy cleavage and dehydration to propylcyclohexane.

Between the methoxy and phenol substituent, the former was under all experimental conditions the first substituent to be deoxygenated. Only at 0.1 MPa hydrogen pressure, direct deoxygenation of phenol was a major pathway to produce propylbenzene. At both the higher hydrogen pressures (0.7 and 2.4 MPa), aromatic ring hydrogenation preceded hydroxyl dexoygenation.

Minor product pathway at 0.1 MPa hydrogen pressure was direct phenolic hydroxyl deoxygenation to produce 3-propylanisole. At 0.7 MPa hydrogen pressure, minor parallel pathways were aromatic ring hydrogenation to 2-methoxy-4-propylcyclohexanol and direct phenolic hydroxyl deoxygenation to produce 3-propylanisole (Appendix C).

5.5.5 Role of Pt and Mo

At 0.1 MPa hydrogen pressure, the overall STY_{Pt} was ~1.5 times lower for Pt-Mo catalyst compared to Pt. This could be due in part to either lower surface Pt on the bimetallic catalyst or a lower inherent rate for the alloyed Pt-Mo nanoparticle. However, the pathway of methoxy deoxygenation was alike for both Pt and Pt-Mo catalyst indicating similar catalytic sites are responsible. Monometallic Mo catalyst exhibits a STY_m about 20 times lower than the Pt-Mo catalyst.

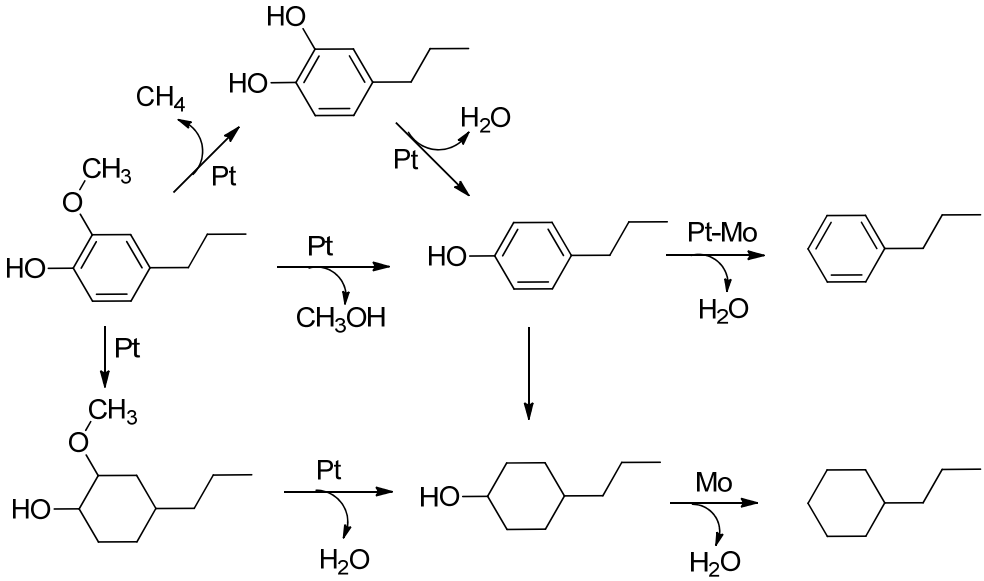

Figure 5.13 Proposed DHE hydrodeoxygenation pathway at a temperature of 300°C by comparison of results over 5%Pt, 20%Mo and 5%Pt-2.5%Mo catalyst at hydrogen partial pressure of 0.1 and 0.7 MPa

The C_9 hydrocarbon STYm was about ~3 times higher over the Pt-Mo catalyst compared to Pt catalyst even though the overall STYm is lower by 3 times. This is consistent with the finding that the selectivity to C9 hydrocarbons was an order of magnitude higher over

the Pt-Mo catalyst (Figure 5.10). Over the Pt catalyst at 14.2 psi hydrogen pressure up to 60% conversion, 4-propylphenol and 4-propyl-1,2-benzenediol were the major products, accounting for >85% selectivity. The Mo catalyst at 14.2 and 342 psi hydrogen pressure, however, exhibited minimal aromatic ring hydrogenation activity. The major product, even at 99.99% conversion over the Mo catalyst at 342 psi, was 4-propylphenol indicating that while methoxy group was cleaved, the phenolic hydroxyl group was unaffected. Isomerization and transalkylation reactions were other side reactions observed over the Mo catalyst. One of the reasons for transalkylation activity over Mo catalyst could be a due to higher proportion of methanol compared to other Pt-based catalysts.

Combining data from WHSV studies from experiments at 14.2 to 342 psi hydrogen pressure and over the PtMo, Pt, and Mo catalysts, Figure 5.13 represents possible catalytic contributions for the different classes of reactions. In summary, experiments over the Pt only and Mo only catalysts reveal that neither of them alone is sufficient to complete deoxygenation of DHE. Comparing the STYm, the overall rate of reaction is lower on Pt-Mo alloy catalyst compared to monometallic Pt, but the STYm of C9 hydrocarbon production is higher over the bimetallic Pt-Mo. This is further evidence for the need of the presence of both Pt and Mo for selective deoxygenation of DHE to hydrocarbons. Our data are not sufficient, however, to differentiate the relative importance of PtMo alloy formation versus close proximity of Pt and Mo phases.

5.5.6 Light gas products

Methane and methanol were the gas products obtained primarily from methoxy transformation reaction. The relative proportion of methane to methanol was dependent on both the hydrogen pressure and overall conversion. In the lower conversion range, the ratio of methane to methanol increased as the hydrogen pressure was decreased. This was due to the pathway of methoxy transformation, which underwent demethylation at 14.2 psi hydrogen pressure, whereas at the 97 and 342 psi hydrogen pressures direct cleavage to form methanol was dominant. As the conversion was increased to beyond 60-70%, the selectivity to methanol decreased, with a corresponding increase in methane and carbon dioxide selectivity. The drop in methanol selectivity was due in part to methanol reforming to carbon dioxide or methanol hydrogenation to methane. Moreover, methanol could also decompose to carbon monoxide, and followed by water-gas shift reaction lead to carbon dioxide. Furthermore, both carbon monoxide and carbon dioxide could possibly undergo methanation reactions. At lower hydrogen pressures the carbon dioxide yield was significant due to water-gas shift reaction which was inhibited as hydrogen pressure was increased. The total carbon yield for light gas products (methanol, methane, carbon monoxide, carbon dioxide) was 11-13%. In theory the maximum carbon yield should be 10% if the only source was the methoxy substituent. However, there were minor ring-opened products including propylcyclopentane and aliphatic heptanes which also would contribute to light gas products.

5.6 Conclusions

In this study variation of hydrogen pressure over the range from 3 to 342 psi has been shown to have a significant effect on the hydrodeoxygenation kinetics of dihydroeugenol, a lignin-based model compound. A bimetallic Pt-Mo catalyst supported on MWCNT is able to carry out hydrodeoxygenation of both the methoxy and phenolic hydroxyl groups to produce >96% yield of C9 hydrocarbons and up to 93.2% yield of propylbenzene at 14.2 psi hydrogen pressure. Furthermore, propylbenzene is shown to be a result of direct deoxygenation pathway and not a consequence of propylcyclohexane dehydrogenation under the reaction conditions. The methoxy group is the first substituent to undergo a transformation either through demethylation or direct cleavage to produce methanol, depending on hydrogen pressure. Aromatic ring hydrogenation is the favored reaction at higher hydrogen pressures where saturated ring hydrocarbon products dominate. At 14.2 psi hydrogen pressure the phenolic hydroxyl group undergoes direct deoxygenation to produce propylbenzene, whereas at higher hydrogen pressures the aromatic ring hydrogenation takes precedence followed by dehydration. The methoxy removal occurs on the monometallic Pt catalyst as well, with the same pathway and a similar STYPt. The Pt only and Mo only catalysts by themselves are not proficient at phenolic hydroxyl removal in a range of 14.2-342 psi hydrogen pressure and their combined presence is vital for complete deoxygenation.

5.7 Acknowledgement

Experimental data at 2.4 MPa hydrogen partial pressure was collected by Dr. Sara L. Yohe.

CHAPTER 6. SUMMARY AND FUTURE RECOMMENDATIONS

6.1 Summary

This dissertation was aimed at identifying the descriptors that control the product distribution from thermochemical processing of biomass or biomass-derived oxygenates. Fundamental studies were carried out using carefully chosen model compounds to represent specific processes as well as help gain insights in to the chemical transformation. Water-gas shift study indicated the kinetics was significantly altered in presence of liquid water. The carbon monoxide reaction order increased to ~0.9 from ~0.1 in presence of liquid water indicating considerable decrease in the carbon monoxide coverage over the catalyst.

In cellulose fast hydropyrolysis, residence time and temperature were shown to have a substantial impact on product distribution. At a millisecond timescale, the cellulose hydropyrolysis revealed that the polymeric chain underwent scission to produce a mixture of levoglucosan, cellobiosan and other oligomer anhydrosugars. Comparing the results to a conventional lab-scale reactor operating at a residence time of 1-3 seconds, it was hypothesized that oligomers (mainly cellobiosan) degraded to levoglucosan and other lighter molecules as the residence time was increased. Furthermore, increasing the hydropyrolysis temperature in the range of 500-700°C resulted in thermal cracking which

increased the contribution of C_2 compounds such as formic acid and glycolaldehyde in the product distribution.

Catalytic hydrodeoxygenation of biomass model compounds has been demonstrated to go through a complex network of series and parallel reactions. The catalyst used in this study was a bimetallic Pt-Mo supported on inert multi-walled carbon nanotubes. The dual functionality of the catalyst was deemed critical to obtain 100% hydrodeoxygenation. A correlation between the overall rate of reaction and the surface Pt was observed for both furfural and dihydroeugenol hydrodeoxygenation. It is possible that surface Pt played a decisive role in hydrogen activation which is a key aspect for the rate of hydrotreating reactions. As Mo loading was increased on the bimetallic catalytic system, the extent of deoxygenated products was higher when compared at similar values of conversion. Given that Mo is a known oxophilic metal, it was hypothesized to be responsible for C-O bond scission.

In Chapters 4 and 5, hydrogen is shown to manipulate the dominant pathway for both furfural and dihydroeugenol hydrodeoxygenation. This resulted in a product distribution that was a function of the hydrogen partial pressure. Over furfural, it was shown that higher hydrogen pressure was instrumental in increasing the overall carbon yield of the liquid product. On the contrary, at higher hydrogen pressure dihydroeugenol exhibited an increasing degree of aromatic-ring hydrogenation which is undesirable. The common theme in both these studies was the role of hydrogen in increasing the overall rate of reaction. This not an unexpected result as hydrodeoxygenation proceeds through

consumption of hydrogen to deoxygenate the model compound. Although, hydrogen increases the rate of each individual reaction reported in this study, it does so at a different extent. This caused an impact on the product distribution as hydrogen pressure was varied in the range of 0.1 to 2.4 MPa. A preliminary study also suggested that temperature has an influential role in selectivity of different pathways.

6.2 Future recommendations

6.2.1 Kinetics of phenol hydroxyl deoxygenation

Using dihydroeugenol as a model compound with both methoxy and phenol group substitutions, the primary reaction invariably involved transformation of the methoxy group. In Chapter 5, kinetics of methoxy transformation and the effect of hydrogen pressure were discussed. Given that the concentration of intermediate products varied along the catalyst bed, accurate kinetic data was not available for phenol deoxygenation which was a secondary/ tertiary reaction. Phenol deoxygenation has been claimed to be the slowest step in the overall reaction network.[104,110] Therefore, estimating the kinetics of phenol deoxygenation will be advantageous in understanding the hydrodeoxygenation pathway. Furthermore, combination with DFT studies may also help resolve the debate in literature on the mechanism of direct deoxygenation of phenol. It was also shown before that presence of both Pt and Mo was critical in phenol deoxygenation. Performing kinetic experiments on a series of bimetallic catalysts with different Pt and Mo ratios will shed light on individual roles of each of the metals in the direct deoxygenation pathway.

6.2.2 Interactions between biomass-derived oxygenates

Thermochemical treatments especially pyrolysis of intact biomass typically produce a soup of compounds which are chemically different both in terms of the oxygen functional group and the carbon backbone.[73] These compounds may not only have different overall activity for the given set of catalyst and reaction conditions, but also undergo positive or negative interactions. The interaction between each of these compounds will affect the efficacy of the catalytic hydrodeoxygenation and would need to be taken into account before reactor design. As discussed before, the objective of this work was to understand the fundamental workings of the catalytic hydrodeoxygenation by feeding single model compounds. Therefore, the next logical step to bridge the gap would be to feed two or more of these distinct model compounds and discern the effect of interactions, if any. As a preliminary study, furfural and acetic acid were co-fed over the 5%Pt/MWCNT catalyst to show that although the conversion of furfural was similar, acetic acid was recovered as-is. This may suggest competitive adsorption between furfural and acetic acid over the monometallic Pt catalyst.

Table 6.1 Furfural and acetic acid catalytic hydrodeoxygenation over 5%Pt/MWCNT catalyst at a temperature of 284°C and 1.9 MPa hydrogen pressure

Furfural feed partial pressure/ MPa	Acetic acid feed partial pressure/ MPa	Furfural conversion/ %	Acetic acid conversion/ %
0.02	0	17	-
0	0.05	-	4.1
0.02	0.05	15	0

Below given is the comparison of site-time yield over 5%Pt/MWCNT catalysts between three model compounds, when they were fed individually: dihydroeugenol, furfural and acetic acid. Data presented here was collected in a conversion range of 10-15%, which represented aryl ether, aldehyde and carboxylic acid transformations respectively.

Table 6.2 Overall STYPt over 5%Pt/MWCNT catalyst extrapolated to conditions at a hydrogen pressure of 1.9 MPa, 0.01 MPa of model compound and a temperature of 300°C.

Model compound	Oxygen functional group	Overall $STY_{Pt}/10^{-1}$ s^{-1}
Dihydroeugenol	aryl ether	1.05
Furfural	aldehyde	4.40
Acetic acid	carboxylic acid	0.41

In case of dihydroeugenol, the theoretical carbon yield of liquid product achievable was only 90%, as the methoxy group was lost either as methanol or methane. A catalytic system that is able to re-attach methanol in form of a methyl substituent will be beneficial in terms of increasing the theoretical carbon yield to 100%. This idea can be further expanded in to utilizing the light C_2 and C_3 compounds produced during pyrolysis of cellulose or biomass. Based on preliminary studies and a literature review, it is considered important that the light oxygenate not undergo complete deoxygenation. For example, over the monometallic Mo catalyst, methanol was preserved as is to a large extent, which resulted in higher proportion of methyl-substituted aromatic rings in the product distribution. Zeolites such as ZSM-5, as well as metal oxides have been reported

to have the capability to adding an alkyl-substituent to the aromatic ring from methoxy-substituted benzene or methanol as a co-feed.[120–122]

6.2.3 Pt-based bifunctional catalysts

Literature on guaiacol hydrodeoxygenation over Pt-based catalyst suggests a higher proportion of ring-saturated products compared to results presented in Chapter 5 at 0.1 MPa hydrogen pressure.[107,123] One of the possible explanations for this behavior is the higher proportion of monometallic Pt particles present over Pt/Al_2O_3 compared to the bimetallic Pt-Mo catalyst tested in this study. Preliminary results in this study suggest that Pt is not only responsible for hydrogen activation but also for undesirable aromatic ring hydrogenation. However, some DFT reports suggest that alloyed Pt particle may have a lower rate of aromatic ring hydrogenation because of absence of preferred Pt configurations for benzene adsorption.[124,125] Alloyed Pt catalysts therefore present an exciting opportunity to further maximize the aromatic hydrocarbon yield. Other oxophilic promoters such as Re, Sn, Nb may alter the catalyst structure and thus have an effect on efficacy of selective hydrodeoxygenation. Furthermore, C-O bond scission activity of the catalyst could also correlated to the oxophilicity of the promoter metal.

6.2.4 Carbide-based catalysts

Molybdenum carbide systems have been reported to have hydrodeoxygenation selectivity from biomass-derived oxygenates.[81,126] However, these catalytic systems were reported to deactivate possibly due to buildup of oxygen species. In this preliminary work, it was hypothesized that adding Pt to the catalyst would assist in oxygen removal from catalytic

surface as water by hydrogen activation. Experiments were also performed at 0.1 and 2.4 MPa hydrogen pressure to compare the results with the bimetallic Pt-Mo catalyst. Initial results suggest Pt/Mo_2C was able to operate at a stable conversion at 2.4 MPa hydrogen pressure, with comparable yields of propylcyclohexane as the hydrocarbon product.

Table 6.3 Comparison of Pt/Mo_2C and 5%Pt-2.5%Mo catalysts at 99.99% conversion at a temperature of 300°C and a hydrogen pressure of 2.4 MPa

Parameter	$1.5\%Pt/Mo_2C$	5%Pt-2.5%Mo /MWCNT
Conversion/ %	99.99	99.99
Propylcyclohexane/ %	94.4	97.8
Propylbenzene/ %	0.3	0.2
Methyl cyclopentane/ %	1.1	0.5

At a lower pressure of 0.1 MPa, continuous deactivation was observed in agreement with other studies. Furthermore, comparing the day to day selectivity of propylbenzene in a similar conversion range suggests that sites responsible for hydrodeoxygenation deactivate as the catalyst is aged. This demands for a need to optimize Pt and Mo_2C sites as well study intermediate hydrogen pressures.

BIBLIOGRAPHY

BIBLIOGRAPHY

1. United Nations General Assembly Declares 2014-2024 Decade of Sustainable Energy for All. at <http://www.un.org/News/Press/docs/2012/ga11333.doc.htm>
2. U.S. Energy Information Administration. Annual Energy Outlook 2014. (2014).
3. Shafiee, S. & Topal, E. When will fossil fuel reserves be diminished? *Energy Policy* **37,** 181–189 (2009).
4. Environmental Challenges in Energy, Carbon Dioxide, Air, Water and Land Use. *OpenStax-CNX* at <http://cnx.org/content/m41725/latest/?collection=col11325>
5. Tsao, J., Lewis, N. & Crabtree, G. Solar FAQs. *US Department of Energy* (2006).
6. Energy Flow. at <https://flowcharts.llnl.gov/>
7. Fischer, M., Werber, M. & Schwartz, P. V. Batteries: Higher energy density than gasoline? *Energy Policy* **37,** 2639–2641 (2009).
8. Speight, J. G. *The Chemistry and Technology of Petroleum, Fifth Edition*. (CRC Press, 2014).
9. Zhang, Q., Chang, J., Wang, T. & Xu, Y. Review of biomass pyrolysis oil properties and upgrading research. *Energy Conversion and Management* **48,** 87–92 (2007).
10. Huber, G. W., Iborra, S. & Corma, A. Synthesis of Transportation Fuels from Biomass: Chemistry, Catalysts, and Engineering. *Chem. Rev.* **106,** 4044–4098 (2006).
11. Cho, J., Davis, J. M. & Huber, G. W. The Intrinsic Kinetics and Heats of Reactions for Cellulose Pyrolysis and Char Formation. *ChemSusChem* **3,** 1162–1165 (2010).
12. Feldman, D. Wood—chemistry, ultrastructure, reactions, by D. Fengel and G. Wegener, Walter de Gruyter, Berlin and New York, 1984, 613 pp. Price: 245 DM. *J. Polym. Sci. B Polym. Lett. Ed.* **23,** 601–602 (1985).

13. Sosa-Arnao, J. H. & Nebra, S. A. Bagasse Dryer Role in the Energy Recovery of Water Tube Boilers. *Drying Technology* **27,** 587–594 (2009).
14. Serrano-Ruiz, J. C., West, R. M. & Dumesic, J. A. Catalytic Conversion of Renewable Biomass Resources to Fuels and Chemicals. *Annual Review of Chemical and Biomolecular Engineering* **1,** 79–100 (2010).
15. Chia, M. *et al.* Bimetallic RhRe/C catalysts for the production of biomass-derived chemicals. *Journal of Catalysis* **308,** 226–236 (2013).
16. Davda, R. R., Shabaker, J. W., Huber, G. W., Cortright, R. D. & Dumesic, J. A. A review of catalytic issues and process conditions for renewable hydrogen and alkanes by aqueous-phase reforming of oxygenated hydrocarbons over supported metal catalysts. *Applied Catalysis B: Environmental* **56,** 171–186 (2005).
17. Huber, G. W., Cortright, R. D. & Dumesic, J. A. Renewable Alkanes by Aqueous-Phase Reforming of Biomass-Derived Oxygenates. *Angewandte Chemie International Edition* **43,** 1549–1551 (2004).
18. Parsell, T. H. *et al.* Cleavage and hydrodeoxygenation (HDO) of C–O bonds relevant to lignin conversion using Pd/Zn synergistic catalysis. *Chemical Science* **4,** 806 (2013).
19. Mohan, D., Pittman, Charles U. & Steele, P. H. Pyrolysis of Wood/Biomass for Bio-oil: A Critical Review. *Energy Fuels* **20,** 848–889 (2006).
20. Elliott, D. C. Historical Developments in Hydroprocessing Bio-oils. *Energy Fuels* **21,** 1792–1815 (2007).
21. Elliott, D. C., Oasmaa, A., Preto, F., Meier, D. & Bridgwater, A. V. Results of the IEA Round Robin on Viscosity and Stability of Fast Pyrolysis Bio-oils. *Energy Fuels* **26,** 3769–3776 (2012).
22. Agrawal, R. & Singh, N. R. Synergistic routes to liquid fuel for a petroleum-deprived future. *AIChE J.* **55,** 1898–1905 (2009).
23. Agrawal, R. & Mallapragada, D. S. Chemical engineering in a solar energy-driven sustainable future. *AIChE J.* **56,** 2762–2768 (2010).

24. Agrawal, R., Agrawal, M. & Singh, N. R. Process for producing liquid hydrocarbon by pyrolysis of biomass in presence of hydrogen from a carbon-free energy source. (2012).
25. Agrawal, R. & Singh, N. R. Producing liquid hydrocarbons from biomass via hydropyrolysis of biomass with a gaseous exhaust stream comprising CO2, CO, H2, and water formed from one of gasification and reforming of carbon containing moiety (CCM) such as natural gas; biofuels. (2012).
26. Agrawal, R. & Singh, N. R. Solar Energy to Biofuels. *Annual Review of Chemical and Biomolecular Engineering* **1,** 343–364 (2010).
27. Girgis, M. J. & Gates, B. C. Reactivities, reaction networks, and kinetics in high-pressure catalytic hydroprocessing. *Ind. Eng. Chem. Res.* **30,** 2021–2058 (1991).
28. Singh, N. R., Mallapragada, D. S., Agrawal, R. & Tyner, W. E. Economic analysis of novel synergistic biofuel (H2Bioil) processes. *Biomass Conv. Bioref.* **2,** 141–148 (2012).
29. Cortright, R. D., Davda, R. R. & Dumesic, J. A. Hydrogen from catalytic reforming of biomass-derived hydrocarbons in liquid water. *Nature* **418,** 964–967 (2002).
30. Lédé, J. Cellulose pyrolysis kinetics: An historical review on the existence and role of intermediate active cellulose. *Journal of Analytical and Applied Pyrolysis* **94,** 17–32 (2012).
31. Sara L. Yohe. High-pressure vapor-phase catalytic hydrodeoxygenation of lignin-derived compounds to hydrocarbons on bimetallic catalysts in the range of 0.2-2.4MPa. (2013).
32. Agrawal, R., Offutt, M. & Ramage, M. P. Hydrogen economy - an opportunity for chemical engineers? *AIChE J.* **51,** 1582–1589 (2005).
33. Ratnasamy, C. & Wagner, J. P. Water Gas Shift Catalysis. *Catalysis Reviews* **51,** 325–440 (2009).
34. Rabe, S., Nachtegaal, M., Ulrich, T. & Vogel, F. Towards Understanding the Catalytic Reforming of Biomass in Supercritical Water. *Angewandte Chemie International Edition* **49,** 6434–6437 (2010).

35. Kunkes, E. L., Soares, R. R., Simonetti, D. A. & Dumesic, J. A. An integrated catalytic approach for the production of hydrogen by glycerol reforming coupled with water-gas shift. *Applied Catalysis B: Environmental* **90,** 693–698 (2009).
36. Phatak, A. A. *et al.* Kinetics of the water–gas shift reaction on Pt catalysts supported on alumina and ceria. *Catalysis Today* **123,** 224–234 (2007).
37. Shabaker, J. W., Huber, G. W., Davda, R. R., Cortright, R. D. & Dumesic, J. A. Aqueous-Phase Reforming of Ethylene Glycol Over Supported Platinum Catalysts. *Catalysis Letters* **88,** 1–8 (2003).
38. Desai, S. & Neurock, M. A first principles analysis of CO oxidation over Pt and Pt66.7%Ru33.3% (111) surfaces. *Electrochimica Acta* **48,** 3759–3773 (2003).
39. He, R., Davda, R. R. & Dumesic, J. A. In Situ ATR-IR Spectroscopic and Reaction Kinetics Studies of Water−Gas Shift and Methanol Reforming on Pt/Al2O3 Catalysts in Vapor and Liquid Phases. *J. Phys. Chem. B* **109,** 2810–2820 (2005).
40. Dietrich, P. J. *et al.* Aqueous Phase Glycerol Reforming by PtMo Bimetallic Nano-Particle Catalyst: Product Selectivity and Structural Characterization. *Top Catal* **55,** 53–69 (2012).
41. Koros, R. M. & Nowak, E. J. A diagnostic test of the kinetic regime in a packed bed reactor. *Chemical Engineering Science* **22,** 470 (1967).
42. Kim, S. M. *et al.* Evolution in Catalyst Morphology Leads to Carbon Nanotube Growth Termination. *J. Phys. Chem. Lett.* **1,** 918–922 (2010).
43. Miller, J. T. *et al.* The effect of gold particle size on AuAu bond length and reactivity toward oxygen in supported catalysts. *Journal of Catalysis* **240,** 222–234 (2006).
44. Pazmiño, J. H., Miller, J. T., Mulla, S. S., Nicholas Delgass, W. & Ribeiro, F. H. Kinetic studies of the stability of Pt for NO oxidation: Effect of sulfur and long-term aging. *Journal of Catalysis* **282,** 13–24 (2011).
45. Bollmann, L. *et al.* Effect of Zn addition on the water–gas shift reaction over supported palladium catalysts. *Journal of Catalysis* **257,** 43–54 (2008).
46. Pazmiño, J. H. *et al.* Metallic Pt as active sites for the water–gas shift reaction on alkali-promoted supported catalysts. *Journal of Catalysis* **286,** 279–286 (2012).

47. Janssens, T. V. W. *et al.* Insights into the reactivity of supported Au nanoparticles: combining theory and experiments. *Top Catal* **44,** 15–26 (2007).
48. Overbury, S. H., Schwartz, V., Mullins, D. R., Yan, W. & Dai, S. Evaluation of the Au size effect: CO oxidation catalyzed by Au/TiO2. *Journal of Catalysis* **241,** 56–65 (2006).
49. Miller, J. T., Schreier, M., Kropf, A. J. & Regalbuto, J. R. A fundamental study of platinum tetraammine impregnation of silica: 2. The effect of method of preparation, loading, and calcination temperature on (reduced) particle size. *Journal of Catalysis* **225,** 203–212 (2004).
50. Madon, R. J. & Boudart, M. Experimental criterion for the absence of artifacts in the measurement of rates of heterogeneous catalytic reactions. *Ind. Eng. Chem. Fund.* **21,** 438–447 (1982).
51. McIntyre, B. J., Salmeron, M. & Somorjai, G. A. An in situ STM determination of a kinetic pathway for the coadsorbate-induced compression of sulfur by CO on Pt(111). *Surface Science* **323,** 189–197 (1995).
52. Streber, R. *et al.* Site blocking and CO/sulfur site exchange processes on stepped Pt surfaces. *J. Phys.: Condens. Matter* **21,** 134018 (2009).
53. Few transportation fuels surpass the energy densities of gasoline and diesel - Today in Energy - U.S. Energy Information Administration (EIA). at <http://www.eia.gov/todayinenergy/detail.cfm?id=9991>
54. Czernik, S. & Bridgwater, A. V. Overview of Applications of Biomass Fast Pyrolysis Oil. *Energy Fuels* **18,** 590–598 (2004).
55. Bridgwater, A. V. Review of fast pyrolysis of biomass and product upgrading. *Biomass and Bioenergy* **38,** 68–94 (2012).
56. Kim, T.-S. *et al.* The effect of storage duration on bio-oil properties. *Journal of Analytical and Applied Pyrolysis* **95,** 118–125 (2012).
57. Patwardhan, P. R., Dalluge, D. L., Shanks, B. H. & Brown, R. C. Distinguishing primary and secondary reactions of cellulose pyrolysis. *Bioresource Technology* **102,** 5265–5269 (2011).

58. Mettler, M. S., Vlachos, D. G. & Dauenhauer, P. J. Top ten fundamental challenges of biomass pyrolysis for biofuels. *Energy & Environmental Science* **5,** 7797 (2012).
59. Venkatakrishnan, V. K. *et al.* High-pressure fast-pyrolysis, fast-hydropyrolysis and catalytic hydrodeoxygenation of cellulose: production of liquid fuel from biomass. *Green Chemistry* **16,** 792 (2014).
60. Cyprès, R. & Furfari, S. Direct post-cracking of volatiles from coal hydropyrolysis: 1. Influence of post-cracking temperature. *Fuel* **64,** 33–39 (1985).
61. Vinueza, N. R., Gallardo, V. A., Klimek, J. F., Carpita, N. C. & Kenttämaa, H. I. Analysis of carbohydrates by atmospheric pressure chloride anion attachment tandem mass spectrometry. *Fuel* **105,** 235–246 (2013).
62. Hurt, M. R. *et al.* On-Line Mass Spectrometric Methods for the Determination of the Primary Products of Fast Pyrolysis of Carbohydrates and for Their Gas-Phase Manipulation. *Anal. Chem.* **85,** 10927–10934 (2013).
63. Wang, Z., Zhou, S., Pecha, B., Westerhof, R. J. M. & Garcia-Perez, M. Effect of Pyrolysis Temperature and Sulfuric Acid During the Fast Pyrolysis of Cellulose and Douglas Fir in an Atmospheric Pressure Wire Mesh Reactor. *Energy Fuels* (2014). doi:10.1021/ef500999z
64. Tessini, C. *et al.* High performance thin layer chromatography determination of cellobiosan and levoglucosan in bio-oil obtained by fast pyrolysis of sawdust. *Journal of Chromatography A* **1218,** 3811–3815 (2011).
65. Pouwels, A. D., Eijkel, G. B., Arisz, P. W. & Boon, J. J. Evidence for oligomers in pyrolysates of microcrystalline cellulose. *Journal of Analytical and Applied Pyrolysis* **15,** 71–84 (1989).
66. Piskorz, J., Majerski, P., Radlein, D., Vladars-Usas, A. & Scott, D. S. Flash pyrolysis of cellulose for production of anhydro-oligomers. *Journal of Analytical and Applied Pyrolysis* **56,** 145–166 (2000).
67. Radlein, D. S. T. A. G., Grinshpun, A., Piskorz, J. & Scott, D. S. On the presence of anhydro-oligosaccharides in the sirups from the fast pyrolysis of cellulose. *Journal of Analytical and Applied Pyrolysis* **12,** 39–49 (1987).

68. Teixeira, A. R. *et al.* Aerosol generation by reactive boiling ejection of molten cellulose. *Energy & Environmental Science* **4,** 4306 (2011).
69. Patwardhan, P. R., Satrio, J. A., Brown, R. C. & Shanks, B. H. Product distribution from fast pyrolysis of glucose-based carbohydrates. *Journal of Analytical and Applied Pyrolysis* **86,** 323–330 (2009).
70. Mosier, N. *et al.* Features of promising technologies for pretreatment of lignocellulosic biomass. *Bioresource Technology* **96,** 673–686 (2005).
71. Lange, J.-P., van der Heide, E., van Buijtenen, J. & Price, R. Furfural—A Promising Platform for Lignocellulosic Biofuels. *ChemSusChem* **5,** 150–166 (2012).
72. Binder, J. B. & Raines, R. T. Simple Chemical Transformation of Lignocellulosic Biomass into Furans for Fuels and Chemicals. *J. Am. Chem. Soc.* **131,** 1979–1985 (2009).
73. Elliott, D. C. Transportation fuels from biomass via fast pyrolysis and hydroprocessing. *WENE* **2,** 525–533 (2013).
74. Asadieraghi, M., Wan Daud, W. M. A. & Abbas, H. F. Model compound approach to design process and select catalysts for in-situ bio-oil upgrading. *Renewable and Sustainable Energy Reviews* **36,** 286–303 (2014).
75. Furimsky, E. Catalytic hydrodeoxygenation. *Applied Catalysis A: General* **199,** 147–190 (2000).
76. Resasco, D. E. What Should We Demand from the Catalysts Responsible for Upgrading Biomass Pyrolysis Oil? *J. Phys. Chem. Lett.* **2,** 2294–2295 (2011).
77. Sitthisa, S. & Resasco, D. E. Hydrodeoxygenation of Furfural Over Supported Metal Catalysts: A Comparative Study of Cu, Pd and Ni. *Catal Lett* **141,** 784–791 (2011).
78. Sitthisa, S., Sooknoi, T., Ma, Y., Balbuena, P. B. & Resasco, D. E. Kinetics and mechanism of hydrogenation of furfural on Cu/SiO2 catalysts. *Journal of Catalysis* **277,** 1–13 (2011).
79. Sitthisa, S., An, W. & Resasco, D. E. Selective conversion of furfural to methylfuran over silica-supported NiFe bimetallic catalysts. *Journal of Catalysis* **284,** 90–101 (2011).

80. Xiong, K., Lee, W.-S., Bhan, A. & Chen, J. G. Molybdenum Carbide as a Highly Selective Deoxygenation Catalyst for Converting Furfural to 2-Methylfuran. *ChemSusChem* n/a–n/a (2014). doi:10.1002/cssc.201402033
81. Lee, W.-S., Wang, Z., Zheng, W., Vlachos, D. G. & Bhan, A. Vapor phase hydrodeoxygenation of furfural to 2-methylfuran on molybdenum carbide catalysts. *Catal. Sci. Technol.* (2014). doi:10.1039/C4CY00286E
82. McManus, J. R. & Vohs, J. M. Deoxygenation of glycolaldehyde and furfural on Mo2C/Mo(100). *Surface Science* **630,** 16–21 (2014).
83. Pushkarev, V. V., Musselwhite, N., An, K., Alayoglu, S. & Somorjai, G. A. High Structure Sensitivity of Vapor-Phase Furfural Decarbonylation/Hydrogenation Reaction Network as a Function of Size and Shape of Pt Nanoparticles. *Nano Lett.* **12,** 5196–5201 (2012).
84. Yu, W. *et al.* One-step hydrogenation–esterification of furfural and acetic acid over bifunctional Pd catalysts for bio-oil upgrading. *Bioresource Technology* **102,** 8241–8246 (2011).
85. Prasomsri, T., Nimmanwudipong, T. & Román-Leshkov, Y. Effective hydrodeoxygenation of biomass-derived oxygenates into unsaturated hydrocarbons by MoO3 using low H2 pressures. *Energy Environ. Sci.* **6,** 1732–1738 (2013).
86. Prasomsri, T., Shetty, M., Murugappan, K. & Román-Leshkov, Y. Insights into the catalytic activity and surface modification of MoO3 during the hydrodeoxygenation of lignin-derived model compounds into aromatic hydrocarbons under low hydrogen pressures. *Energy & Environmental Science* (2014). doi:10.1039/c4ee00890a
87. Dietrich, P. J. *et al.* Aqueous Phase Glycerol Reforming with Pt and PtMo Bimetallic Nanoparticle Catalysts: The Role of the Mo Promoter. *Top Catal* **56,** 1814–1828 (2013).
88. Dietrich, P. J. *et al.* Structural and catalytic differences in the effect of Co and Mo as promoters for Pt-based aqueous phase reforming catalysts. *Applied Catalysis B: Environmental* **156–157,** 236–248 (2014).

89. Bates, S. A., Delgass, W. N., Ribeiro, F. H., Miller, J. T. & Gounder, R. Methods for NH3 titration of Brønsted acid sites in Cu-zeolites that catalyze the selective catalytic reduction of NOx with NH3. *Journal of Catalysis* **312,** 26–36 (2014).
90. Neophytides, S. G., Zafeiratos, S. H. & Jaksic, M. M. Selective Interactive Grafting of Composite Bifunctional Electrocatalysts for Simultaneous Anodic Hydrogen and CO Oxidation I. Concepts and Embodiment of Novel-Type Composite Catalysts. *J. Electrochem. Soc.* **150,** E512–E526 (2003).
91. Grim, S. O. & Matienzo, L. J. X-ray photoelectron spectroscopy of inorganic and organometallic compounds of molybdenum. *Inorg. Chem.* **14,** 1014–1018 (1975).
92. deVries, J. E., Yao, H. C., Baird, R. J. & Gandhi, H. S. Characterization of molybdenum-platinum catalysts supported on γ-alumina by X-ray photoelectron spectroscopy. *Journal of Catalysis* **84,** 8–14 (1983).
93. Sitthisa, S. *et al.* Conversion of furfural and 2-methylpentanal on Pd/SiO2 and Pd–Cu/SiO2 catalysts. *Journal of Catalysis* **280,** 17–27 (2011).
94. Humphreys, J. M. & Chapple, C. Rewriting the lignin roadmap. *Current Opinion in Plant Biology* **5,** 224–229 (2002).
95. Agrawal, R., Singh, N. R., Ribeiro, F. H. & Delgass, W. N. Sustainable fuel for the transportation sector. *PNAS* **104,** 4828–4833 (2007).
96. McDonough, T. J. The chemistry of organosolv delignification. (1992). at <https://smartech.gatech.edu/handle/1853/2069>
97. Xu, W., Miller, S. J., Agrawal, P. K. & Jones, C. W. Depolymerization and Hydrodeoxygenation of Switchgrass Lignin with Formic Acid. *ChemSusChem* **5,** 667–675 (2012).
98. Pandey, M. P. & Kim, C. S. Lignin Depolymerization and Conversion: A Review of Thermochemical Methods. *Chem. Eng. Technol.* **34,** 29–41 (2011).
99. Zakzeski, J., Bruijnincx, P. C. A., Jongerius, A. L. & Weckhuysen, B. M. The Catalytic Valorization of Lignin for the Production of Renewable Chemicals. *Chem. Rev.* **110,** 3552–3599 (2010).
100. Hicks, J. C. Advances in C–O Bond Transformations in Lignin-Derived Compounds for Biofuels Production. *J. Phys. Chem. Lett.* **2,** 2280–2287 (2011).

101. Bu, Q. *et al.* A review of catalytic hydrodeoxygenation of lignin-derived phenols from biomass pyrolysis. *Bioresource Technology* **124,** 470–477 (2012).
102. Wang, H., Male, J. & Wang, Y. Recent Advances in Hydrotreating of Pyrolysis Bio-Oil and Its Oxygen-Containing Model Compounds. *ACS Catal.* **3,** 1047–1070 (2013).
103. Saidi, M. *et al.* Upgrading of lignin-derived bio-oils by catalytic hydrodeoxygenation. *Energy & Environmental Science* **7,** 103 (2014).
104. Zhao, C. & Lercher, J. A. Selective Hydrodeoxygenation of Lignin-Derived Phenolic Monomers and Dimers to Cycloalkanes on Pd/C and HZSM-5 Catalysts. *ChemCatChem* **4,** 64–68 (2012).
105. Zhao, C., He, J., Lemonidou, A. A., Li, X. & Lercher, J. A. Aqueous-phase hydrodeoxygenation of bio-derived phenols to cycloalkanes. *Journal of Catalysis* **280,** 8–16 (2011).
106. Zhu, X., Lobban, L. L., Mallinson, R. G. & Resasco, D. E. Bifunctional transalkylation and hydrodeoxygenation of anisole over a Pt/HBeta catalyst. *Journal of Catalysis* **281,** 21–29 (2011).
107. Foster, A. J., Do, P. T. M. & Lobo, R. F. The Synergy of the Support Acid Function and the Metal Function in the Catalytic Hydrodeoxygenation of m-Cresol. *Top Catal* **55,** 118–128 (2012).
108. Mortensen, P. M., Grunwaldt, J.-D., Jensen, P. A. & Jensen, A. D. Screening of Catalysts for Hydrodeoxygenation of Phenol as a Model Compound for Bio-oil. *ACS Catal.* **3,** 1774–1785 (2013).
109. Nie, L. & Resasco, D. E. Kinetics and mechanism of m-cresol hydrodeoxygenation on a Pt/SiO2 catalyst. *Journal of Catalysis* **317,** 22–29 (2014).
110. He, J., Zhao, C. & Lercher, J. A. Impact of solvent for individual steps of phenol hydrodeoxygenation with Pd/C and HZSM-5 as catalysts. *Journal of Catalysis* **309,** 362–375 (2014).
111. Ausavasukhi, A., Huang, Y., To, A. T., Sooknoi, T. & Resasco, D. E. Hydrodeoxygenation of m-cresol over gallium-modified beta zeolite catalysts. *Journal of Catalysis* **290,** 90–100 (2012).

112. Gualda, G. & Kasztelan, S. Initial Deactivation of Residue Hydrodemetallization Catalysts. *Journal of Catalysis* **161,** 319–337 (1996).
113. Weisz, P. B. & Prater, C. D. in *Advances in Catalysis* (ed. W.G. Frankenburg, V. I. K. and E. K. R.) **Volume 6,** 143–196 (Academic Press, 1954).
114. Vannice, M. A. in *Kinetics of Catalytic Reactions* 38–86 (Springer US, 2005). at <http://link.springer.com/chapter/10.1007/978-0-387-25972-7_4>
115. Nimmanwudipong, T., Runnebaum, R. C., Block, D. E. & Gates, B. C. Catalytic Conversion of Guaiacol Catalyzed by Platinum Supported on Alumina: Reaction Network Including Hydrodeoxygenation Reactions. *Energy Fuels* **25,** 3417–3427 (2011).
116. Korbach, P. F. & Stewart, W. E. Kinetic and Equilibrium Studies of Benzene Hydrogenation in a Batch Recycle Reactor. *Ind. Eng. Chem. Fund.* **3,** 24–27 (1964).
117. Prigogine, I., Outer, P. & Herbo, C. Affinity and Reaction Rate Close to Equilibrium. *J. Phys. Chem.* **52,** 321–331 (1948).
118. Chou, P. & Vannice, M. A. Benzene hydrogenation over supported and unsupported palladium: I. Kinetic behavior. *Journal of Catalysis* **107,** 129–139 (1987).
119. Lin, S. D. & Vannice, M. A. Hydrogenation of Aromatic Hydrocarbons over Supported Pt Catalysts .II. Toluene Hydrogenation. *Journal of Catalysis* **143,** 554–562 (1993).
120. Yashima, T., Sato, K., Hayasaka, T. & Hara, N. Alkylation on synthetic zeolites: III. Alkylation of toluene with methanol and formaldehyde on alkali cation exchanged zeolites. *Journal of Catalysis* **26,** 303–312 (1972).
121. Renavd, M., Chantal, P. D. & Kaliaguine, S. Anisole production by alkylation of phenol over ZSM5. *Can. J. Chem. Eng.* **64,** 787–791 (1986).
122. Sato, S., Koizumi, K. & Nozaki, F. Ortho-Selective Methylation of Phenol Catalyzed by CeO2-MgO Prepared by Citrate Process. *Journal of Catalysis* **178,** 264–274 (1998).
123. Do, P. T. M., Foster, A. J., Chen, J. & Lobo, R. F. Bimetallic effects in the hydrodeoxygenation of meta-cresol on γ-Al2O3 supported Pt–Ni and Pt–Co catalysts. *Green Chemistry* **14,** 1388 (2012).

124. Saeys, M., Reyniers, M.-F., Marin, G. B. & Neurock, M. Density Functional Study of Benzene Adsorption on Pt(111). *J. Phys. Chem. B* **106,** 7489–7498 (2002).
125. Bratlie, K. M., Lee, H., Komvopoulos, K., Yang, P. & Somorjai, G. A. Platinum Nanoparticle Shape Effects on Benzene Hydrogenation Selectivity. *Nano Lett.* **7,** 3097–3101 (2007).
126. Han, J., Duan, J., Chen, P., Lou, H. & Zheng, X. Molybdenum Carbide-Catalyzed Conversion of Renewable Oils into Diesel-like Hydrocarbons. *Advanced Synthesis & Catalysis* **353,** 2577–2583 (2011).

APPENDICES

Appendix A Liquid phase water-gas shift reaction

Transmission electron microscopy

TEM measurements were carried out over fresh and used Pt and Pt-Mo catalysts supported on norit-carbon as well as Pt/C catalyst after reduction and CO activation. The average particle size for used catalyst is typically lower for the fresh catalyst compared to used catalyst, but it was similar after CO activation.

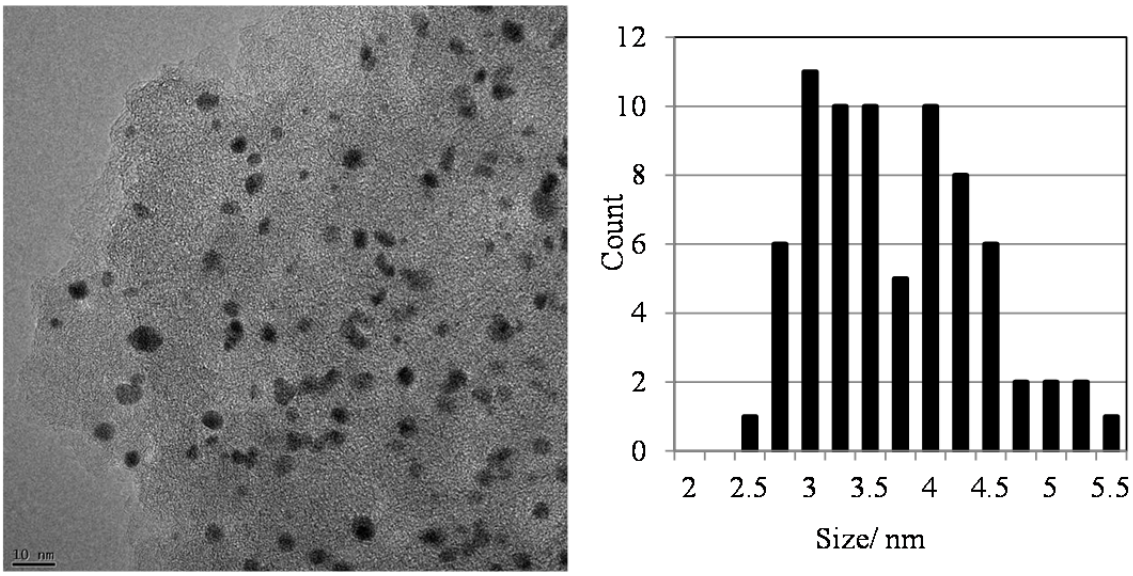

Figure A.1 TEM image and size distribution for used 5%Pt/C catalyst

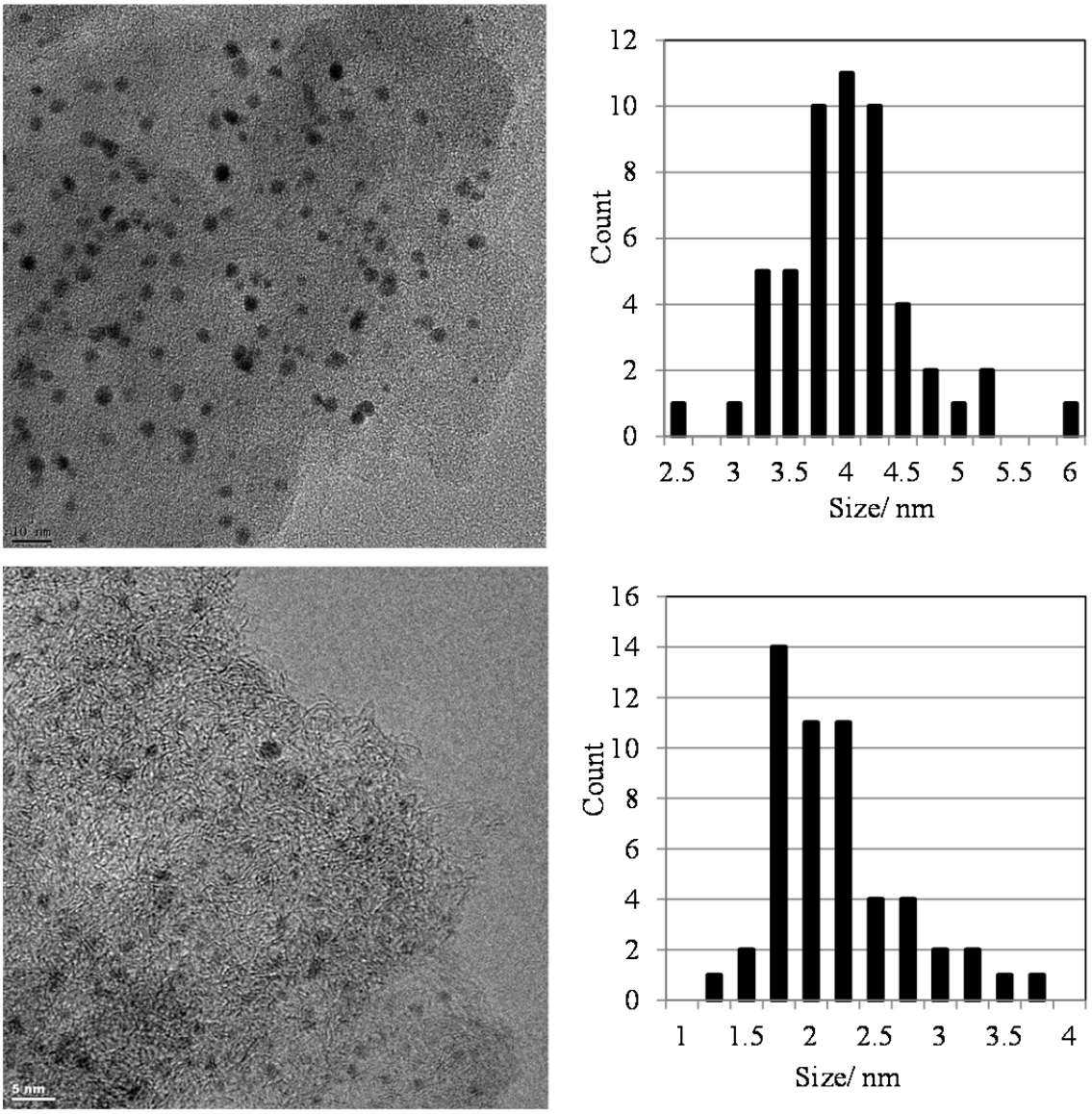

Figure A.2 TEM image and size distribution for 5%Pt/C (after reduction and CO activation) and Fresh 5%Pt-Mo/C

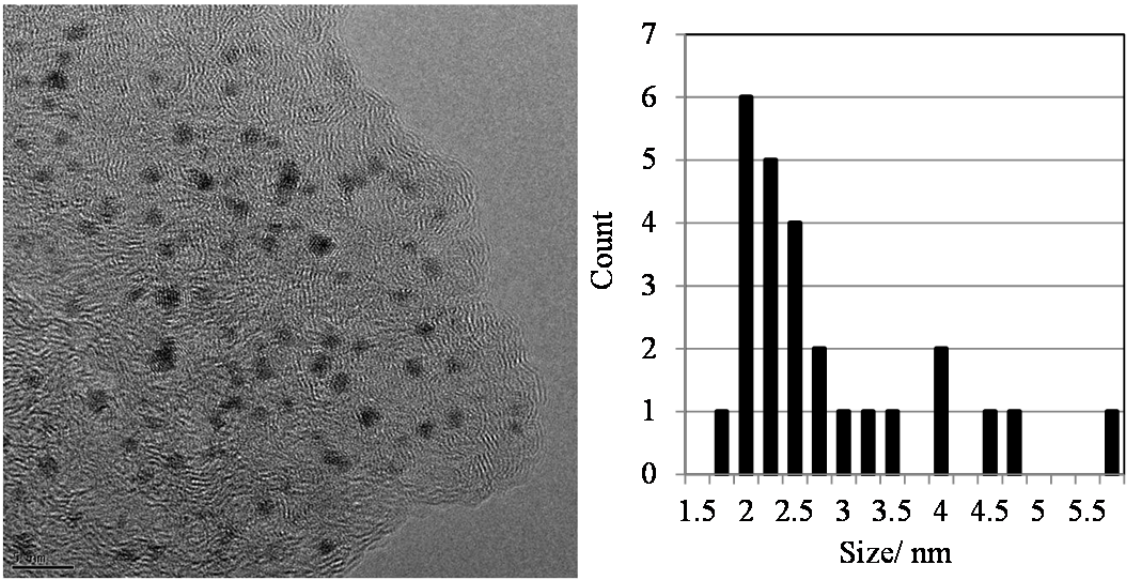

Figure A.3 TEM image and size distribution for used 5%Pt-Mo/C

Correcting Activation energy for water order

Modeling the rate as a power law

$$r = k_0 e^{-\frac{E_a}{RT}} P_{CO}^a P_{H_2O}^b P_{CO_2}^c P_{H_2}^d$$

$$r = (k_0 P_{CO}^a P_{CO_2}^c P_{H_2}^d) e^{-\frac{E_a}{RT}} P_{H_2O}^b$$

$$r = (\mathrm{c}_1) e^{-\frac{E_a}{RT}} P_{H_2O}^b$$

Expressing P_{H2O} as an exponential function of temperature

$$P_{H_2O} = c_2 e^{m/T}$$

$$P_{H_2O} = c_2 e^{-5/T}$$

$$r = (c_1) e^{-\frac{E_{act}}{RT}} (c_2^b e^{-5b/T})$$

$$r = (c_1 c_2^b) e^{-\frac{E_{act}}{RT} - \frac{5b}{T}}$$

Rate measured is

$$r = k e^{-\frac{E_{app}}{RT}}$$

Therefore,

$$-E_{app} = -E_{act} - 41b$$

$$E_{act} = E_{app} - 41b$$

Appendix B Fast hydropyrolysis in a millisecond residence timescale reactor

Hydropyrolysis reactor pressure profile

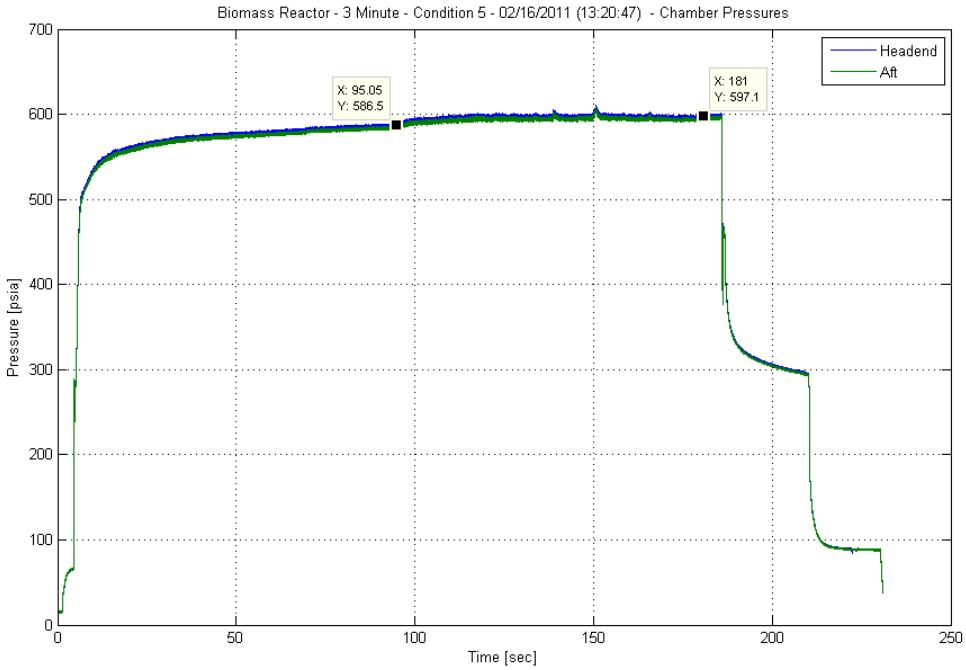

Figure B. 1 Pressure profile at head-end and aft reactor section of the reactor for Run ID RR09

Liquid chromatography mass spectrometry

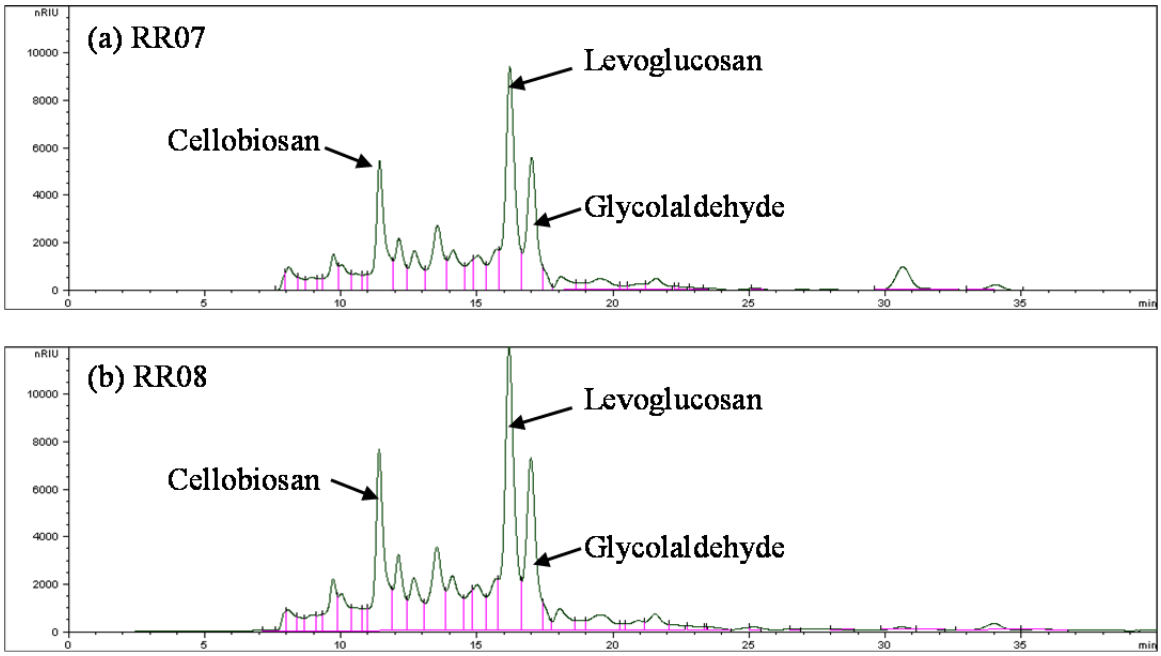

Figure B.2 LC-MS spectra for (a) RR07 and (b) RR08

Appendix C Catalytic hydrodeoxygenation of biomass model compounds

CO chemisorption isotherms

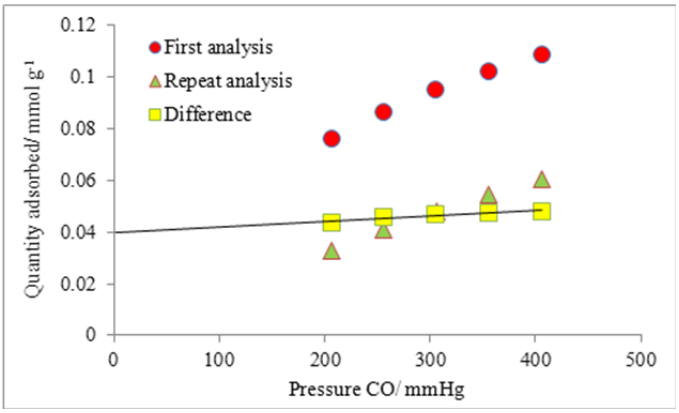

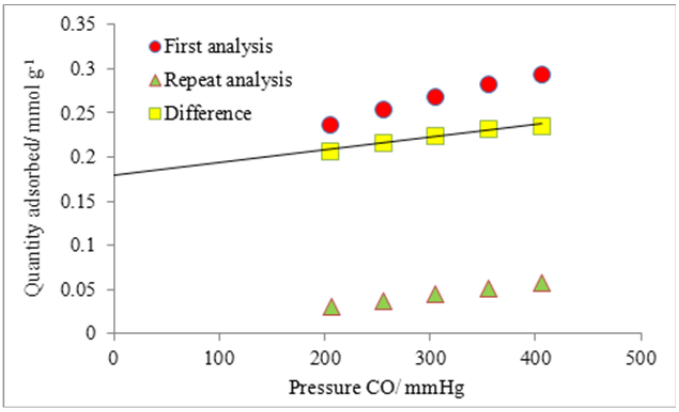

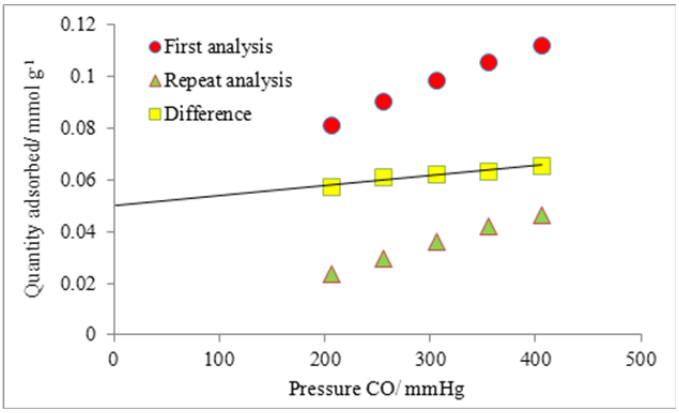

Figure C.1 CO chemisorption isotherms for (a) 5%Pt, (b) 20%Mo, (c) 5%Pt-2.5%Mo

STEM-EELS analysis on a series of Pt-Mo catalysts

Table C.1 Percentage of different particle configurations on the fresh Pt-Mo bimetallic catalysts as identified by STEM-EELS line-scans on at least 20 particles[31]

	Pt Only	Pt-Mo Coordinated	Pt-Mo Alloy	Total
	Percentage of Total Particles / %			
5%Pt-1.2%Mo/MWCNT	50.0	45.0	5.0	100.0
5%Pt-2.5%Mo/MWCNT	22.9	54.3	22.9	100.0
2.5%Pt-2.5%Mo/MWCNT	25.0	60.0	15.0	100.0
2%Pt-4.9%Mo/MWCNT	7.7	61.5	30.8	100.0

Thermodynamic equilibrium ratio estimation

$At\ 300°C, k_{eq} = 0.1\ atm^{-3}$

$$k_{eq} = \frac{P_{propylbenzene}}{P_{propylcyclohexane} \cdot P_{H2}^3}$$

$$\frac{P_{propylbenzene}}{P_{propylcyclohexane}} = k_{eq} \cdot P_{H2}^3$$

Table C.2 Estimated equilibrium ratio of propylbenzene to propylcyclohexane as a function of hydrogen partial pressure at 300°C

Hydrogen partial pressure/ MPa	(Propylbenzene/ Propylcyclohexane)
0.1	10
0.3	1
0.7	0.063
2.4	0.0014

Overall and carbon mass balance

For data provided in Figure 5.2, between 7-15 hours (date of experiment 01/23/2014)

Overall mass balance:

Total DHE fed: 28.76 ml*1.038gm/ml = 29.85 gm

Liquid collected in condenser 1 = 25.84 gm, Liquid collected in condenser 2 = 2.56 gm

Mass balance = 95.14%

Carbon mass balance

DHE feed flow rate, carbon mmol min^{-1} = 0.375

Table C. 3 Product carbon molar flow rate to accomplish carbon balance

Compound	Carbon molar flow rate/ mmol min^{-1}
DHE	0.234
4-propylphenol	0.099
4-propyl-1,2-benzenediol	0.020
3-propylanisole	0.0065
propylbenzene	0.0064
4-propylcyclohexanol	0.003
propylcyclohexane	0.0013
DHE isomer	0.0009
4-propylcyclohexanone	0.0007
propylcyclopentane	0.0006
Other unidentified (~9 peaks)	0.0025
Total	99.75%

Picture of the experimental setup

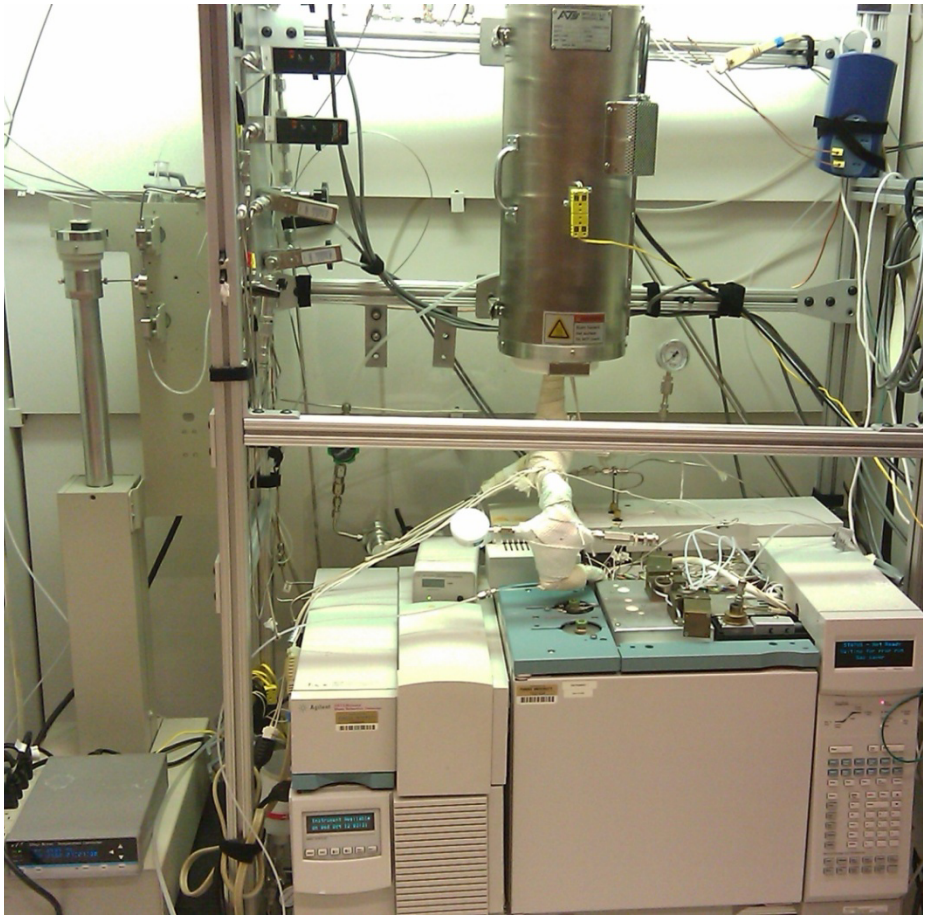

Figure C.2 Picture of the high-pressure, vapor-phase continuous reactor.

Hydrogen order plots

Comparing hydrogen order between different reaction pathways is used to predict the effect of hydrogen pressure on the selectivity of various products.

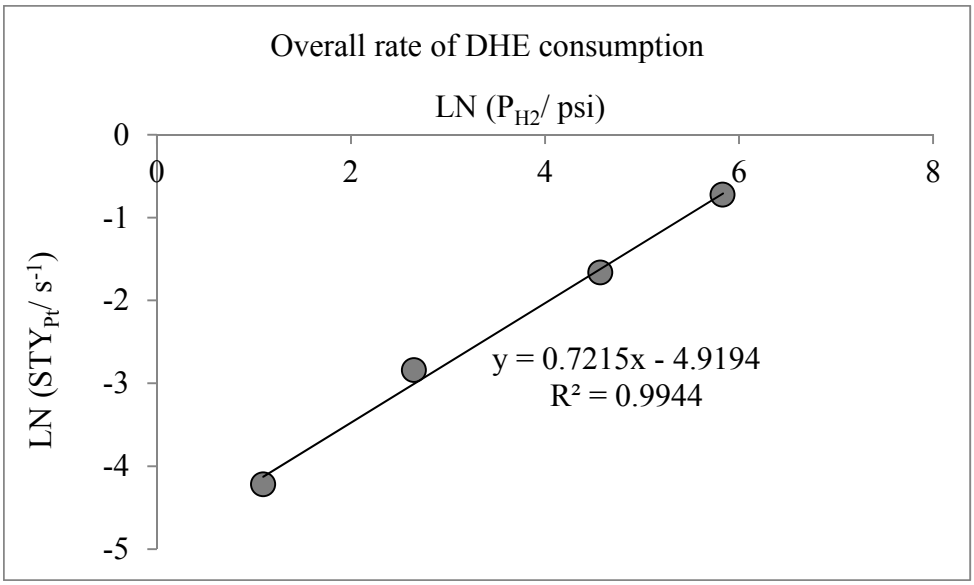

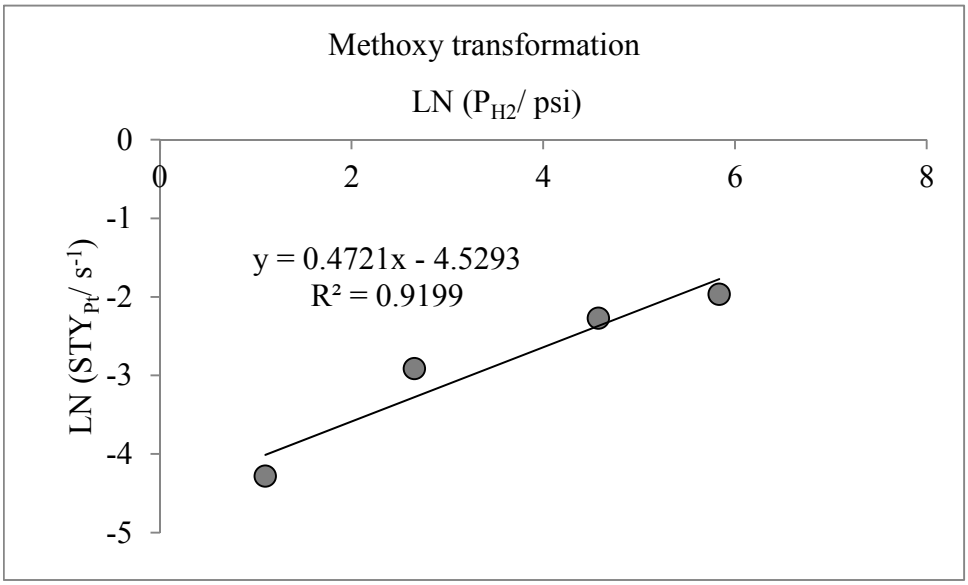

Figure C.3 Hydrogen order plots for overall DHE consumption and methoxy transformation, in a range of 0.02 to 2.4 MPa hydrogen partial pressure over 5%Pt-2.5%Mo and 300°C

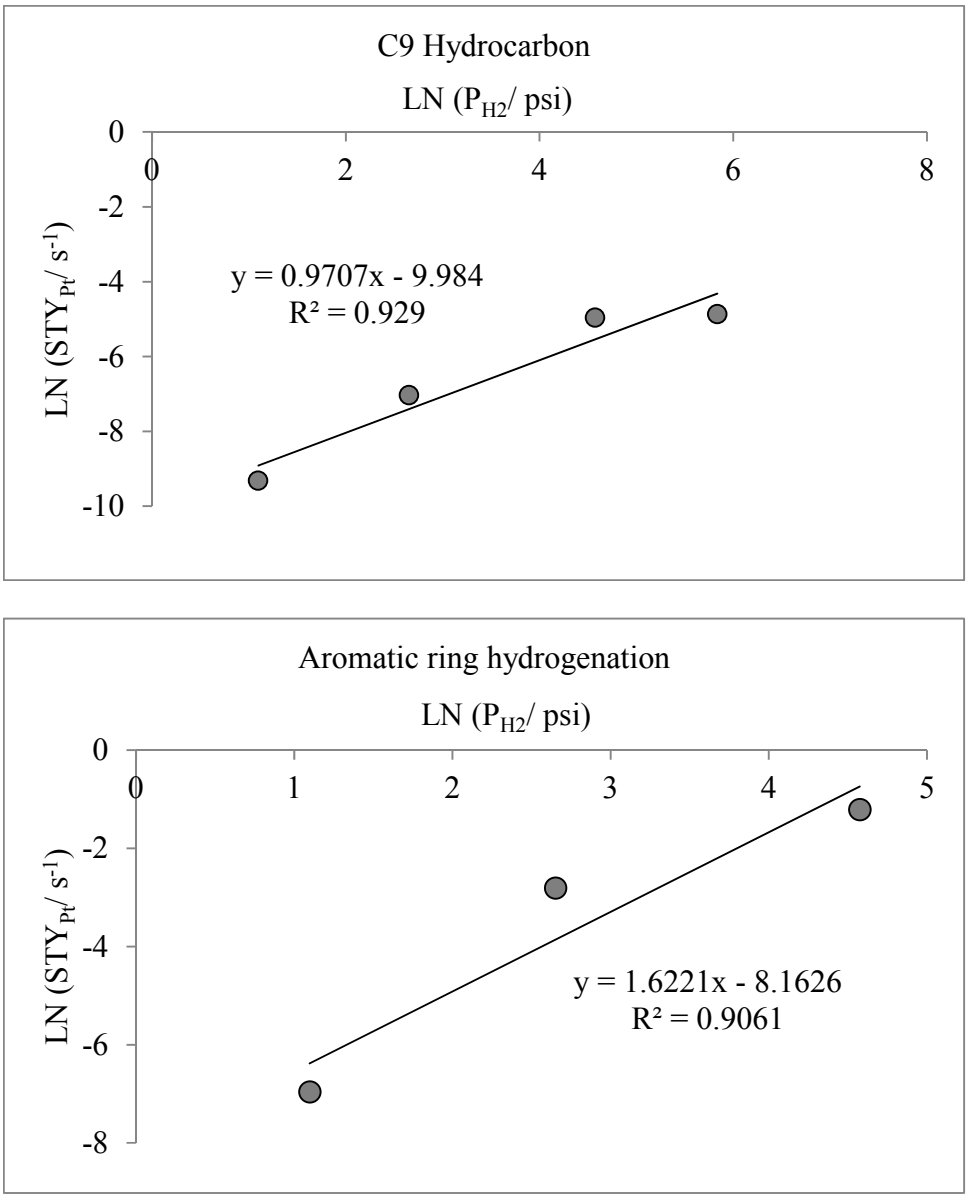

Figure C.4 Hydrogen order plots for C9 hydrocarbon and aromatic ring hydrogenation in a range of 0.02 to 2.4 MPa hydrogen partial pressure over 5%Pt-2.5%Mo and 300°C

WHSV plots for minor products (5%Pt-2.5%Mo)

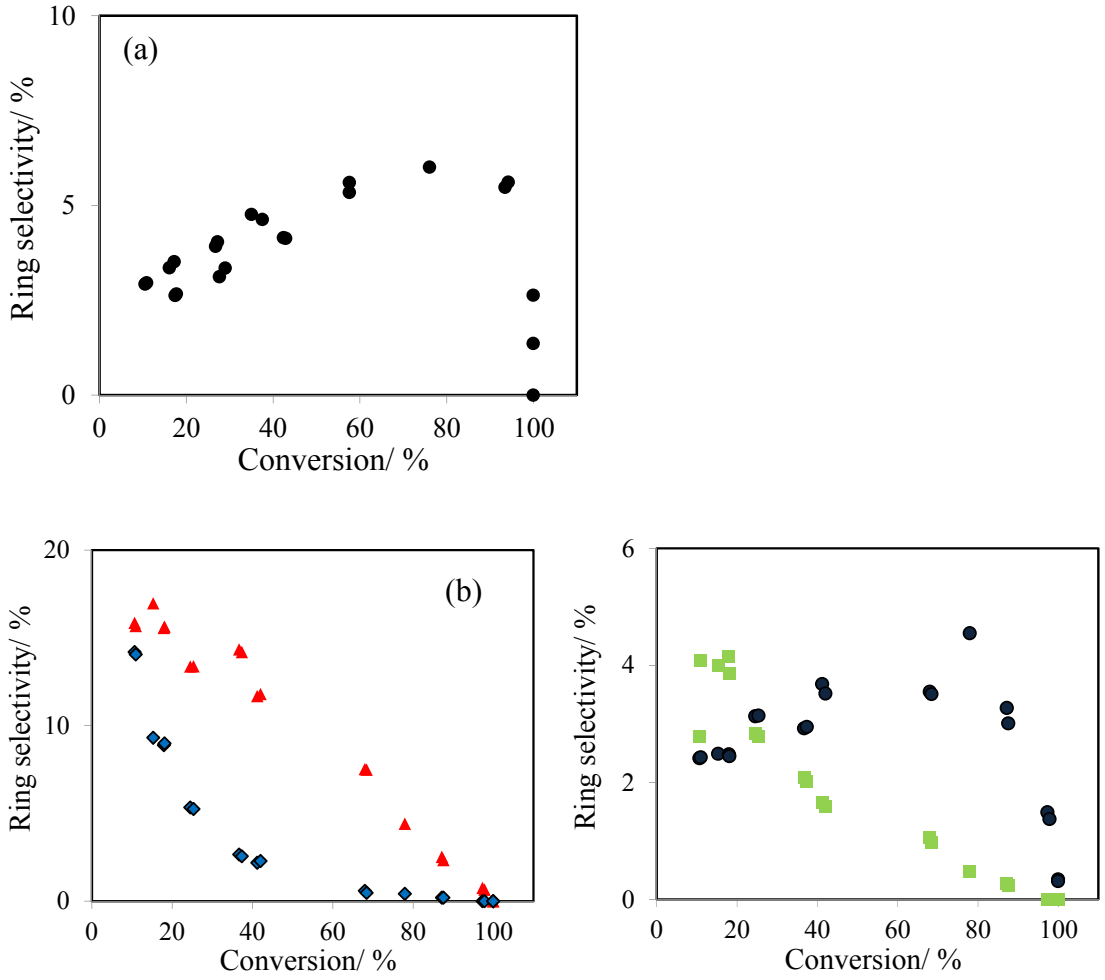

Figure C.5 Minor products selectivity as a function of conversion for (a) 0.1 MPa and (b) 0.7 MPa hydrogen partial pressure over 5%Pt-2.5%Mo catalyst at 300°C. Legend: 2-methoxy-4-propylcyclohexanol (red triangles), 4-propyl-1,2-benzenediol (blue diamonds), methylpropylphenol (green squares) and propylanisole (black circles)

Light gas products (5%Pt and 20%Mo)

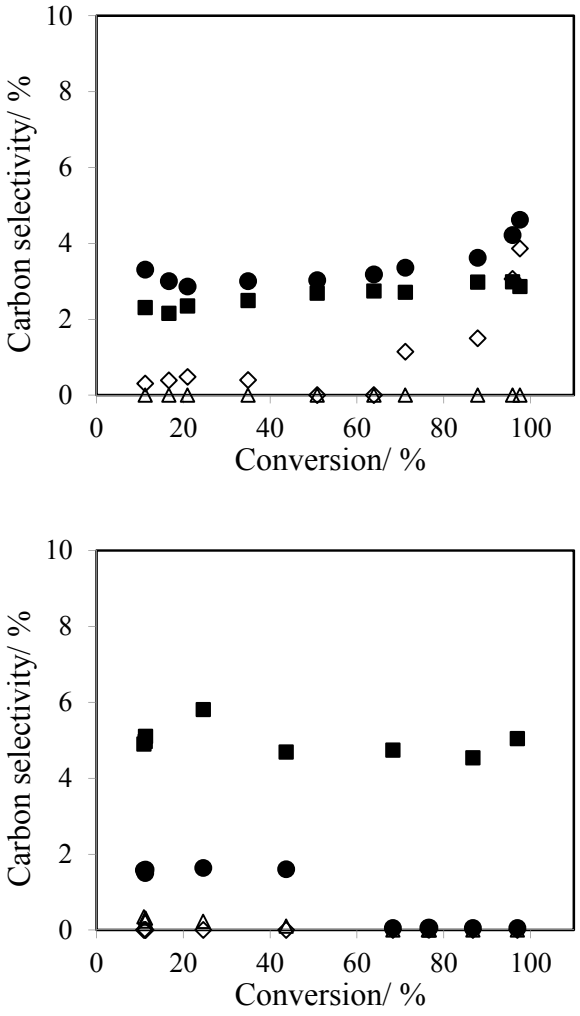

Figure C.6 Carbon selectivity for light C_1 products for (a) 5%Pt and (b) 20%Mo catalysts. Legend: methane (circles), methanol (squares), carbon monoxide (diamonds) and carbon dioxide (triangles)

VITA

VITA

Dhairya Dilip Mehta
Graduate School, Purdue University

Education

Bachelor of Chemical Engineering, 2009, Institute of Chemical Technology, Mumbai, India
Master of Science, Chemical Engineering, 2013, Purdue University, Indiana, USA
Applied Management Principles, Krannert School of Management, 2013, Purdue University, Indiana, USA
Doctor of Philosophy, Chemical Engineering, 2014, Purdue University, Indiana, USA

Experience

Graduate research (Purdue University

- Studied kinetics of vapor-phase hydrodeoxygenation of dihydroeugenol (lignin-based model compounds) and furfural (cellulose and hemicellulose based model compound) over Pt, Pt-Mo and Mo catalytic systems supported on multi-walled carbon nanotubes. Demonstrated the role of hydrogen in influencing the kinetics of hydrodeoxygenation pathway and hence in the final product distribution.
- Worked as a part of three member team on a novel continuous feed millisecond timescale fast hydropyrolysis reactor to study the effect of residence time and temperature on product distribution. Explained the disconnect between the microgram scale batch reactor and the lab-scale continuous feed reactor results.
- Determined the kinetics of water-gas shift reaction under aqueous phase reforming conditions. Correlated the kinetics obtained in liquid phase WGS to gas phase WGS over Pt and Pt-Mo catalysts.
- Designed and built fixed bed and stirred tank reactor systems capable of handling high pressure hydrogen for conducting kinetics studies described over heterogeneous catalysts.
- Prepared a series of Pt and Pt-based bimetallic catalysts on various supports by incipient wetness impregnation and characterized selected catalysts by Chemisorption, Temperature programmed reduction/ desorption and Transmission electron microscopy.

Undergraduate Research (Institute of Chemical Technology)

- Determined the feasibility of sulfuric acid catalyzed esterification of free fatty acids from waste acid oils in a batch reactor system. Five different waste acid oils were sourced from oil manufacturers from across India such as soya, rice bran and fish oil.
- Kinetics of this reaction was determined in a batch reactor system and compared to that of fatty acid distillate.

Intern (National Organic Chemical Industries Ltd.)

- Developed a vapor-liquid equilibrium diagram for cyclohexylamine-water system using methods like NRTL, UNIQUAC and used it for debottlenecking of the installed distillation column

Skills

- Experimental: High hydrogen pressure compatible reactor design and construction, catalyst prepation, Chemisorption, Temperature programmed reduction, kinetic measurements by gas chromatography - mass spectrometer, liquid chromatography, fourier transform infrared spectroscopy.
- Software: Chemstation, Gaussian, Matlab, Origin, CasaXPS, Endnote, MS Office

Awards and Honors

- Won the best paper presentation (honorary mention) at the Annual Graduate Research symposium, Purdue University (2013)
- Selected to present graduate work at the BASF research forum held at Tarrytown, NY (2013)
- Awarded 1st prize in the Industry Defined Problem competition (Azeotropy) held at IIT Bombay, sponsored by Hindustan Petroleum Corp. Ltd., India (2008)
- Secured 3rd rank in a class of 75, Sophomore year, ICT, Mumbai (2007)
- Awarded Eastman and PGSG travel grants for AIChE and ACS conferences

Presentations

- Mehta D. D., Akatay M. C., Sollberger F. G., Stach E. A., Dumesic J. A., Miller J. T., Delgass W. N., Ribeiro F. H., Liquid phase water-gas shift reaction kinetics over supported Pt and Pt-Mo catalysts

    - Oral presentation, Michigan Catalysis Society Spring Symposium, Midland, MI (May 2012)
    - Oral presentation, AIChE Annual Meeting, Minneapolis, MN (October 2011)
    - Poster presentation, Spring symposium of Catalysis Club of Chicago, Naperville, IL (May 2011)
- Mehta D. D., Smeltz A.D., Delgass W. N., Agrawal R. and Ribeiro F. H., Fast hydropyrolysis of cellulose in a novel millisecond residence time continuous feed reactor
    - Oral presentation, 246th ACS National Meeting, Indianapolis, IN (September 2013)
    - Oral presentation, AIChE National Meeting, San Francisco, CA (November 2013)

Activities and Leadership experience

- Safety officer of Ribeiro Group (March 2012 - May 2013)
    - Evaluated all experimental systems for potential safety hazards on a biannual timescale
    - Audited SOP and emergency procedures for new as well as recently altered rigs
- Social committee chair, Graduate student organization, Chemical Engineering, Purdue University (August 2011 – June 2012)
    - Led a team of 4 members to plan and conduct 12 social and sport events for students and faculty over the year
- Student coordinator of senior year chemical engineering class (2008-2009), acting as a liaison between university and class

Volunteering experience

- Taught Mathematics and Science to adults working towards General education development (GED) tests at Lafayette adult resource academy (LARA) from May-October 2010
- Member of the Graduate student organization's Outreach committee, participated in various local events such as Winterization, De-trash the Wabash